

Structure formation of charged colloidal particles in confined geometry

vorgelegt von

Diplom-Physiker
Stefan Grandner
Freiberg

Von der Fakultät II - Mathematik und Naturwissenschaften
der Technischen Universität Berlin
zur Erlangung des akademischen Grades
Doktor der Naturwissenschaften
Dr. rer. nat.

genehmigte Dissertation

Promotionsausschuss:

Vorsitzende: Prof. Dr. Birgit Kanngießer
1. Gutachterin: Prof. Dr. Sabine H. L. Klapp
2. Gutachter: Prof. Dr. Hartmut Löwen

Tag der wissenschaftlichen Aussprache: 16.12.2011

Berlin 2012
D 83

Eidesstattliche Versicherung

Hiermit versichere ich, dass ich die von mir vorgelegte Dissertation selbstständig angefertigt und die verwendeten Quellen und Hilfsmittel vollständig angegeben habe. Die Kooperation mit anderen Wissenschaftlern habe ich in der Dissertation kenntlich gemacht.

Stefan Grandner

Erklärung

Teile dieser Dissertation wurden in den folgenden 6 Publikationen veröffentlicht:

- S. H. L. Klapp, S. Grandner, Y. Zeng, and R. von Klitzing, J. Phys.: Condens. Matter, **20**, 494232 (2008).
- S. Grandner and S. H. L. Klapp, J. Chem. Phys., **129**, 244703 (2008).
- S. Grandner, Y. Zeng, R. von Klitzing, and S. H. L. Klapp, J. Chem. Phys., **131**, 154702 (2009).
- S. H. L. Klapp, S. Grandner, Y. Zeng, and R. von Klitzing, Soft Matter, **6**, 2330 (2010).
- S. Grandner and S. H. L. Klapp, Europhys. Lett., **90**, 68004 (2010).
- Y. Zeng, S. Grandner, C. L. P. Oliveira, A. F. Thünemann, O. Paris, J. S. Pedersen, S. H. L. Klapp, and R. von Klitzing, Soft Matter, DOI: 10.1039/C1SM05971H (2011).

Abstract

The structure formation in films of charged, colloidal suspensions confined by uncharged and charged slit pores is investigated in the present thesis. The colloids in such systems are characterized by a surface charge corresponding to their size. The counterions, which dissolve from their surface into the solvent, yield an effective screening of the electrostatic repulsion between the particles. The aim of this work is to understand the impact of the system parameters on characteristic lengths, correlations, freezing and melting phenomena. Such parameters are salt concentration, density, particle size, and surface charges of the confining walls. Colloidal suspensions and their structural properties receive great attention in nature sciences and technology as, e. g., the preparation of membranes and photonic crystals.

We consider the system on a theoretical level by employing Monte-Carlo simulations where the particle-particle interactions are modeled via the Derjaguin-Landau-Verwey-Overbeek theory. A special focus in this work is the influence of surface charges of the confinement, providing additional counterions, on the structure formation. Our theoretical predictions for small particle densities are verified by colloidal-probe atomic-force microscope experiments. A prominent effect of confined colloidal and molecular particles is the particle layering parallel to the surfaces yielding the so-called structural forces. This effect exhibits a significant dependence on the system parameters. It involves the decrease of the amplitudes of the oscillating forces by increasing the salt concentration and a force enhancement by increasing the wall charge in a parameter range relevant for the experiment. Furthermore, we show that freezing and melting phenomena are influenced by confinement. In this context, we discuss the onset of crystallization for increasing density and the alternation of (staggered) hexagonal- and square-like structures for narrowing the confinement. These phenomena, affected crucially by wall charges, show a surface-charge-induced reentrant freezing. Finally, the investigations are extended to charged, binary mixtures where we find a so-called structural crossover in homogeneous systems and discuss the impact of the confinement on the composition of the mixture.

Our results contribute to the fundamental understanding of the structure formation in colloidal suspensions as well as in other systems like dusty plasmas and molecular systems. They are a base for further theoretical and experimental studies providing the knowledge for future applications and for understanding nature.

Zusammenfassung

In dieser Arbeit wird die Strukturbildung in Filmen geladener, kolloidaler Suspensionen untersucht, welche durch ungeladene bzw. geladene Schlitzporen räumlich begrenzt sind. Die Kolloide in solchen Systemen sind durch eine Oberflächenladung proportional zu ihrer Größe charakterisiert. Die Gegenionen, welche von den Teilchenoberflächen in das Lösungsmittel dissoziieren, ergeben eine effektive Abschirmung der elektrostatischen Repulsion zwischen den Teilchen. Das Ziel dieser Arbeit ist den Einfluss bestimmter Systemparameter auf charakteristische Längen, Korrelationen und Flüssig-Fest-Übergänge zu verstehen. Solche Parameter sind Salzkonzentration, Dichte, Teilchengröße und Oberflächenladung der begrenzenden Wände. Kolloidale Suspensionen und ihre strukturellen Eigenschaften erhalten große Aufmerksamkeit in den Naturwissenschaften und der Technologie wie z. B. bei der Herstellung von Membranen und photonischen Kristallen.

Mit Hilfe von Monte-Carlo-Simulationen betrachten wir das System auf einer theoretischen Ebene, wobei die Teilchen-Teilchen-Wechselwirkung auf der Grundlage der Derjaguin-Landau-Verwey-Overbeek-Theorie beschrieben wird. Ein spezieller Fokus in dieser Arbeit ist der Einfluss von Oberflächenladungen der begrenzenden Wände, welche zusätzliche Gegenionen abgeben, auf die Strukturbildung. Unsere theoretischen Vorhersagen werden dabei durch experimentelle Resultate unter Verwendung eines Rasterkraftmikroskops gestützt. Ein bekannter Effekt in kolloidalen und molekularen Systemen ist die Schichtenbildung der Teilchen parallel zu den Oberflächen, welche sogenannte Strukturkräfte erzeugt. Dieser Effekt zeigt eine signifikante Abhängigkeit von Systemparametern. Dies beinhaltet eine Amplitudenverringerung der oszillierenden Kräfte durch eine Erhöhung der Salzkonzentration als auch eine Erhöhung der Kraft bei steigender Wandladung innerhalb eines für das Experiment relevanten Bereiches. Außerdem zeigen wir, dass Flüssig-Fest-Phasenübergänge durch die begrenzte Geometrie beeinflusst werden. In diesem Kontext diskutieren wir das Einsetzen von Kristallisation bei steigender Dichte und das abwechselnde Auftreten von (seitlich versetzten) hexagonalen und quadratischen Strukturen bei kleiner werdendem Wandabstand. Diese Phänomene, welche durch die Wandladungen stark beeinträchtigt werden, zeigen ein ladungsinduziertes Gefrieren. Außerdem werden diese Untersuchungen auf geladene binäre Mischungen ausgeweitet. Dabei beobachten wir einen sogenannten strukturellen Übergang in homogenen Systemen und diskutieren den Einfluss der Wände auf die Zusammensetzung der Mischung.

Unsere Resultate tragen zum fundamentalen Verständnis der Strukturbildung, sowohl in kolloidalen Suspensionen als auch in anderen Systemen wie komplexen Plasmen und molekularen Systemen, bei. Sie sind eine Grundlage für weitere theoretische und experimentelle Arbeiten, welche das Wissen für zukünftige Anwendungen liefern und zum Verständnis der Natur beitragen.

Contents

| | | |
|----------|--|-----------|
| 1 | Introduction | 1 |
| 2 | Model system for charged suspensions | 8 |
| 2.1 | Charging and charge screening of surfaces | 8 |
| 2.2 | Derjaguin-Landau-Verwey-Overbeek theory | 10 |
| 2.3 | Soft-core potential | 19 |
| 2.4 | Derjaguin approximation | 20 |
| 2.5 | Uncharged, unstructured walls | 22 |
| 2.6 | Screened, charged walls | 23 |
| 2.7 | Model system for binary mixture of screened, charged particles | 31 |
| 3 | Principles from statistical mechanics and thermodynamics: | |
| | Investigation of structure and phase behavior | 33 |
| 3.1 | Canonical ensemble | 33 |
| 3.2 | Grand canonical ensemble | 35 |
| 3.3 | Isobaric-isothermal ensemble | 36 |
| 3.4 | Structural observables | 37 |
| 3.5 | Asymptotics via Ornstein-Zernike equation | 40 |
| 3.6 | Phase transitions | 43 |
| 3.7 | Ensembles for binary mixtures | 45 |
| 3.8 | Structural observables for binary mixtures | 45 |
| 3.9 | Asymptotic behavior in binary mixtures | 46 |
| 4 | Simulation Methods | 48 |
| 4.1 | Reduced units | 48 |
| 4.2 | Periodic boundaries and minimum image convention | 48 |
| 4.3 | Truncated and shifted potential | 50 |
| 4.4 | Monte-Carlo method | 52 |
| 4.5 | Monte-Carlo method for binary mixtures | 56 |
| 4.6 | Sampling the chemical potential | 57 |
| 5 | Structure formation at low densities | 59 |
| 5.1 | Layering effect | 59 |
| 5.2 | Influence of the salt concentration | 61 |
| 5.3 | Influence of the particle size | 66 |
| 5.4 | Impact of surface charges on structural forces | 71 |

| | | |
|----------|---|------------|
| 6 | Crystal-like structuring at moderate and large densities | 81 |
| 6.1 | Freezing transitions in bulk | 81 |
| 6.2 | Capillary freezing | 82 |
| 6.3 | Density-induced freezing and solid-solid transition | 84 |
| 6.4 | Surface-charge-induced freezing | 95 |
| 7 | Binary mixtures | 104 |
| 7.1 | Structural crossover in bulk systems | 105 |
| 7.2 | Impact of confinement on layering and composition of a binary mixture | 114 |
| 8 | Conclusion and outlook | 122 |
| A | Calculation of local bond angle order parameters | 127 |
| B | Fourier transforms of Coulomb and Yukawa potential | 128 |

1 Introduction

The structure formation of colloidal particle suspensions receives continuous attention for decades. There is a diversity of naturally existing and artificially made colloids. These particles are of great interest for technical (e. g., photonic crystals [17], colloidal dispersions for purification of water, sedimentation processes [82]), chemical (e. g., paints, cosmetics), and medical applications (e. g., drug targeting [71]), but also for biological systems (e. g., blood cells, fd viruses [77]). The size of colloids is in the range of nanometers to microns. In contrast to atoms or small molecules, quantum effects are less important or can even be neglected. Thus, the particle interactions are well described by principles of classical statistical mechanics [39, 52].

Depending on certain system parameters including external fields, colloidal suspensions exhibit a variety of possible structures involving different states of aggregation referred to as gas, fluid (or liquid), gel, glass, or solid. Such system parameters are temperature, density, pressure, solvent properties (salt concentration, permittivity), electrical or magnetic fields, but also material properties of the colloids as, e. g., particle size, shape, charge, dipole moments, and surface properties. Understanding these aspects gives deeper insight into colloidal science and applications based on it. From a theoretical point of view, analytical and numerical methods from statistical physics are the appropriate tool for predicting macroscopic properties of these materials found in real life or in experiments. However, an explicit description of these many-particle systems is difficult due to the large number of particles which is in the order of Avogadro's constant ($\propto 10^{23}$). One method to deal with this problem are coarse-graining approaches where certain degrees of freedom are integrated out. In other words, these particles are treated implicitly in the free energy of the system. This is reasonable if the system is characterized by different length- and time scales, i. e., only the big (colloidal) particles are treated explicitly whereas very small particles (e. g., counterions) or solvent molecules with short length- and timescales are treated implicitly. Another method is the mean-field approach where not only the degrees of freedom are integrated out but also correlations of these particles are neglected. In other words, all particles, interacting with a certain particle, are replaced by a mean field.

Confining surfaces in colloidal suspensions are an important type of external fields which are omnipresent. They occur in biological systems (e. g., venes or cell walls) as well as in technical systems (e. g., the pore walls in porous materials [76] and microfluidic devices [54]). Between narrow surfaces, the liquids or suspensions form thin films with complex behavior [67]. Confinement can also be realized in experimental setups as, e. g., the colloidal-

probe atomic-force microscope (CP-AFM) [32] or the surface force apparatus (SFA) [66].

A well-known effect induced by confinement is the layering of the particles. It is a consequence of the symmetry breaking by the surface. Thus, a homogeneous (bulk) system changes into an inhomogeneous system [124]. This is indicated by an oscillating local density perpendicular to the surfaces. This was found, e. g., for ferrofluids [122, 8]. A generic feature arising from the layering in a slit-pore, consisting of two adjacent, infinitely extended, plane-parallel walls, are the so-called structural (or solvation) forces. For small or moderate densities these forces exhibit an oscillatory, exponential decaying behavior. They originate from the competition between the formation of particle layers and the arrangement of the particle between the confining surfaces found experimentally for colloidal silica particles and polystyrene in [92]. A theoretical study discussed this effect for Lennard-Jones (LJ) particles using Ornstein-Zernike (OZ) theory [89]. Via Monte-Carlo (MC) simulations and density-functional theory (DFT), charged colloidal spheres and polyelectrolytes were investigated in [69]. Besides experimental findings in colloidal systems [97, 116], these forces were also found for small molecules as, e. g., in water [66] and octamethylcyclotetrasiloxane (OMCTS) [63] using SFA with mica surfaces. Furthermore, it was found for molten salts [62], micellar solutions [103, 112], and polyelectrolytes [112]. Using such colloidal suspension as a solvent for much larger particles, the suspension acts as a “depletion agent”. There, the solvent particles form layers between the bigger ones which induces oscillations in the depletion interactions [11, 97].

A further effect of the layering is that it can induce freezing transitions. This was found experimentally, e. g., for silica and polystyrene spheres [92]. Theoretically, it occurred in hard sphere (HS) systems investigated by MC [107, 37] and free volume theory [107, 108], but also in soft sphere (SS) systems using molecular dynamics (MD) simulations [113] and LJ systems using MC [7]. The corresponding bulk system freezes at larger densities [2]. In a slab-geometry, this shift is referred to as capillary freezing [29]. Freezing in confined, colloidal systems yields a variety of crystal-like structures known from theory and experiment. The most prominent structures are hexagonal and squared crystals [107], but there are more complex ones as, e. g., prism, rhombic and buckled structures [107, 108, 37, 102]. Controlling these freezing mechanisms are a tool to obtain special material properties. In this context, novel self-assembled structures are receiving great attention [9, 118, 17]. At interfaces, membranes can be prepared from two-dimensionally self-assembled colloids [128]. Besides the impact on the translational order, the orientational order can be affected as well. This is known for the isotropic-nematic transition of rods [21], the chain formation in dipolar

systems [70], and the structure formation of rod-like, dipolar particles under shear [53]. Small angle scattering with neutrons (SANS) [74] or X-rays (SAXS) [130] are useful to investigate bulk systems, whereas total internal reflection microscopy (TIRM) is used to examine the interaction of a flat surface with particles [121] and their structure formation [99].

With this background, this thesis explores charged, colloidal suspensions in confinement. Most natural and artificial materials possess surface charges if they are suspended in a polar solvent as, e. g., water. The charges result from a dissociation of oppositely charged counterions to the solvent. These ions screen the potential of the surface yielding a Yukawa-like potential. This is related to the widespread field of dusty plasmas [38, 87]. To this end, charged silica nanoparticles are considered theoretically (computer simulations) and experimentally (CP-AFM), since they are a model system tunable in size, charge, and polydispersity. These parameters change the particle interaction in a complex way since the surface charge of the particles depends on their diameter. Furthermore, the charge can be controlled by addition of salt to the solvent. Thus, a more complex behavior is expected as compared to HS or LJ systems. This issue was addressed in our publications [73, 130]. The system, consisting of macroions and microions, is modeled on an effective level using a coarse-graining approach. This yields the well-known Derjaguin-Landau-Verwey-Overbeek (DLVO) potential [119]. In more detail, the microions are integrated out since their dynamics are on a much shorter length- and timescale as compared to the macroions. In addition to this implicit treatment, a mean field approach is used by neglecting the microion correlations. Thus, the number of explicitly treated particles decreases significantly since there are much more microions in the system due to the polyvalence of the macroions. These steps yield an effective screening parameter (inverse Debye length) which describes the screening of the electrostatic macroion potential by the microions [52].

In this thesis, we examine this coarse-grained model for a charged suspension by employing MC computer simulations in different ensembles and compare the results with CP-AFM experiments. The experiments were done, in cooperation with the group of Regine von Klitzing at the TU Berlin, by Yan Zeng [75, 72, 45, 73]. Within this method, first introduced by Ducker et al. [32], a colloidal silica sphere with radius $R = 3.35\mu m$ is glued to the apex of a tipless AFM cantilever. It is mounted in a molecular force probe setup such that a force acting on the colloidal sphere is detected as a deflection. A few drops of the colloidal silica suspension is given on a silicon wafer possessing a native silica (SiO_2) top and the cantilever is immersed into the solution. A sketch of the setup is given in fig. 1a. Thus, the force on the big colloidal sphere exerted by the suspension, which is confined be-

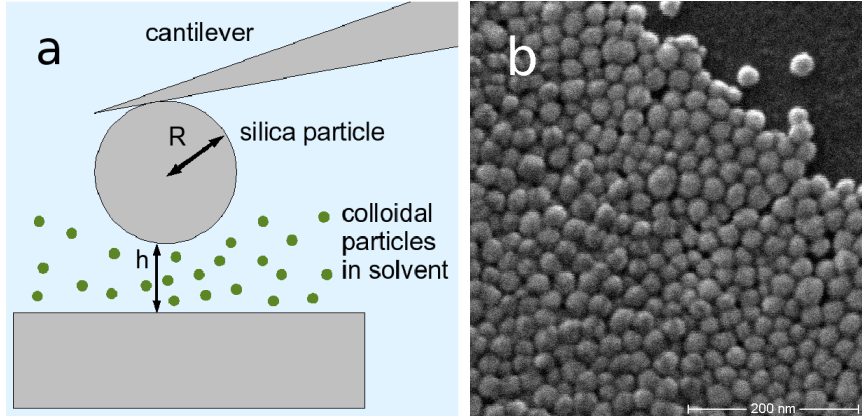


Figure 1: a) Sketch of the CP-AFM with a confined suspension. b) TEM image of the silica particles TMA-34.

tween the sphere and the wafer, can be measured as function of the surface separation. Since the colloidal sphere is much bigger than the colloidal silica particles in the solution, it can be approximated as flat due to Derjaguin's approximation (DA). In order to ensure reproducibility and to obtain good statistics, 30-40 force-distance curves were measured at different lateral locations on the same substrate as well as on different substrates. Depending on the investigations, a fresh cleaved mica sheet is deposited on the top of the silicon wafer [45]. Different colloidal silica suspensions are used for the investigations containing silica beads of the types TMA-34 (see fig. 1b), HS-40, and SM-30 which were purchased from Aldrich (Taufkirchen, Germany). The corresponding diameters of $25 \pm 2\text{nm}$, $16 \pm 2\text{nm}$, and $9 \pm 2\text{nm}$, respectively, were determined via transmission electron microscopy (TEM), SANS, and scanning force microscopy.

We demonstrate that effects as layering, solvation forces, and freezing transitions are highly sensitive on varying the system properties. This is discussed in our publications [72, 43, 73, 130]. In more detail, the amplitudes and phases of the solvation forces depend on the particle charge (i. e., on the particle size) [73] as well as on the amount of added salt [72]. We obtained fluid-solid transitions and solid-solid transitions. The charged particles begin to crystallize at densities beneath the bulk freezing transition (capillary freezing). This behavior was examined theoretically by us in [43]. It is noteworthy that the Yukawa-like potential of the particles induces the bulk freezing transition at smaller densities as compared to the HS or SS system [56, 57]. At larger densities, phase transitions between different solid structures have been found exhibiting an alternation between (staggered)

hexagonal and squared (non-perfect) structures. This was also obtained for confined HS in [37] but the phase transitions are shifted towards different wall separations and densities.

A main feature of this thesis is the investigation of charged confining surfaces. Whereas several theoretical studies considered simple uncharged hard or soft walls [29, 7, 37], the impact of additional counterions from the charged walls was found to be crucial. This issue was examined in our publications [45, 44]. Such systems occur in biological and technical contexts such as, e. g., proteins at charged lipid membranes [96, 129], microfluidic devices consisting of charged channels [54], or other experimental setups [12]. First attempts in this direction concerning the influence of wall counterions on the particle-particle interaction were done for Yukawa interactions in [26]. The effective force between a pair of charged macroions confined by charged surfaces was considered in [4, 64]. However, due to the inhomogeneous ion distribution within the slit-pore assumed here, the impact on the layering is marginal found in [26]. Here, we go one step further and take the influence of the wall counterions on the particle-wall interaction into account which was published by us in [45]. A consequence of the screened wall potential is the non-monotonic behavior as function of the surface potential. This effect results from the competition between the electrostatic repulsion and the screening. Above a certain surface potential, the screening dominates which has a crucial impact on the layering and the related structural forces. In more detail, their oscillatory behavior in the asymptotic range exhibits a non-monotonic behavior in the amplitude and the phase, whereas the wave- and the decay length are unaffected. The latter fact conforms with DFT predictions [34, 48] that the wave- and decay lengths of the structural forces in a confined system is determined by the bulk correlations at same chemical potential. Above a critical surface potential, the amplitude of the structural force enhances. Indeed, this enhancement was found in CP-AFM experiments in cooperation with the group of R. v. Klitzing (TU Berlin) [74]. One explanation is that, due to the stronger screening of the wall charges at larger surface potentials, more particles can move into the slit-pore from the connected bulk reservoir. In a former study by Löwen et al. [84] such a behavior was found for charged colloidal particles trapped in a charged wedge.

Furthermore, we demonstrated in [44], for the first time, that surface charges can affect freezing transitions. Considering a slit-pore of like-charged walls, it is shown that the density of capillary freezing is shifted in a non-monotonic way as function of the surface potential. The inner, lateral structure of the frozen phase is also affected. Only by replacing the surface material, it is possible to create fluid, hexagonal, or squared structures without changing other system parameters. Changing the surface potential contin-

uously, we found indications for first order phase transitions between these structures.

So far, we focused on monodisperse suspensions. However, a wide range of systems existing in nature and in application contexts is actually composed of several types of particles. Here, we focus on binary systems where the two species are characterized by different core radii, charges, dipole moments, or other properties. The thesis takes a closer look on them in bulk and confinement. In particular, we investigate the effect of structural crossover for strongly asymmetric, charged, binary mixtures which is known for HS systems [47, 48]. It describes the observation that in a mixture the asymptotic correlations are characterized by a certain wave- and decay length which are in the order of the size of one particle species of the system. Confining a mixture by a surface or in a slab-geometry, is supposed to affect the arrangement of particles in it [104]. Thus, we consider the layering of the different charged particle species depending on the densities and the composition of them. Similar investigations were employed for mixtures containing polar and non-polar particles using MC simulations [19].

The thesis is organized as follows. In chapter 2, the model system is introduced. The process of surface charging is explained and described by physical models. The DLVO potential is derived from principles of statistical mechanics using a DFT approach following [52]. This potential is supplemented by a (short-ranged) soft-core potential in order to mimic experimental conditions. The modeling of the confinement is discussed. There, we focus on the modifications of the particle-wall screening for charged surfaces introduced in our study [45]. In chapter 3, principles of statistical mechanics and thermodynamics are discussed and recapitulated. This involves the thermodynamic ensembles (canonical, grand canonical, and isobaric-isothermal) used in our simulations. Structural observables are explained which are used to quantify static properties of the simulated suspension for certain system parameters. Additional methods and analytical expressions are discussed. This involves an analytical expression for the asymptotic behavior of correlation functions derived from OZ theory. Furthermore, a brief discussion of indications for phase transitions is presented. Chapter 4 describes simulation details including a recapitulation of the MC method. Furthermore, the determination of the chemical potential, which is essential for the grand canonical ensemble, is described. In chapter 5 and 6, the results of our simulations for monodisperse, charged suspensions are presented and discussed. Whereas chapter 5 focuses on layering and structural forces at low densities, chapter 6 discusses the impact of confinement on freezing transitions. A main issue in these chapters is the influence of surface charges on the structure formation. In the last results chapter 7, strongly asymmetric, binary mixtures of charged

colloids are examined. There, the structural crossover in bulk systems is investigated for varying mixture compositions. Furthermore, the impact of confinement on the structure formation (layering) is considered. The thesis ends with a conclusion of the main aspects and gives an outlook for future work.

2 Model system for charged suspensions

2.1 Charging and charge screening of surfaces

Before describing the interaction between the spherical particles of the suspensions considered, we take a brief look on the mechanisms leading to surface charges of materials in contact with polar solvents.

Surfaces in contact with a dipolar liquid are in most cases charged [20]. Water, e. g., greatly supports the solvation of ions due to its high dielectric constant. The process of charging can be divided into several mechanisms. Two of them are adsorption and dissociation. The former might be due to protonation, i. e., a negatively charged group is exposed (e. g. an amino group of a protein) leaving behind a proton H^+ on the surface which yields a positive surface charge. The latter, which is typical for oxides, is realized by dissociation of a proton from the surface yielding a negative surface charge. In the following we consider the case of dissociation which is of interest of this study.

A theoretical description of this system was formulated by Gouy and Chapman for a planar surface [42, 22]. The surface charges induce an electric field which influence the distribution of the dissociated ions where two effects compete. On one hand the ions are attracted by the oppositely charged surface. On the other hand the thermal motion yields a diffusion of the ions away from the surface. In equilibrium a diffusive layer forms above the surface. The charged surface together with the ion layer is called *electric double layer*. In general, further co- and counterions, e. g. an additional salt, can be solved in the solvent. The Coulomb potential of the charged surface is screened by the ions. Hence, it is useful to derive an effective potential taking the screening into account. Theoretically, this can be formulated via Poisson-Boltzmann theory. The effective potential $\phi(\mathbf{r})$ is given by the Poisson equation

$$\nabla^2 \phi(\mathbf{r}) = -\frac{\rho(\mathbf{r})}{\varepsilon \varepsilon_0}. \quad (1)$$

The co- and counterions of species i are assumed to be Boltzmann distributed normal to the charged surface given by

$$\rho_i(\mathbf{r}) = \nu_i e_0 c^0 \exp(-W_i(\mathbf{r})/k_B T) \quad (2)$$

with $\rho(\mathbf{r}) = \sum_i \rho_i(\mathbf{r})$, the bulk ion concentration c^0 , and the work W_i which is required to shift an ion of species i from infinity towards the surface. The Boltzmann distribution given in eq. (2) is a mean field approach neglecting correlation effects. Thus, the counterions are assumed to be monovalent since it is known that multivalent charges cause significant counterion correlations

changing the effective interaction [106, 3] and can even induce charge inversion [111]. The work is given by $W_+(\mathbf{r}) = \nu_+ e_0 \phi(\mathbf{r})$ and $W_-(\mathbf{r}) = \nu_- e_0 \phi(\mathbf{r})$ with the valencies ν_i of the cations and the anions. In case of monovalent ions assumed here, the valencies are $\nu_+ = 1$ and $\nu_- = -1$. It is assumed that the salt concentration is much higher than the concentration of the dissolved ions. Otherwise, the number of anions and cations (including counterions and background salt) would not be the same [20]. Thus, the electroneutrality condition is fulfilled.

Finally, inserting eq. (2) into eq. (1) yields the Poisson-Boltzmann equation

$$\nabla^2 \phi(\mathbf{r}) = -\frac{e_0 c^0}{\varepsilon \varepsilon_0} \sum_i \nu_i \exp\left(-\frac{\nu_i e_0 \phi(\mathbf{r})}{k_B T}\right). \quad (3)$$

A limitation of PB theory is the neglected discrete structure of the ions and the surface. This becomes important at high ion densities where the mean distance between the ions is getting very small and the detailed molecular structure might become important [20]. Thus, the theory is limited to small concentrations. Furthermore, PB theory is a mean-field approach, i. e., the particles interact with an average field of the other particles but local correlation effects are not taken into account. More precisely, the ion distribution given in eq. (2) is only determined by the effective potential $\phi(\mathbf{r})$ which does not involve concrete ion-ion interactions.

In many cases the Poisson-Boltzmann equation is linearized by assuming low potentials ϕ since an analytical solution is only for simple cases accessible, e. g., in one dimension. To this end, the exponential function is expanded for small ϕ omitting terms of second and higher order, i. e., $\exp(-\nu_i e_0 \phi(\mathbf{r})/k_B T) = 1 - \nu_i e_0 \phi(\mathbf{r})/k_B T$ which yields the linearized PB equation [20]

$$\nabla^2 \phi(\mathbf{r}) = -\frac{e_0 c^0}{\varepsilon \varepsilon_0} \sum_i \nu_i \left(1 - \frac{\nu_i e_0 \phi(\mathbf{r})}{k_B T}\right) \quad (4)$$

$$= \kappa^2 \phi(\mathbf{r}). \quad (5)$$

with the inverse Debye length κ defined by $\kappa^2 = 2e_0^2 c^0 / (\varepsilon \varepsilon_0 k_B T)$. Note, that $\nu_{\pm} = \pm 1$ was used. The first summand in eq. (4) vanishes due to the electroneutrality condition. The linearized PB equation given in eq. (5) can be solved analytically for a flat surface perpendicular to the z -axis at $z = 0$. With the boundary conditions $\phi(z \rightarrow 0) = \psi_S$ and $\phi(z \rightarrow \infty) = 0$ the solution reads

$$\phi(z) = \psi_S \exp(-\kappa z) \quad (6)$$

with the surface potential ψ_S . The same consideration in case of spherical particles was done by Debye and Hückel [24] which is the basis for the effec-

tive interaction of sterically charge-stabilized spherical particles discussed in sec. 2.2.

Knowing the material properties, i. e. the number of charged groups on the surface, one can estimate the surface charge which is related to the surface potential ψ_S . The charge density σ_S of a surface with potential ψ_S in contact with a solvent is given by the Grahame equation. Assuming charge neutrality this relation can be derived analytically for a one-dimensional case using the exact Poisson-Boltzmann equation and reads [20]

$$\sigma_S = \sqrt{8c_0\varepsilon_0\varepsilon k_B T} \sinh \frac{e_0\psi_S}{2k_B T} \quad (7)$$

with the total ion concentration $c_0 = Z\rho + IN_A$ of the bulk suspension where Z is the valency of the particles, I is the ionic strength (salt concentration), and N_A is Avogadro's constant. The surface charge of a spherical particle with diameter σ is given by

$$Ze_0 = 4\pi \left(\frac{\sigma}{2}\right)^2 \sigma_S. \quad (8)$$

2.2 Derjaguin-Landau-Verwey-Overbeek theory

Simulating charged colloidal suspensions within the primitive model [3], i. e. the explicit treatment of all macro-, co-, and counterions interacting with Coulomb interactions, needs much effort since the number and size of the co- and counterions strongly differs from that of the macroions, as well as the different time scales on which the particles move. The small ions and the fluid molecules are much faster than the bigger macroions. In order to get good statistics one must use an appropriate number of macroions and therefore a much bigger number of co- and counterions. Accelerating methods such as cell lists and Verlet lists are not applicable due to the long-ranged Coulomb interactions of the charged particles. Against this background, effective models have been developed which neglect the explicit description of the huge number of co- and counterions but treat them within a mean field approach. First, in a coarse-graining step these degrees of freedom are integrated out. In a second step, the mean-field approximation, correlations of these microions are neglected, i. e., they are replaced by an average field [52]. To this end, it is necessary to consider the distribution of the small ions in the vicinity of a big ion. Assuming that polarization of the particles can be neglected here, all particles interact by spherical forces. The counterions are attracted by the oppositely charged macroion. This is counterbalanced by the entropy-driven tendency of the counterions to distribute homogeneously

in space. To fulfill this balance the ions arrange in a steady distribution where their chemical potentials in the vicinity of the macroion surface are in equilibrium with the chemical potentials of the bulk (far from the surface). The effect for the equally charged coions is similar but they are repelled by the macroion. Thus, the charged surface of the macroion and the counterions form an electric double-layer. Due to the resulting screened electrostatic repulsion, the particles are sterically charge-stabilized. Besides this repulsion, DLVO theory also involves attractive Van-der-Waals interactions [119, 20], which are neglected in this study. These forces, possessing a short interaction range, are important for coagulation and precipitation. However, we assume that the particles considered here do not come in the interaction range of these forces.

Thus, it is of great interest in this study to derive the well-known and widely used DLVO interaction potential [119] without van-der-Waals interaction. This interaction potential is the basis for the investigations presented in this thesis. Following the derivation in [52], we start from the primitive model where the potential energy of the system, containing macroions O and microions M , has the form

$$V(\{\mathbf{R}_i\}, \{\mathbf{r}_j\}) = V_{00}(\{\mathbf{R}_i\}) + V_{0M}(\{\mathbf{R}_i\}, \{\mathbf{r}_j\}) + V_{MM}(\{\mathbf{r}_j\}). \quad (9)$$

It is useful to consider the system in a semi-grand canonical ensemble meaning that the number of macroions N_0 is fixed whereas the number of microions N_M can fluctuate. The corresponding partition function reads

$$Q_{N_0} = \frac{1}{N_0! \Lambda_0^{3N_0}} \int \exp(-\beta V_{00}) \Xi_M(\mu_+, \mu_-, V, T; \{\mathbf{R}_i\}) dR^{3N_0} \quad (10)$$

which describes the canonical ensemble of macroions with a fixed particle number. The quantity Ξ_M , used in eq. (10), is the grand partition function of the microions with chemical potentials μ_ν in the external potential of the macroions. It is given by

$$\Xi_M = \sum_{N_+ = 0}^{\infty} \sum_{N_- = 0}^{\infty} \frac{\xi_+^{N_+} \xi_-^{N_-}}{N_+! N_-!} \int \int \exp[-\beta(V_{0M} + V_{MM})] dr^{3N_+} dr^{3N_-} \quad (11)$$

with the activities ξ_\pm of the microions given by $\xi_\nu = \exp(\beta \mu_\nu) / \Lambda_\nu^3$ where Λ_ν is the thermal wavelength. The partition function eq. (10) can be re-expressed by introducing an effective potential acting on each macroion which is

$$V_{eff}(\{\mathbf{R}_i\}) = V_{00}(\{\mathbf{R}_i\}) + \Omega_M(\mu_+, \mu_-, V, T; \{\mathbf{R}_i\}) \quad (12)$$

and contains the grand partition function of the microions via

$$\Omega_M = -k_B T \ln \Xi_M. \quad (13)$$

Hence, the partition function reads

$$Q_{N_0} = \frac{1}{N_0! \Lambda_0^{3N_0}} \int \exp[-\beta V_{eff}(\{\mathbf{R}_i\})] dR^{3N_0}. \quad (14)$$

The effective potential V_{eff} contains the direct interactions V_{00} between the macroions, which are pairwise additive, and the microion-induced interactions Ω_M , which are not additive and contain a volume term. Hence, the effective interaction is not pairwise additive. First, we introduce the total external potential acting on the microions of species ν which reads

$$\phi_\nu(\mathbf{r}) = \sum_{i=1}^{N_0} v_{0\nu}(|\mathbf{r} - \mathbf{R}_i|) \quad (15)$$

where $v_{0\nu}$ is the macroion-microion interaction potential for species ν . Now, the big challenge is to determine the grand potential Ω_M given by

$$\Omega[\rho_+^{(1)}, \rho_-^{(1)}] = F[\rho_+^{(1)}, \rho_-^{(1)}] - \sum_\nu \int [\mu_\nu - \phi_\nu(\mathbf{r})] \rho_\nu^{(1)}(\mathbf{r}) d\mathbf{r} \quad (16)$$

where the free energy functional can be separated into several contributions

$$F[\rho_+^{(1)}, \rho_-^{(1)}] = \sum_\nu F_\nu^{id}[\rho_\nu^{(1)}] + F^c + F^{corr}. \quad (17)$$

Before evaluating the grand potential eq. (16) using DFT, the containing terms are discussed in more detail and approximations are introduced in the following. We limit ourselves to a mean-field approach where the macroions, behaving like an ideal gas, only experience an average electrostatic potential of the other particles and charges of other surfaces. Therefore, the last term in eq. (16), which contains microion correlations, can be set to $F^{corr} = 0$. The remaining contributions are the free energy of an ideal gas for species ν ,

$$F_\nu^{id} = k_B T \int \rho_\nu^{(1)}(\mathbf{r}) (\ln[\Lambda_\nu^3 \rho_\nu^{(1)}(\mathbf{r})] - 1) d\mathbf{r}, \quad (18)$$

and the free energy stemming from the Coulomb interactions of all microions in the mean-field approximations, that is

$$F^c = \frac{1}{2} e_0 \int \Phi^c(\mathbf{r}) \rho_Z(\mathbf{r}) d\mathbf{r}. \quad (19)$$

The electrostatic potential of the microions Φ^c used in eq. (19) satisfies the Poisson equation

$$\nabla^2 \Phi^c(\mathbf{r}) = -\frac{e_0 \rho_Z(\mathbf{r})}{\varepsilon \varepsilon_0} \quad (20)$$

with the charge density of all microions $\rho_Z(\mathbf{r}) = \sum_{\nu} z_{\nu} \rho_{\nu}^{(1)}(\mathbf{r})$. It can be determined with the help of the Green's function $G(\mathbf{r}, \mathbf{r}')$ which gives the electrostatic potential at \mathbf{r}' due to a point charge at \mathbf{r} . Hence, Φ^c is given as

$$\Phi^c(\mathbf{r}) = \int G(\mathbf{r}, \mathbf{r}') e_0 \rho_Z(\mathbf{r}') d\mathbf{r}'. \quad (21)$$

Without boundaries, the Green's function takes the Coulombic form $G(\mathbf{r}, \mathbf{r}') = G(\mathbf{r}' - \mathbf{r}) = 1/(4\pi\varepsilon\varepsilon_0|\mathbf{r}' - \mathbf{r}|)$. Then, inserting eq. (21), the mean-field approximation of the Coulombic contribution of the free energy given in eq. (19) becomes

$$F^c = \frac{1}{2} e_0^2 \int \int \frac{\rho_Z(\mathbf{r}) \rho_Z(\mathbf{r}')}{4\pi\varepsilon\varepsilon_0 |\mathbf{r} - \mathbf{r}'|} d\mathbf{r} d\mathbf{r}'. \quad (22)$$

Applying the variational principle on eq. (16) yields a system of coupled differential equations which can be solved via MD [83]. However, we are interested in further analytical progress which can be achieved by assuming weak inhomogeneities induced by the macroions. To this end the free energy contributions in eq. (17) will be expanded in the deviation of the local density $\rho_{\nu}^{(1)}(\mathbf{r})$ from its bulk value n_{ν}

$$\Delta\rho_{\nu}^{(1)}(\mathbf{r}) = \rho_{\nu}^{(1)}(\mathbf{r}) - n_{\nu}. \quad (23)$$

The integrand of the ideal part given in eq. (18) then becomes

$$\begin{aligned} \rho_{\nu}^{(1)}(\mathbf{r}) (\ln[\Lambda_{\nu}^3 \rho_{\nu}^{(1)}(\mathbf{r})] - 1) &\approx n_{\nu} (\ln[\Lambda_{\nu}^3 n_{\nu}] - 1) \\ &+ \ln[\Lambda_{\nu}^3 n_{\nu}] \Delta\rho_{\nu}^{(1)}(\mathbf{r}) + \frac{1}{2n_{\nu}} (\Delta\rho_{\nu}^{(1)}(\mathbf{r}))^2. \end{aligned} \quad (24)$$

Inserting equations eq. (17), eq. (19) and eq. (24) into the grand potential eq. (16) yields

$$\begin{aligned} \Omega[\rho_+^{(1)}, \rho_-^{(1)}] = & \sum_{\nu} \left(F_{\nu}^{id}(n_{\nu}) + k_B T \ln[\Lambda_{\nu}^3 n_{\nu}] \int \Delta\rho_{\nu}^{(1)}(\mathbf{r}') d\mathbf{r}' + \frac{k_B T}{2n_{\nu}} \int (\Delta\rho_{\nu}^{(1)}(\mathbf{r}'))^2 d\mathbf{r}' \right) \\ & + \frac{1}{2} e_0 \int \Phi^c(\mathbf{r}') \rho_Z(\mathbf{r}') d\mathbf{r}' - \sum_{\nu} \int [\mu_{\nu} - \phi_{\nu}(\mathbf{r}')] \rho_{\nu}^{(1)}(\mathbf{r}') d\mathbf{r}' \end{aligned} \quad (25)$$

The chemical potentials μ_ν are replaced by their ideal values

$$\mu^{id} = k_B T \ln[\Lambda^3 \rho^{(1)}(\mathbf{r})]. \quad (26)$$

Using the variational principle, the grand potential eq. (25) is minimized with respect to $\Delta\rho_\nu^{(1)}(\mathbf{r})$ in order to find distributions that minimize the free energy. One obtains a system of coupled equations which relates the total electrostatic potentials ϕ_ν with the electrostatic potential of all microions Φ^c and their density distributions ρ_ν . The variation of $\Omega[\rho_+^{(1)}, \rho_-^{(1)}]$ yields

$$\begin{aligned} 0 &= \frac{\delta\Omega[\rho_+^{(1)}, \rho_-^{(1)}]}{\delta\Delta\rho_\nu^{(1)}(\mathbf{r})} \\ &= k_B T \ln[\Lambda_\nu^3 n_\nu] \int \delta(\mathbf{r} - \mathbf{r}') d\mathbf{r}' + \frac{k_B T}{2n_\nu} \int 2\Delta\rho_\nu^{(1)}(\mathbf{r}') \delta(\mathbf{r} - \mathbf{r}') d\mathbf{r}' \\ &\quad + \frac{1}{2} e_0^2 \iint \frac{z_\nu \delta(\mathbf{r} - \mathbf{r}') \rho_Z(\mathbf{r}'') + z_\nu \delta(\mathbf{r} - \mathbf{r}'') \rho_Z(\mathbf{r}')}{4\pi\epsilon\epsilon_0 |\mathbf{r}' - \mathbf{r}''|} d\mathbf{r}' d\mathbf{r}'' \\ &\quad - \int \mu_\nu^{id} \delta(\mathbf{r} - \mathbf{r}') d\mathbf{r}' + \int \phi_\nu(\mathbf{r}') \delta(\mathbf{r} - \mathbf{r}') d\mathbf{r}'. \end{aligned} \quad (27)$$

The resulting system of coupled equations reads

$$-\beta\phi_\nu(\mathbf{r}) = \frac{\Delta\rho_\nu^{(1)}(\mathbf{r})}{n_\nu} + \beta z_\nu e_0 \Phi^c(\mathbf{r}) \quad (28)$$

which are coupled through the electrostatic potential Φ^c . The macroions, which have a diameter of $2R$, are considered as point-like particles for the next steps. Then, the Coulombic contribution to the external potential of the macroions $\phi_\nu(\mathbf{r})$ can be set for each \mathbf{r} to

$$\begin{aligned} \phi_\nu(\mathbf{r}) &= z_\nu e_0 \Phi^{ext}(\mathbf{r}) \\ &= -z_\nu e_0 \sum_i \frac{Ze_0^2}{4\pi\epsilon\epsilon_0} \frac{1}{|\mathbf{r} - \mathbf{R}_i|} \end{aligned} \quad (29)$$

where Φ^{ext} is the external electrostatic potential of the point macroions. The finite diameter of the particles will be reintroduced later by renormalizing the particle charge. The total electrostatic potential containing the contribution of the microions Φ^c and of the macroions Φ^{ext} becomes

$$\Phi(\mathbf{r}) = \Phi^c(\mathbf{r}) + \Phi^{ext}(\mathbf{r}) = e_0 \int \frac{\rho_Z(\mathbf{r}') + Z\rho_{ext}(\mathbf{r}')}{4\pi\epsilon\epsilon_0 |\mathbf{r} - \mathbf{r}'|} d\mathbf{r}' \quad (30)$$

with the microscopic density of the macroions $\rho_{ext}(\mathbf{r}) = \sum_i \delta(\mathbf{r} - \mathbf{R}_i)$. Hence, by rearranging eq. (28), inserting eq. (29) and using eq. (30) one obtains the

deviation of the microion density

$$\Delta\rho_\nu^{(1)}(\mathbf{r}) = -n_\nu\beta z_\nu e_0^2 \int \frac{\rho_Z(\mathbf{r}') + Z\rho_{ext}(\mathbf{r}')}{4\pi\varepsilon\varepsilon_0|\mathbf{r}-\mathbf{r}'|} d\mathbf{r}'. \quad (31)$$

In order to simplify the problem a salt-free case is considered in the following, i. e., the microions only consist of one species which are counterions. Then, eq. (31) becomes a single integral equation and the microion charge density $\rho_Z(\mathbf{r}) = z\rho^{(1)}(\mathbf{r})$. The integral equation can be solved analytically by Fourier transformation $\mathcal{F}[\dots]$. We first apply the transformation on both sides of eq. (31) yielding

$$\mathcal{F}[\Delta\rho^{(1)}(\mathbf{r})] = -\frac{nze_0^2}{k_B T} \int \frac{z\rho^{(1)}(\mathbf{r}') + Z \sum_i \delta(\mathbf{r}' - \mathbf{R}_i)}{4\pi\varepsilon\varepsilon_0} \mathcal{F}\left[\frac{1}{|\mathbf{r}-\mathbf{r}'|}\right] d\mathbf{r}'. \quad (32)$$

The Fourier transform of the Coulomb potential is $\mathcal{F}\left[\frac{1}{|\mathbf{r}-\mathbf{r}'|}\right] = e^{-i\mathbf{k}\cdot\mathbf{r}'\frac{4\pi}{k^2}}$ (see appendix B). Thus, the integral in eq. (32) becomes a Fourier transformation with respect to \mathbf{r}' . Using eq. (23) on the left hand side of eq. (32) and keeping in mind that $\mathcal{F}[1] = \delta(\mathbf{k})$, one obtains

$$\hat{\rho}^{(1)}(\mathbf{k}) - n\delta(\mathbf{k}) = -\frac{nze_0^2}{k_B T} \frac{1}{k^2} \left[\frac{z}{\varepsilon\varepsilon_0} \hat{\rho}^{(1)}(\mathbf{k}) + \frac{Z}{\varepsilon\varepsilon_0} \sum_i e^{-i\mathbf{k}\cdot\mathbf{R}_i} \right] \quad (33)$$

where the Fourier transform of the density is defined as $\mathcal{F}[\rho^{(1)}(\mathbf{r})] = \hat{\rho}^{(1)}(\mathbf{k})$. The δ function in eq. (33) is neglected in the following since it contributes only for $k = 0$, i. e., $r \rightarrow \infty$. Rearranging the equation yields the Fourier transform of the counterion density determined by the macroion positions which reads

$$\hat{\rho}^{(1)}(\mathbf{k}) = -\frac{Z\kappa^2}{z(k^2 + \kappa^2)} \sum_i e^{-i\mathbf{k}\cdot\mathbf{R}_i}. \quad (34)$$

where we used the square of the inverse Debye length which reads

$$\kappa^2 = \frac{n z^2 e_0^2}{\varepsilon\varepsilon_0 k_B T}. \quad (35)$$

By back transformation of eq. (34) one gets an analytic expression for the microion density distribution $\rho^{(1)}(\mathbf{r})$ for a given macroion configuration. Here, monovalent counterions are considered with $z = 1$. Using spherical coordi-

nates, we obtain

$$\begin{aligned}\mathcal{F}^{-1}[\hat{\rho}^{(1)}(\mathbf{k})] &= \rho^{(1)}(\mathbf{r}) \\ &= \frac{1}{(2\pi)^3} Z \kappa^2 \sum_{i=1}^{N_0} \int_0^\infty dk \int_0^{2\pi} d\varphi \int_{-1}^1 d\cos\vartheta k^2 \times \\ &\quad \frac{1}{k^2 + \kappa^2} \exp(i k |\mathbf{r} - \mathbf{R}_i| \cos\vartheta).\end{aligned}\quad (36)$$

The integration over φ and $\cos\vartheta$ yields

$$\begin{aligned}\rho^{(1)}(\mathbf{r}) &= \frac{1}{(2\pi)^2} Z \kappa^2 \sum_{i=1}^{N_0} \frac{1}{i|\mathbf{r} - \mathbf{R}_i|} \times \\ &\quad \left[\int_0^\infty dk \frac{k}{k^2 + \kappa^2} \exp(i k |\mathbf{r} - \mathbf{R}_i|) - \int_0^\infty dk \frac{k}{k^2 + \kappa^2} \exp(-i k |\mathbf{r} - \mathbf{R}_i|) \right].\end{aligned}\quad (37)$$

Applying $k \rightarrow -k$ on the second integral in eq. (37), both integrals have the same integrand but different boundaries, i. e., the first from 0 to ∞ and the second from $-\infty$ to 0. Thus, they can be combined yielding an integral from $-\infty$ to ∞ . Now, the next step reads

$$\rho^{(1)}(\mathbf{r}) = \frac{1}{(2\pi)^2} Z \kappa^2 \sum_{i=1}^{N_0} \frac{1}{i|\mathbf{r} - \mathbf{R}_i|} \int_{-\infty}^\infty dk \frac{k}{k^2 + \kappa^2} \exp(i k |\mathbf{r} - \mathbf{R}_i|). \quad (38)$$

This integral can be solved via Cauchy's integral formula [18] where $\frac{1}{k^2 + \kappa^2}$ is written as $\frac{1}{(k-i\kappa)(k+i\kappa)}$. Then, the contour integral is calculated over a closed curve C on the complex plane consisting of C_1 being the real axis from $-\infty$ to ∞ and C_2 being a curve on the positive imaginary plane with infinite distance to the origin closing C . The whole curve C encloses one of the two complex poles which is at $k_0 = i\kappa$. The integral over C_2 does not contribute since the integrand in eq. (38) vanishes for $k \rightarrow \infty$. Applying the integral formula one obtains the microion density

$$\rho^{(1)}(\mathbf{r}) = \frac{Z \kappa^2}{4\pi} \sum_{i=1}^{N_0} \frac{\exp(-\kappa |\mathbf{r} - \mathbf{R}_i|)}{|\mathbf{r} - \mathbf{R}_i|} \equiv \sum_{i=1}^{N_0} \rho_i^{(1)}(\mathbf{r}) \quad (39)$$

where the last relation states that the microion distribution $\rho^{(1)}(\mathbf{r})$ can be considered as a superposition of single profiles $\rho_i^{(1)}(\mathbf{r})$ belonging to a macroion at position \mathbf{R}_i .

So far we have assumed that the macroions are point-like in order to get the result eq. (39). The finite diameter of the particles can be reintroduced via renormalizing their surface charge. To this end, we set up the constraint $\rho_i^{(1)}(\mathbf{r}) = 0$ for $|\mathbf{r} - \mathbf{R}_i| < R$ which means that the microions cannot overlap with the macroions. This constraint is combined with the condition of charge neutrality in the system which reads for monovalent counterions ($z = 1$)

$$\int_{|\mathbf{r} - \mathbf{R}_i| > R} \rho_i^{(1)}(\mathbf{r}) d\mathbf{r} = |Z|. \quad (40)$$

Note, that this only holds for small overlap of the electric double layers of the macroions, i. e., only for small particle densities which is related to the Debye-Hückel approximation [24]. Now, the macroion charge Z in the density eq. (39) is replaced by a renormalized charge Z' . Inserting eq. (39) into eq. (40) and solving the integral via spherical coordinates and integration by parts one obtains

$$Z' = |Z| \frac{\exp(\kappa R)}{1 + \kappa R} \quad (41)$$

and the final microion density distribution for a particle i reads

$$\rho_i^{(1)}(\mathbf{r}) = \frac{Z' \kappa^2}{4\pi} \frac{\exp(-\kappa |\mathbf{r} - \mathbf{R}_i|)}{|\mathbf{r} - \mathbf{R}_i|}. \quad (42)$$

The corresponding electrostatic potential $\Phi_i(\mathbf{r})$ is given by Poisson's equation $\nabla^2 \Phi_i(\mathbf{r}) = -(e_0 \rho_i^{(1)}(\mathbf{r})) / (\varepsilon \varepsilon_0)$ and reads

$$\Phi(\mathbf{r}) = \sum_{i=1}^{N_0} \frac{Z' e_0}{4\pi \varepsilon \varepsilon_0} \frac{\exp(-\kappa |\mathbf{r} - \mathbf{R}_i|)}{|\mathbf{r} - \mathbf{R}_i|} \equiv \sum_{i=1}^{N_0} \Phi_i(\mathbf{r}). \quad (43)$$

Now, coming back to the effective potential of the whole system (see eq. (12)), we are interested in the contribution which depends on the macroion positions. Again, we restrict the model to one species ν and set $\rho_Z(\mathbf{r}) = z \rho^{(1)}(\mathbf{r})$. Inserting the grand potential eq. (25) into eq. (12) and replacing $\phi(\mathbf{r}) = z e_0 \Phi^{ext}(\mathbf{r})$ yields

$$\begin{aligned} V_{eff}(\{\mathbf{R}_i\}) &= V_{00}(\{\mathbf{R}_i\}) + V_0 + \int z e_0 \Phi^{ext}(\mathbf{r}) \rho^{(1)}(\mathbf{r}) d\mathbf{r} \\ &= V_{00}(\{\mathbf{R}_i\}) + V_0 + \sum_{i=1}^{N_0} \sum_{j=i+1}^{N_0} v_{eff}(|\mathbf{R}_i - \mathbf{R}_j|) \end{aligned} \quad (44)$$

where V_0 is a structure-independent term which does not influence the forces acting between the macroions. The effective interaction potential $v_{eff}(|\mathbf{R}_i -$

$\mathbf{R}_j|)$ between two macroions, which is given in eq. (44) as an convolutional integral [18], can be simplified via Fourier transformation. To this end, one needs the Fourier transformations of the Coulomb and the Yukawa potential which are given in appendix B. Inserting the Coulomb potential given in eq. (29) and the microion density distribution eq. (42) into the convolution in eq. (44) yields

$$v_{eff}(|\mathbf{R}_j - \mathbf{R}_i|) = -\frac{Z'^2 e_0^2 \kappa^2}{16\pi^2 \varepsilon \varepsilon_0} \int \frac{\exp(-\kappa|\mathbf{r} - \mathbf{R}_i|)}{|\mathbf{r} - \mathbf{R}_i|} \frac{1}{|\mathbf{r} - \mathbf{R}_i|} d\mathbf{r}. \quad (45)$$

Note, that for the inserted Coulomb potential the charge Z was exchanged by Z' due to the finite radius of the particles corresponding to eq. (41). The Fourier transformation of this convolutional integral is the product of the Fourier transforms of both functions given in eq. (191) and eq. (192) in appendix B which yields the effective potential in k -space

$$\hat{v}_{eff}(\mathbf{k}) = -\frac{Z'^2 e_0^2 \kappa^2}{\varepsilon \varepsilon_0} \frac{1}{k^2(k^2 + \kappa^2)}. \quad (46)$$

The back transformation of eq. (46) with respect to $\mathbf{R}_j - \mathbf{R}_i$ yields an integral which can be solved in spherical coordinates. Therefore, the residue theorem is used where the integral is taken over a closed path on the complex plane and the real axis. Note, that the denominator in eq. (46) can be rewritten as $k^2 + \kappa^2 = (k + i\kappa)(k - i\kappa)$. It is necessary to extent the k integration from $-\infty$ to ∞ . Otherwise the integrand would not vanish on the complex plane. This finally gives the effective potential of two macroions at \mathbf{R}_i and \mathbf{R}_j surrounded by microions

$$v_{eff}(|\mathbf{R}_j - \mathbf{R}_i|) = W \frac{\exp(-\kappa|\mathbf{R}_j - \mathbf{R}_i|)}{|\mathbf{R}_j - \mathbf{R}_i|} \quad (47)$$

with the coupling parameter

$$W = \frac{Z'^2 e_0^2}{4\pi \varepsilon \varepsilon_0} \quad (48)$$

where the effective valency Z' is given in eq. (41). As a last step we rewrite the inverse Debye length κ given in eq. (34). In a more general case, different species of counterions can be contained in the fluid which we refer to as salt ions. They have been neglected during the derivation of eq. (47). Then, κ can be written as

$$\kappa^2 = \frac{1}{\varepsilon \varepsilon_0 k_B T} \left(n(z e_0)^2 + \sum_k n_k (z_k e_0)^2 \right) \quad (49)$$

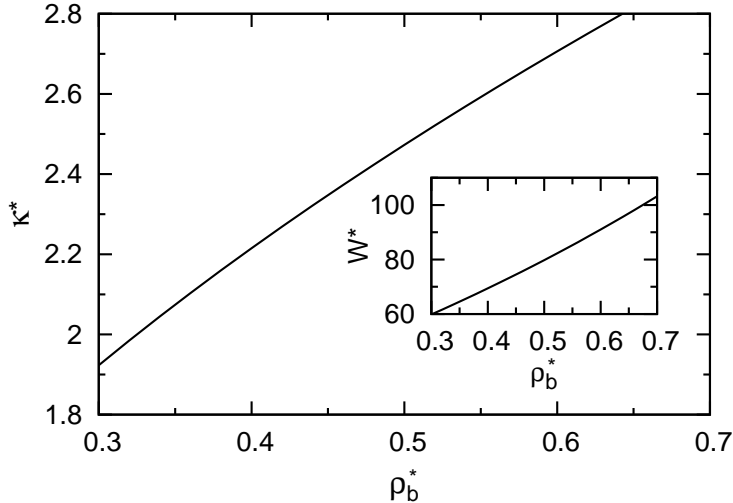


Figure 2: Dimensionless values for the inverse Debye length κ^* and the DLVO coupling parameter W^* (inset) as functions of the bulk density ρ_b^* .

where the subscript k stands for different species of salt ions. Assuming univalent microions ($|z| = 1$) the charge neutrality between macro- and microions requires $n = |Z|\rho$ with the macroion density ρ . Furthermore we define the ionic strength $I = (1/2) \sum_k n_k z_k^2$ which yields

$$\kappa = \sqrt{\frac{e_0^2}{\varepsilon \varepsilon_0 k_B T}} (Z\rho + 2IN_A). \quad (50)$$

The inverse Debye length κ given in eq. (50) and the DLVO coupling parameter W given in eq. (48) are plotted within the density range of interest in fig. 2. The system parameters $\sigma = 26nm$, $Z = 35$, $T = 298K$, $\varepsilon = 78.5$, and $I = 10^{-5}mol/l$ are consistent with the experimental setup. From fig. 2 it can be concluded that κ is a state-dependent quantity. In more detail, the screening increases with density since there are more counterions per volume in the solvent. Therefore also the coupling parameter increases with density due to the implicit dependence $\kappa(\rho)$.

2.3 Soft-core potential

In order to mimic experimental conditions where suspensions of charged silica spheres are used, the DLVO potential is supplemented by a short-ranged soft core. It describes the steric repulsion of the particles which possess a finite volume. In more detail, the core can induce freezing transitions at

smaller densities than without core, even in the case of an overlayed long-rang potential as, e. g., a Yukawa interaction. To this end, the repulsive part of the LJ potential is taken as a soft sphere potential reading

$$u_{SS}(r) = 4\epsilon_{SS} \left(\frac{\sigma}{r}\right)^{12} \quad (51)$$

with the core diameter σ being the same value as the effective diameter used in the DLVO potential. The precise form of the core seems not to be essential but yields only minor quantitative differences in the behavior of the suspension. Another possibility is a hard sphere core with diameter σ . Combined with Yukawa potentials, i. e. hard-core Yukawa (HCY), this was used in former studies [104, 65]. In the present work, we assume $\epsilon_{SS}/(k_B T) = 1$.

2.4 Derjaguin approximation

The description of the interaction between two surfaces is an important issue in statistical physics. However, the geometry and the specific potential often yield differential equations which are hardly solvable. In sec. 2.2 linearized PB theory was used to determine DLVO interactions between spherical particle of finite volume. In some cases it is reasonable to apply DA, namely if the radius of curvature compared to the interaction range of the surfaces is large. In the spirit of DLVO theory this is the case for thin electric double layers. Following Derjaguin's work the approximation is discussed in this section and related to important physical quantities [27, 110].

We consider two adjacent, curved surfaces Σ_1 and Σ_2 . The centers of curvature radii are located on the z -axis of the coordinate system. Thus, the points of closest distance h of the surfaces is also located on the z -axis whereas the x - y -plane is parallel to the tangential planes at these points. The surface Σ_1 is defined by the curvatures K_1 and K'_1 whereas Σ_2 is defined by K_2 and K'_2 . For small curvatures the points on Σ_i with coordinates z_1 and z_2 can be expanded as

$$z_1 = -\frac{1}{2} (K_1 x^2 + K'_1 y^2) \quad (52)$$

$$z_2 = h + \frac{1}{2} (K_2 x^2 + K'_2 y^2) \quad (53)$$

neglecting terms of third and higher order. Obviously, the distance of facing

points (or surface elements) is

$$\begin{aligned}
H &= z_2 - z_1 \\
&= h + \frac{1}{2}(K_1 + K_2)x^2 + \frac{1}{2}(K'_1 + K'_2)y^2 \\
&= h + \frac{1}{2}Kx^2 + \frac{1}{2}K'y^2
\end{aligned} \tag{54}$$

where the curvatures $K = K_1 + K_2$ and $K' = K'_1 + K'_2$ are defined. Here, we introduce the assumption that only facing points with same x and y , whose distance is given in eq. (54), interact with each other. This is reasonable since the interaction energy of non-facing surface elements (with larger distances) should be small due to the short range of the potential as compared to the surface distance. Hence, the interaction energy F can be calculated by integrating the interaction energy per unit area $f(H)$ reading

$$F(h) = \int \int f \left(h + \frac{1}{2}Kx^2 + \frac{1}{2}K'y^2 \right) dx dy. \tag{55}$$

where the integration has to be evaluated over the area given by the projection of the surfaces onto the x - y -plane (assuming each point on Σ_1 has a facing point on Σ_2). Due to the short-range character of f used before, it is possible to extend these integration boundaries to infinity since these points do not contribute. Introducing polar coordinates in the form

$$x = \frac{\rho}{\sqrt{K}} \cos \vartheta \tag{56}$$

$$y = \frac{\rho}{\sqrt{K'}} \sin \vartheta \tag{57}$$

equation (55) becomes

$$F(h) = \int_0^{2\pi} \int_0^\infty f \left(h + \frac{1}{2}\rho^2 \right) \frac{\rho d\rho d\vartheta}{\sqrt{KK'}}. \tag{58}$$

As a second substitution, we use the argument of f as the new variable $H = h + (1/2)\rho^2$, which corresponds to eq. (54). This yields the much simpler form

$$F(h) = \frac{2\pi}{\sqrt{KK'}} \int_h^\infty f(H) dH \tag{59}$$

where the integration over ϑ was carried out. Together with the extension of the integration boundaries to infinity, eq. (59) is the well-known Derjaguin

approximation. In the special case of a spherical particle with radius R and a planar wall possessing curvatures $K_1 = K'_1 = 1/R$ and $K_2 = K'_2 = 0$, respectively, eq. (59) becomes

$$\frac{F(h)}{2\pi R} = \int_h^\infty f(H)dH \quad (60)$$

where the definitions of K and K' in eq. (54) were used. The interaction energy per unit area $f(H)$ is related to the pressure tensor component P_{zz} (or stress tensor component $\tau_{zz} = -P_{zz}$) in the form [110]

$$f(H) = P_{zz}(H) - P_{bulk} \quad (61)$$

where P_{bulk} is the bulk pressure of the fluid without the confining surfaces. Equation (61) implies that the interaction energy per unit area is the excess pressure exerted by the confining surfaces, which can be computed directly by computer simulations as, e. g., with the MC method. Furthermore, the left-hand side of eq. (60) is an important quantity since $F(h)/R$ is accessible experimentally using SFA [66] or CP-AFM [32]. Thus, eq. (60) and eq. (61) is a key expression since it relates experiment and simulation.

2.5 Uncharged, unstructured walls

Confining surfaces are of interest for investigating inhomogeneous systems. A simple (short-ranged) soft-wall potential neglecting surface charges and surface structures is derived in the following. The solid wall is modeled as a fcc lattice of atoms interacting via LJ potentials. This is a very simple but, on a mesoscopic scale, an appropriate choice. The (100)-plane of it with infinite expansion in x and y direction is taken as the surface of the wall where the surface normal is parallel to the z axis. Since in experiments usually the confining substrate is much thicker than the size of the confined space it is appropriate to assume an infinite number of (100)-planes on top of each other. A unit cell of the (100)-plane contains 2 particles yielding a mean area density of $n_A = 2/l^2$. Starting from the LJ potential for one particle

$$u^{LJ}(r) = 4\varepsilon_w \left\{ \left(\frac{\sigma}{r_{ij}} \right)^{12} - \left(\frac{\sigma}{r_{ij}} \right)^6 \right\} \quad (62)$$

with the coupling parameter ε_w , the particle diameter σ , and the particle-particle distance $r_{ij} = |\mathbf{r}_i - \mathbf{r}_j|$ with $\mathbf{r} = (x, y, z)^T$, the potential for a (100)-monolayer is calculated via integration. Here we consider an upper and a

lower wall located at $z' = \pm s_z/2$ and the two potentials of a monolayer read

$$\begin{aligned} u_{fs}^{LJ,mono}(z) &= \int_{-\infty}^{\infty} \int_{-\infty}^{\infty} dx' dy' n_A u^{LJ}(|\mathbf{r} - \mathbf{r}'|) \\ &= 4\pi\varepsilon_w n_A \sigma^2 \left(\frac{1}{5} \left[\frac{\sigma}{z \mp s_z/2} \right]^{10} - \frac{1}{2} \left[\frac{\sigma}{z \mp s_z/2} \right]^4 \right) \end{aligned} \quad (63)$$

where the index fs denotes the fluid-solid interaction. Extending these monolayers to infinity by building up an fcc lattice is done the same way using the length density $n_L = 2/l$. Using eq. (63) the integration yields

$$\begin{aligned} u_{fs}^{LJ} &= \pm \int_{\pm s_z/2}^{\infty} n_L u_{fs}^{LJ,mono}(z - z') \\ &= \mp \frac{2}{3} \pi \varepsilon_w n_V \sigma^3 \left(\frac{2}{15} \left[\frac{\sigma}{z \mp s_z/2} \right]^9 - \left[\frac{\sigma}{z \mp s_z/2} \right]^3 \right) \end{aligned} \quad (64)$$

where $n_V = n_A n_L$. In the following the attractive part of the integrated LJ wall eq. (64) is neglected. This yields a soft-wall (SW) potential which reads

$$u_{fs}^{SW} = \mp \frac{4}{45} \pi \varepsilon_w n_V \sigma^3 \left[\frac{\sigma}{z \mp s_z/2} \right]^9 \quad (65)$$

In the present work, we assume $n_V \sigma^3 = 1$ and $\varepsilon_w/(k_B T) = 1$.

2.6 Screened, charged walls

Confining, charged surfaces are common in experimental setups [63, 99, 116] and therefore of great interest for theoretical studies [117, 25, 79, 35]. The simple soft-wall potential in eq. (65) which models the “pure“ confinement fails to predict some experimental results including different wall materials [45]. The reason is that, in general, the confining surfaces which are in contact with the solvent are charged. This is a consequence of the dissociation of counterions from these walls. Figure 3 is a sketch of the modified model [45]. These additional ions may modify the fluid-wall and the fluid-fluid interaction since they change the screening of charges between the interacting particles and between particles and walls. Since the screening is an inhomogeneous effect it is reasonable to consider the distribution of wall counterions between two charged walls. To this end, we employ the exact (non-linearized) PB theory (see sec. 2.1) for a system without salt ions or macroions. In this

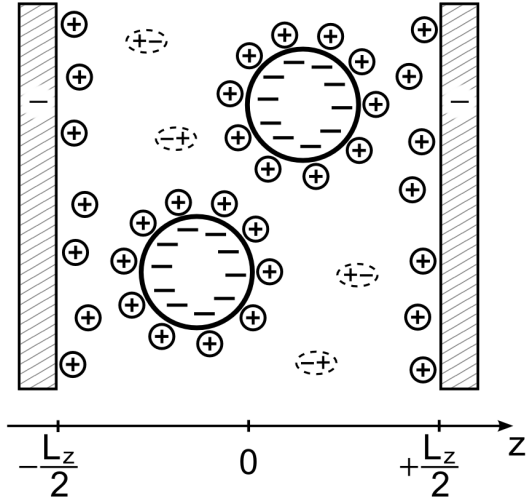


Figure 3: Illustration of the model system, involving negatively charged colloids, positively charged counterions and salt (indicated by the ellipses) between negatively charged plates separated by distance L_z . Wall counterions dissociating from the like-charged walls are located within a thin layer next to the walls.

case, the PB equations eq. (1) and eq. (2) can be solved analytically, yielding the following counterion profile [33]

$$\rho_{cw}(z) = \rho_0 \frac{2\gamma_0^2 / (\kappa_0 L_z / 2)^2}{\cos^2(\gamma_0(1 - 2z/L_z))}. \quad (66)$$

In eq. (66), ρ_0 is the mean density of counterions between the two walls, κ_0 is the corresponding Debye parameter, and γ_0 is determined by the condition

$$\frac{(\kappa_0 L_z / 2)^2}{2\gamma_0} - \tan \gamma_0 = 0. \quad (67)$$

For typical experimental conditions considered here, it follows from eqs. (66) and (67) that most of the counterions are located near the charged walls, whereas in the center of the slit pore the distribution has a minimum with small or almost vanishing ρ_{cw} (see fig. 4a and b). However, taking macroions or salt ions into account, the counterion profile eq. (66) is only an approximation. The additional ions would influence the counterion distribution. On one hand, the macroions, which possess a finite volume, would squeeze the counterions towards the walls due to the decreased available volume. On the other hand, their (screened) surface charge would attract the wall counterions. Furthermore, the counterions dissociated from the macroions and the

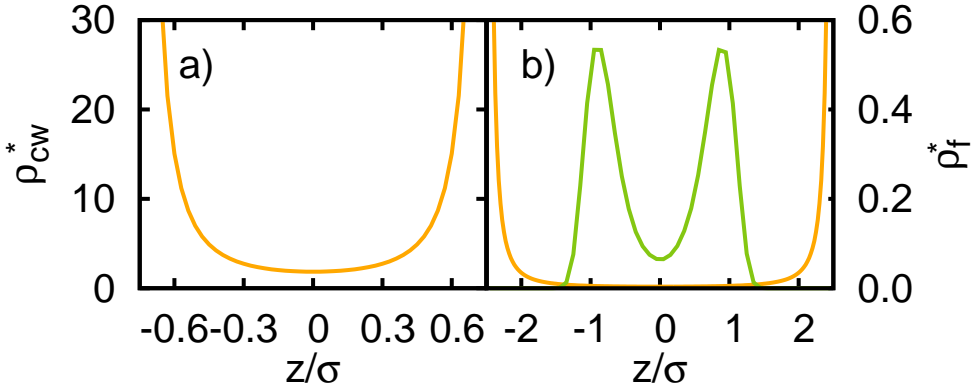


Figure 4: Wall counterion profiles $\rho_{cw}^* = \rho_{cw}\sigma^3$ (orange lines) between charged silica walls ($\psi_S = -80\text{mV}$) determined from exact PB theory using eq. (66) for a) $L_z = 1.5\sigma$ and b) $L_z = 5.0\sigma$. Additionally, the macroion density profile $\rho_f^* = \rho_f\sigma^3$ (green line) for a bulk density $\rho_b^* = 0.2$ is plotted in (b). Note, that in (a) all macroions are squeezed out of the pore at ρ_b considered.

salt ions would interact with them as well. However, neglecting these effects is an appropriate approximation since we think that the qualitative behavior of the wall counterions will not be affected. In more detail, the counterions will localize near the walls even in the presence of macroions.

Thus, considering a typical macroion distribution between the walls, we see that ρ_{cw} mainly influences the fluid-wall interaction but not the fluid-fluid interaction since between two macroions the wall counterion density is small (see fig. 4b). This is supported by numerical simulations [26] where such additional fluid-fluid contributions only yield marginal effects on the local density profiles of the macroions. The impact on the fluid-fluid interaction is discussed in sec. 5.4. The insertion of macroions, which are surrounded by counterions themselves, will change this wall counterion distribution. In [25] the impact of overlapping counterion clouds is discussed. However, we neglect this effect and assume its impact on the system to be small, especially at the parameter range considered. One related effect is the expulsion of salt ions from the slit pore, called Donnan effect [90] which is neglected here as well. However, the agreement of experimental and simulation results for the wavelengths of solvation forces in our previous studies [74, 75] justifies these assumptions.

Starting from PB theory (see sec. 2.1) and using the linear superposition approximation (LSA) [119, 78, 13] and DA discussed in sec. 2.4, one can find a screened interaction potential for thin electric double layers between a charged flat surface (wall) and a charged sphere (particle in the fluid). The

LSA is a widely used approximation which linearly superposes the potentials of two facing surfaces assuming that on the midplane (between the surfaces) the potentials are negligibly small.

Consequently, the potential of a slit-pore consisting of two parallel charged walls is constructed by superposing both fluid-solid interaction potentials. In this paragraph, we sketch the main steps leading to the final fluid-wall potential, following former studies [119, 78, 13, 14]. The consideration starts with the electrostatic potential $\phi(z)$ of two plane parallel, infinitely extended, charged surfaces normal to the z -direction. the two plates possess constant surface potentials ψ_1 and ψ_2 , and they are separated by a distance h . Due to the surfaces charges and the electric double layers consisting of the dissociating counterions (assumed to be monovalent), the potential is given by the exact PB equation

$$\frac{\partial^2 \phi(z)}{\partial z^2} = \frac{c_0 e_0}{\varepsilon \varepsilon_0} \sinh \frac{e_0 \phi(z)}{k_B T}. \quad (68)$$

The solution of eq. (68) yields an expression for the free energy of the electric double layers from which the force at the mid-plane acting on the plates can be determined. However, the solution involves elliptic integrals. A strong simplification is reached by assuming a large separation h between the plates. In other words, the range of the electrostatic potential of a single surface in absence of the other one is short compared to h . Then, the single surface potentials ϕ_1 and ϕ_2 can be superposed [119, 28, 78, 13, 46, 14], i. e. $\phi(z) = \phi_1(z) + \phi_2(z)$, called LSA in literature. Due to the small value of the potential ψ_m on the mid-plane between the plates, the solution of eq. (68) can be expanded in powers of $\exp(-\psi_m)$. Combining this with the superposition, the resulting interaction energy per unit area in case of monovalent ions reads

$$f_{CP,LSA} = 32 \varepsilon \varepsilon_r \kappa \gamma_1 \gamma_2 \left(\frac{k_B T}{e_0} \right)^2 \exp(-\kappa h) \quad (69)$$

with $\gamma_i = \tanh(e_0 \psi_i / 4k_B T)$. The subscript CP is referred to the constant surface potential condition. The interaction between a planar surface and a sphere of diameter σ is derived by applying DA to eq. (69), where eq. (60) is used with $R = \sigma/2$, yielding

$$u_{FS}^{LSA,DA}(z) = 64 \pi \varepsilon_0 \varepsilon \gamma_F \gamma_S \frac{\sigma}{2} \left(\frac{k_B T}{e_0} \right)^2 \exp \left(-\kappa_W(z) \left(z - \frac{\sigma}{2} \right) \right), \quad (70)$$

where the surface distance is replaced by the distance between plate and center of the sphere, i. e. $h = z - \sigma/2$. The subscript F is used for the spherical particle in the fluid suspension and S is used for the solid plane

surface. Keep in mind, that in eq. (70) we set the screening parameter $\kappa = \kappa_W$ including wall counterions.

Note, that eq. (70) is a rough approximation since both LSA and DA neglect higher order curvature effects [14, 15], i. e. they are precise for large particles. Furthermore, LSA is a good approximation for large separations between the surfaces (or thin electric double layers) [78], whereas DA is appropriate for small distances. Also DA is valid for thin electric double layers and short interaction ranges including weak overlap of the double layers, which is characterized by large enough κ . This finally yields a range of validity in an intermediate distance range. A further limitation is the surface potential ψ_i which in case of too large values yields significant deviations for the forces between the surfaces since for large interaction ranges the superposition approximation becomes obscure [13]. However, the additional wall counterions in eq. (70) yield a larger screening between wall and particle described by the screening parameter κ_W . Thus, the interaction ranges are even smaller as compared to interactions without wall counterions. Due to the fact that this study considers screening strengths $\kappa_W > \kappa \gtrsim 1$, the electric double layers of the particles and the surfaces are of intermediate or short range. Thus, the assumptions made will cause deviations, i. e. they will result in an overestimation of the interaction energy between plane surface and sphere [14, 15]. However, we expect only quantitative deviations, whereas the investigation of charged walls in this study focuses on qualitative properties.

The original version of eq. (70) derived in [15] uses a screening parameter equal to the bulk screening κ . However, as motivated before the fluid-wall interaction is changed by additional counterions. We take this into account by using the modified screening strength $\kappa_W(z)$ in eq. (70). The z -dependence of κ_W is a consequence of the inhomogeneity of eq. (66). To derive an expression for κ_W we consider a charged spherical particle and a charged flat wall with a distance z . Since the screening of the fluid-wall interaction is determined by all wall counterions between them we assume that it can be described by the mean density of these ions

$$\bar{\rho}_{cw} = \frac{1}{z} \int_0^z \rho_{cw}(z') dz' \quad (71)$$

which is the average of the local density profile of the counterions in this distance z . Due to the strong localization of the counterions at the wall as illustrated in fig. 4 the limit of the integral can be extended to infinity,

yielding

$$\bar{\rho}_{\text{cw}} \approx \frac{1}{z} \int_0^\infty \rho_{\text{cw}}(z') dz'. \quad (72)$$

On the other hand, to fulfill the electroneutrality condition all wall counterions dissociated to the solvent must compensate the wall charge. The corresponding expression reads

$$|\sigma_S| = \int_0^\infty \rho_{\text{cw}}(z') e_0 dz'. \quad (73)$$

The surface charge density σ_S can be calculated via the Grahame equation (see. eq. (7)) and is therefore determined by the surface material and the ion concentration of the solvent. Combining eqs. (72) and (73) yields the expression

$$\bar{\rho}_{\text{cw}} = \frac{|\sigma_S|}{e_0 z} \quad (74)$$

which relates the mean counterion density at the wall and the surface charge density. According to the definition of the screening parameter (see eq. (50)), the mean density given in eq. (74) makes a contribution to the screening of the fluid-wall interaction of eq. (70). Thus, the fluid-wall screening parameter is set to

$$\kappa_W(z) = \sqrt{\frac{e_0^2}{\varepsilon_0 \varepsilon k_B T} \left(Z\rho + 2IN_A + \frac{|\sigma_S|}{e_0 z} \right)}. \quad (75)$$

Upon increasing the distance z from the wall, $\kappa_W(z)$ approaches the bulk value κ which is consistent to the vanishing wall counterion density at large distances. However, the fluid-wall potential vanishes anyway within this limit due to the exponential decay. On the other hand, eq. (75) shows that approaching the wall yields an enhancement of the screening.

The advantage of our approach is that it involves a one-wall potential, which can be superposed yielding a charged slit pore as considered in the present work. This assumption is motivated by the fact that at the wall separations considered, the electric double layers (wall counterion distributions) do overlap only slightly. Moreover, a recent study showed that the LSA used for eq. (70) even holds for small overlap [80].

The modification in the screening parameter introduced in our former study [45] yields a non-monotonic behavior of the repulsion range of the fluid-wall interaction visualized in fig. 5a. Starting from an uncharged wall the repulsion increases for increasing wall charge. At a certain point, the

screening strength κ_W , which is increasing as well, begins to dominate the electrostatic repulsion. Hence, the repulsion range decreases for increasing wall charge above this point. As we have shown in [45] this non-monotony yields a behavior of force-distance curves consistent with the experiment.

In order to elucidate the advantage of our model it is reasonable to compare it with other interaction potentials suggested in literature which is discussed in the following (see [45] for more details). The most simple ansatz for screened charged walls is based on an integrated Yukawa-like interaction (called here 'model I') [45] and reads

$$u_I(z) = W_S \exp\left(-\kappa\left(\frac{L_z}{2} - z\right)\right) + W_S \exp\left(-\kappa\left(\frac{L_z}{2} + z\right)\right) \quad (76)$$

where the influence of wall counterions is only taken into account in the coupling parameter W_S . It totally neglects their impact on the screening. As a consequence, the repulsion range increases monotonically with surface charge (see fig. 5b). There are other models for charge walls with a similar behavior. One is given via linearized Poisson-Boltzmann which reads (called here 'model II') [52]

$$u_{II}(z) = Z\psi_S \frac{\cosh(\kappa z)}{\sinh(\kappa L_z/2)} \quad (77)$$

which is shown in fig. 5c for varying wall charges. Another ansatz derived from exact Poisson-Boltzmann theory [26, 4] (called here 'model III') reads

$$u_{III}(z) = -\frac{2k_B T}{|e_0|} \ln \cos\left(\gamma_0\left(1 - \frac{2z}{L_z}\right)\right). \quad (78)$$

where γ_0 is defined by eq. (67). Model III is shown in fig. 5d as well. Both models are derived for a two-wall system and are not a superposition of single-wall potentials as in the model used here. However, they yield the same qualitative behavior as the simple ansatz eq. (76) with monotonically increasing repulsion for increasing wall charge whereas our modified fluid-wall potential eq. (70) yields non-monotonicity. Regarding recent AFM results [45] where an charge-induced enhancement of the force amplitude was observed, model I, II and III are not appropriate to explain these results, whereas our model does. Additionally, we compared these models with a simplification of eq. (70) averaging out the z -dependence of the screening parameter eq. (75), i. e. it is assumed that the wall counterions distribute homogeneously between the charged surfaces. In this case (plotted in fig. 5e) a non-monotonicity of the repulsion is observed as found for inhomogeneously distributed wall counterions. This emphasizes the importance of wall counterions for the screening of the fluid-wall interaction whereas the distribution of the counterions within the pore is less important and yields (minor)

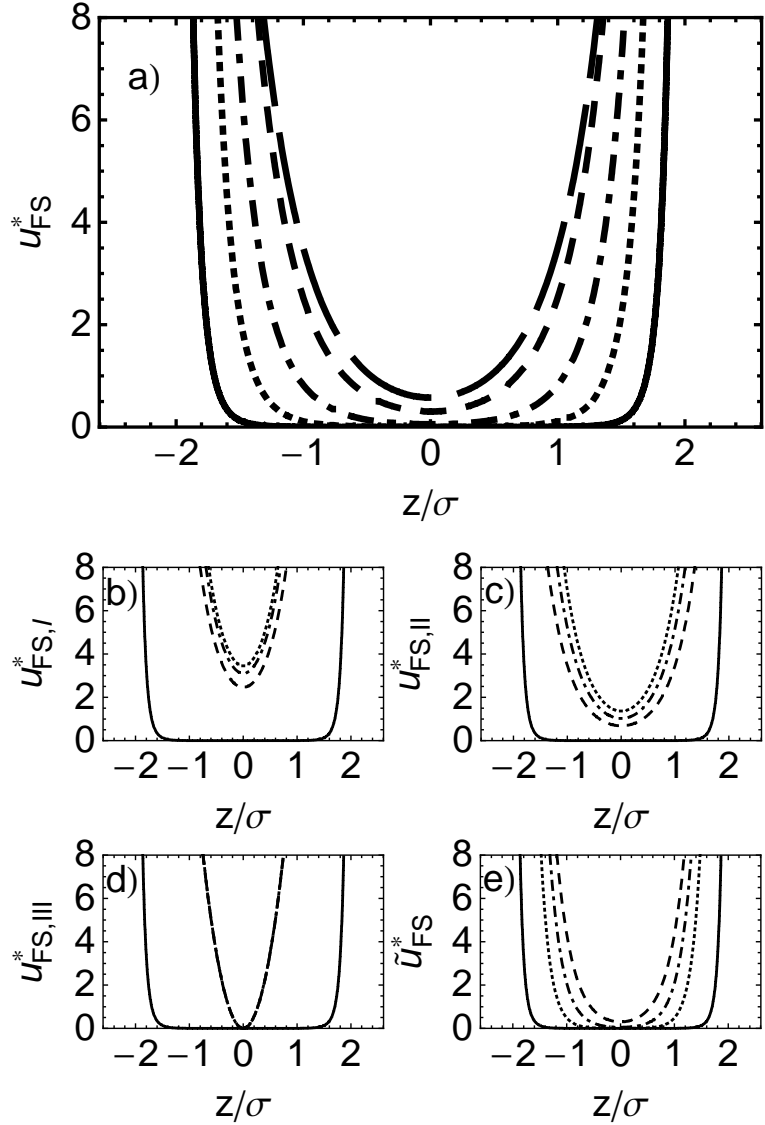


Figure 5: Illustration of various fluid-wall potentials ($u_{FS}^* = \beta u_{FS}$) for charged colloids between two like-charged walls [all plots include the soft-wall contribution defined in eq. (65)]. The data correspond to the wall separation $L_z = 5\sigma$, macroion density $\rho_b\sigma^3 = 0.44$, and the surface potentials $\psi_S = 0$ (solid line), $\psi_S = -40mV$ (long-dashed, only in (a)), $\psi_S = -80mV$ (dashed), $\psi_S = -120mV$ (dot-dashed), and $\psi_S = -160mV$ (dotted). (a) Our model, (b) model I, (c) model II, (d) model III, and (e) our model with pore averaged κ_W (see main text).

quantitative changes. However, a homogeneous distribution would yield additional screening contributions to the fluid-fluid interaction. Therefore, we use the more reasonable, inhomogeneous wall counterion distribution given in eq. (66).

2.7 Model system for binary mixture of screened, charged particles

Most of the thesis is devoted to suspensions containing only one type of macroions. In chapter 7 we extend the discussion to binary mixtures of charged particles. Binary mixtures consisting of particles with different sizes and charges are modeled via pairwise Yukawa interactions based on DLVO theory (see sec. 2.2). To this end species A and B are considered. All interactions, especially the cross-interactions between A and B , are assumed to be pairwise additive, i. e. the Berthelot mixing rule is applied [59]. Former studies investigated deviations from additivity by introducing an additional factor for the coupling constant of the cross terms. This non-additivity yields, e. g., fluid-fluid demixing (macrophase separation) [59, 5] or mixing and microphase separation [5]. In particular, it is known that dusty plasmas exhibit macrophase separation [68]. The difference to plasmas is that in colloidal suspensions the surface charges are compensated by counterions attached to the surface and the acting force is determined by their renormalized charge, whereas in plasmas the screening is determined by free electrons [68].

Here, we focus on colloidal mixtures without non-additivity. The pairwise additive interactions read

$$u_{DLVO}^{(ij)}(r) = W^{(ij)} \frac{\exp(-\kappa r)}{r}, \quad (79)$$

$$W^{(ij)} = \frac{\tilde{Z}^{(i)} \tilde{Z}^{(j)} e_0^2}{4\pi \varepsilon_0 \varepsilon} \exp\left(\kappa \left(\frac{\sigma_i + \sigma_j}{2}\right)\right), \quad (80)$$

$$\tilde{Z}^{(i)} = \frac{Z^{(i)}}{1 + \kappa \sigma_i / 2} \quad (81)$$

with $i, j \in \{A, B\}$, the coupling parameters $W^{(ij)}$, the renormalized valencies $\tilde{Z}^{(i)}$, and the particle diameters σ_i . For each pair (ij) the screening parameter κ is constant containing the ions of all particle species. On the scale of the average macroion distance it is an appropriate assumption for the fluid-fluid interaction that the counterions are distributed homogeneously. Hence, the

inverse Debye length reads

$$\kappa = \sqrt{\frac{e_0^2}{\varepsilon_0 \varepsilon k_B T} \left(\sum_j Z^{(j)} \rho^{(j)} + 2IN_A \right)} \quad (82)$$

where monovalent counterions ($|z_c^{(j)}| = 1$) and charge neutrality between counter and macroions ($|z_c^{(j)}| \rho_c^{(j)} = \rho_c^{(j)} = |Z^{(j)}| \rho^{(j)}$) is assumed (see sec. 2.2).

The particles are supplemented by a short-ranged soft core being the repulsive part of the LJ potential (see sec. 2.3). Applying Berthelot's mixing rule, this soft-sphere potential reads

$$u_{SS}^{(ij)}(r) = 4\varepsilon_{SS} \left(\frac{\sigma_i + \sigma_j}{2r} \right)^{12}. \quad (83)$$

Finally, the total interaction potential for the mixture is

$$u^{(ij)}(r) = u_{SS}^{(ij)}(r) + u_{DLVO}^{(ij)}(r). \quad (84)$$

3 Principles from statistical mechanics and thermodynamics: Investigation of structure and phase behavior

3.1 Canonical ensemble

A *canonical ensemble* consists of all possible states in a system with constant volume, temperature, and particle number. The system only exchanges heat with a surrounding reservoir which guarantees the consistency of the temperature [52, 39]. The system boundaries are not penetrable for particles. They are characterized by constant values of particles N , volume V , and temperature T , whereas the energy can fluctuate. Thus, the canonical ensemble is determined by a fixed density ρ . The equilibrium probability density of finding a configuration $\{\mathbf{r}^N\}$ of certain energy is given by the Boltzmann factor and reads

$$f^{[N]}(\mathbf{r}^N, \mathbf{p}^N) = \frac{1}{h^{3N} N!} \frac{\exp(-\beta H(\mathbf{r}^N, \mathbf{p}^N))}{Q_N} \quad (85)$$

with the Hamiltonian $H(\mathbf{r}^N, \mathbf{p}^N)$. The constant Q_N , which normalizes $f^{[N]}$ by counting all possible states of the ensemble, is the canonical partition function

$$Q_N = \frac{1}{h^{3N} N!} \int \int \exp(-\beta H(\mathbf{r}^N, \mathbf{p}^N)) d\mathbf{r}^{3N} d\mathbf{p}^{3N}. \quad (86)$$

If the Hamiltonian H can be written in the form $H(\mathbf{r}^N, \mathbf{p}^N) = E_{kin}(\mathbf{p}^N) + E_{pot}(\mathbf{r}^N)$, i. e. kinetic energy E_{kin} and potential energy E_{pot} are separable, the integration of the momenta \mathbf{p}^N can be carried out analytically. Introducing the de-Broglie thermal wavelength

$$\Lambda = \sqrt{\frac{h^2}{2\pi m k_B T}} \quad (87)$$

the partition function eq. (86) simplifies to

$$Q_N = \frac{1}{\Lambda^{3N} N!} \int \exp(-\beta E_{pot}(\mathbf{r}^N)) d\mathbf{r}^{3N} \quad (88)$$

where the integral is called *configurational integral* since it only depends on the configuration $\{\mathbf{r}^N\}$. The corresponding probability density reads

$$f^{[N]}(\mathbf{r}^N) = \frac{1}{\Lambda^{3N} N!} \frac{\exp(-\beta E_{pot}(\mathbf{r}^N))}{Q_N}. \quad (89)$$

Whereas eq. (86) is in the spirit of statistical mechanics, the Helmholtz free energy

$$F = U - TS \quad (90)$$

is the thermodynamic counterpart where the link between both is given by

$$F = -k_B T \ln Q_N. \quad (91)$$

Via the Gibbs fundamental equation and the differential form of eq. (90), the thermodynamic functions entropy S , pressure P , chemical potential μ , and internal energy U are given as derivatives of F with respect to T , V , N , and $1/T$ [52]. If the probability distribution eq. (85) is given, the ensemble average of an observable can be determined. The latter is defined for an arbitrary function $B(\mathbf{r}^N, \mathbf{p}^N)$ by

$$\langle B \rangle = \int \int B(\mathbf{r}^N, \mathbf{p}^N) f^{[N]}(\mathbf{r}^N, \mathbf{p}^N) dr^{3N} dp^{3N}. \quad (92)$$

The first equality in eq. (93) is the ensemble average of the internal energy U (assuming separability of kinetic and potential energy). Comparing this with eq. (88) it follows that the ensemble average is also given as the derivative of Q_N . For energy and pressure this reads

$$U = \frac{1}{\Lambda^{3N} N! Q_N} \int E_{pot} \exp(-\beta E_{pot}) dr^{3N} = - \left(\frac{\partial \ln Q_N}{\partial \beta} \right)_V, \quad (93)$$

$$P = k_B T \left(\frac{\partial \ln Q_N}{\partial V} \right)_{NT}, \quad (94)$$

$$\mu = -k_B T \left(\frac{\partial \ln Q_N}{\partial N} \right)_{VT}. \quad (95)$$

In practice, the free energy (or the partition function) cannot be determined directly in computer simulations. However, the Monte-Carlo method is able to calculate derivatives of $\ln Q_N$ with respect to an independent variable or a parameter containing it, i. e., β , V , or N in the canonical ensemble. These derivatives are given in eqs. (93), (94), and (95) yielding the ensemble averages of the thermodynamic functions U , P , and μ . The latter are simply integrals over phase space and can be computed within MC by sampling the phase space over an appropriate set of (uncorrelated) states of an ensembles NVT (see sec. 4.4). This shows that the sampling of the ensemble average is related with the sampling of the partition function.

3.2 Grand canonical ensemble

The set of all possible states with fixed chemical potential μ , volume V , and temperature T is called *grand canonical ensemble* [52, 110]. In contrast to the canonical ensemble of sec. 3.1 the particle number can fluctuate. This is realized for subsystems in contact with each other which not only exchange energy but also particles. Many experimental setups conform with this situation where a small volume, film, or interface is in contact with a huge particle reservoir. The particle number fluctuates around a mean value such that the equilibrium condition is fulfilled, i. e., the chemical potentials of both subsystems are equal.

Here, we assume separability of the kinetic and the potential energy term in the Hamiltonian. Then, the probability distribution to find N particles in a configuration $\{\mathbf{r}^N\}$ is

$$f(\mathbf{r}^N, N) = \frac{1}{\Lambda^{3N} N! \Xi} \exp(\beta\mu N) \exp(-\beta E_{pot}(\mathbf{r}^N, N)). \quad (96)$$

with the grand partition function

$$\Xi = \sum_{N=0}^{\infty} \frac{\exp(\beta\mu N)}{\Lambda^{3N} N!} V^N \int \exp(-\beta E_{pot}(\mathbf{r}^N, N)) d\mathbf{r}^{3N} \quad (97)$$

which contains the configurational integral as eq. (88) but also *integrates* over N with the weight $\exp(\beta\mu N)$. The quantity $\exp(\beta\mu)/\Lambda^3$ is defined as the activity. Similar to eq. (91) the grand potential Ω links statistical mechanics and thermodynamics via the relation

$$\Omega = -k_B T \ln \Xi. \quad (98)$$

The thermodynamic functions S , P , and N are determined by the derivatives of Ω with respect to the independent variables μ , V , and T . The important (fixed) parameter μ is given within the canonical ensemble as a derivative of $\ln Q_N$ and therefore as an ensemble average (see eq. (95)). In practice, it can be computed via the Widom method presented in sec. 4.6.

One central issue of the grand canonical ensemble is the fluctuating quantity N which yields another important property of the system, i. e. the isothermal compressibility. The latter is defined as

$$\chi_T = -\frac{1}{V} \left(\frac{\partial V}{\partial P} \right)_T. \quad (99)$$

The ensemble average of the particle number reads

$$\langle N \rangle = \sum_{N=0}^{\infty} N P(N) \quad (100)$$

with the probability $P(N) = \int f(\mathbf{r}^N, N) d\mathbf{r}^N$ of finding a state in the ensemble μVT possessing exactly N particles. The mean-square deviation $\langle(\Delta N)^2\rangle = \langle N^2\rangle - \langle N\rangle^2$ is a measure for the fluctuations of N . Using eqs. (100), (96), and (99) it follows [52]

$$\frac{\langle(\Delta N)^2\rangle}{\langle N\rangle} = \frac{k_B T}{\langle N\rangle} \frac{\partial \langle N\rangle}{\partial \mu} = \rho k_B T \chi_T \quad (101)$$

which is the relative mean-square deviation. A direct conclusion from eq. (101) is that χ_T is always positive or zero since $\langle N^2\rangle \geq \langle N\rangle^2$.

3.3 Isobaric-isothermal ensemble

The isobaric-isothermal ensemble is a set of all possible states characterized by a constant particle number N , pressure P , and temperature T [52]. In contrast to the canonical ensemble in sec. 3.1 the volume V can fluctuate. Thus, the density is not fixed. In contrast to the grand canonical ensemble, it has the advantage that the pressure is fixed. This is interesting for experiments since the pressure can be controlled easily. The corresponding thermodynamic quantity is the Gibb's free energy

$$G = F + PV. \quad (102)$$

The thermodynamic functions S , V , and μ are given by derivatives of G with respect to the corresponding independent variables [52]. The link between thermodynamics and statistical mechanics is given by

$$G = -k_B T \ln \Delta_N. \quad (103)$$

The partition function Δ_N involves the canonical partition function Q_N of eq. (86) but further it is averaged over the volume V weighted with the Boltzmann factor $\exp(-\beta PV)$ and reads

$$\Delta_N = \beta P \int_0^\infty \exp(-\beta PV) Q_N dV. \quad (104)$$

3.4 Structural observables

An important measure of the microscopic structure of colloidal suspensions in bulk is the radial distribution function (or pair correlation function)

$$\begin{aligned} g(r) &= \frac{\left\langle \sum_k \sum_{l \neq k} \delta(|\mathbf{r}_k - \mathbf{r}_l|) \right\rangle}{N\rho 4\pi r^2 \Delta r} \\ &= \frac{\langle N(r, \Delta r) \rangle}{N\rho 4\pi r^2 \Delta r}. \end{aligned} \quad (105)$$

with the number $N(r, \Delta r)$ of particles within a spherical shell of radius r and thickness Δr . The particle number density ρ given as

$$\rho = \frac{N}{V} \quad (106)$$

is related to the volume fraction

$$\phi = \frac{\pi}{6} \rho \sigma^3 \quad (107)$$

with the particle diameter σ . The radial distribution function provides information about the probability of finding a certain distance between the particles and allows conclusions about the structure. In particular, it allows the distinction between gas-, fluid-, and solid-like states. Furthermore, it reveals information about characteristic length scales in the asymptotic regime ($r \rightarrow \infty$). The latter is discussed in sec. 3.5.

Confining surfaces have a deep impact on the structure formation of these systems. It is reasonable to calculate several observables describing the structure of the colloids which take into account the symmetry breaking due to the surfaces. One fundamental impact of the confinement on the suspension is the layering of particles. Monitoring this layering (see sec. 5.1) is easily done by computing the local density

$$\rho(z) = \langle N(z)/V \rangle \quad (108)$$

with the number of particles $N(z)$ located within a thin layer from z to $z + \Delta z$ parallel to the walls.

Similar to the pair correlation functions eq. (105) for the bulk system, the in-plane structure of the layers is monitored via in-plane radial distribution functions (in-plane pair correlation functions)

$$g_{||}(r_{||}) = \frac{\langle N^{layer}(r_{||}, \Delta r) \rangle}{N^{layer} \rho^{layer} 2\pi r_{||} \Delta r} \quad (109)$$

with the number of particles N^{layer} within a particle layer parallel to the surfaces between $z = r_{||}$ and $z = r_{||} + \Delta r$ and the mean particle area density in this layer. A layer is defined by two neighboring minima of the local density defined in eq. (108). Note, that in the definition eq. (109) the z -positions within a layer are projected on a (2D) plane. Hence, eq. (109) deviates from the definition in [7]. These in-plane correlation functions are computed for each particle layer between the confining surfaces separately since they are not expected to be identical. Due to the exponential dampening of the density profile for increasing distance from the wall the layers become less pronounced and their mean density might change as well. This has impact on the in-plane structure.

At higher densities the particle layers show an onset of freezing. These structural changes within the layers are monitored via local bond angle order parameters ψ_n which are a measure for the degree of in-plane ordering. The subscript n stands for the n -fold symmetry of interest. This order parameter for a certain layer is defined as

$$\psi_n = \left\langle \frac{1}{N_{layer}} \sum_{i=1}^{N_{layer}} \frac{1}{N_i^b} \left| \sum_{j=1}^{N_i^b} \exp(in\theta_j) \right| \right\rangle \quad (110)$$

with the number of neighboring particles N_i^b of the particle i , and the bond angle θ_j enclosing an arbitrary in-plane axis and the bond vector \mathbf{r}_{ij} between particles i and j . In this work we focus on the parameters ψ_4 (or ψ_8) and ψ_6 which are sensitive on squared and hexagonal structures, respectively. For a perfect square lattice $\psi_4 = \psi_8 = 1$ and $\psi_6 = 0$ whereas for a perfect hexagonal lattice $\psi_6 = 1$ and $\psi_4 = \psi_8 = 0$. A detailed calculation of the local bond order parameters and the determination of next neighbors is given in appendix A.

In order to investigate freezing phase transitions (see sec. 3.6) it is useful to compute corresponding bond order fluctuations

$$\chi_n = N (\langle \psi_n^2 \rangle - \langle \psi_n \rangle^2) \quad (111)$$

which are a measure of how strong the bond order parameters fluctuate. In the vicinity of a phase transition, the fluctuations are expected to increase significantly which is discussed briefly in sec. 3.6.

An important thermodynamic observable is the normal pressure which is related to the solvation force known from AFM experiments. This quantity is related to the layering of the particles parallel to the surfaces mentioned above and, therefore, exhibits an oscillating behavior (at least for small densities) as function of the surface separation L_z . An analytical description of this

behavior, which is related to the pair correlation functions, is given in sec. 3.5. A virial expression of the normal component of the pressure tensor \mathbf{P} can be derived from the total energy of the system which reads [110]

$$P_{zz} = k_B T \left\langle \frac{N}{L_z A} \right\rangle - \left\langle \frac{1}{A} \frac{\partial U^{total}}{\partial L_z} \right\rangle \quad (112)$$

with particle number N , surface area A , and the total energy $U^{total} = U^{FF} + U^{FS}$ containing both the fluid-fluid and the fluid-solid interactions. The first term in eq. (112) is the ideal contribution to the pressure. The other energy contributions are given as

$$U_{FF} = \frac{1}{2} \sum_{i=1}^N \sum_{j \neq i}^N u_{FF}(r_{ij}) \quad \text{and} \quad (113)$$

$$U_{FS} = \sum_{k=1}^2 \sum_{i=1}^N u_{FS}^{[k]}(z_i \mp L_z/2) \quad (114)$$

with the energy $u_{FF}(r_{ij})$ of particle i in the potential of particle j , and the energy $u_{FS}^{[k]}(z_i \mp L_z/2)$ of particle i in the potential of wall k . Hence, the derivatives in eq. (112) can be calculated. Using a reduced z -component $z_i = L_z z_i^*$, the absolute value $r_{ij} = |\mathbf{r}_{ij}|$ is re-expressed as

$$r_{ij} = \sqrt{(x_i - x_j)^2 + (y_i - y_j)^2 + L_z^2(z_i^* - z_j^*)^2} \quad (115)$$

which yields by insertion of eq. (113)

$$\begin{aligned} \frac{\partial U_{FF}}{\partial L_z} &= \frac{1}{2} \sum_{i=1}^N \sum_{j \neq i}^N \frac{\partial u_{FF}(r_{ij})}{\partial r_{ij}} \frac{L_z(z_i^* - z_j^*)^2}{r_{ij}} \\ &= \frac{1}{2L_z} \sum_{i=1}^N \sum_{j \neq i}^N \frac{\partial u_{FF}(r_{ij})}{\partial r_{ij}} \frac{z_{ij}^2}{r_{ij}} \end{aligned} \quad (116)$$

with $z_{ij} = \mathbf{r}_{ij} \cdot \mathbf{e}_z$. Inserting eq. (114) yields

$$\frac{\partial U_{FS}}{\partial L_z} = \frac{1}{L_z} \sum_{k=1}^2 \sum_{i=1}^N \left(z_i \mp \frac{L_z}{2} \right) \frac{\partial u_{FS}(z_i^{[k]})}{\partial z_i^{[k]}}. \quad (117)$$

The lateral components P_{xx} and P_{yy} are defined analogously to eq. (112) containing the derivative with respect to x or y , respectively. The structuring in the pore influences these components as well. For $L_z \rightarrow \infty$, i. e. in the

limit case of a homogeneous system, the diagonal elements of the pressure tensor equal each other ($P_{xx} = P_{yy} = P_{zz}$). Besides the virial expression of the normal pressure eq. (112), a “force” expression can be defined reading [110]

$$P_{zz}^{force} = -\frac{\langle F_z^{[1]} \rangle - \langle F_z^{[2]} \rangle}{2A} \quad (118)$$

with the force $F_z^{[k]}$ of the particles acting the wall k . In principle, both expressions are identical, i. e. $P_{zz} = P_{zz}^{force}$. Therefore, comparing both values within computer simulations can be used as a consistency check.

3.5 Asymptotics via Ornstein-Zernike equation

Solvation forces extracted from AFM experiments [98, 116] exhibit for large surface separations exponentially decaying oscillations of the amplitude. They are determined by one (leading) wave- and decay length which is, in general, not the case for short separations. Using the same suspension, the same quantitative asymptotic behavior is found in the bulk correlation functions extracted from SANS experiments [74]. More precisely, the wavelengths and decay lengths equal each other. This is remarkable since the oscillations of the solvation forces are a result of the particle layering, i. e., they are induced by the confining surfaces. However, the wavelength seems to be an intrinsic property of the suspension which is not affected by the confinement itself. In a theoretical way this was predicted by DFT calculations [34, 41, 105, 48]. Thus, it is worthwhile to take a closer look on the theoretical description of the correlation functions, density profiles, and solvation pressure curves via OZ theory.

The asymptotic behavior of the correlation functions of a bulk system can be analytically described via the exact Ornstein-Zernike (OZ) equation [93, 52]. In such a homogeneous system with constant density ρ , the OZ equation reads

$$h(r) = c(r) + \rho \int d\mathbf{r}' h(|\mathbf{r} - \mathbf{r}'|) c(r') \quad (119)$$

with the total correlation function $h(r)$ and the direct correlation function $c(r)$. This convolution can be transformed via Fourier transformation into

$$\hat{h}(q) = \frac{\hat{c}(q)}{1 - \rho\hat{c}(q)}. \quad (120)$$

The back transformation using spherical coordinates yields

$$rh(r) = \frac{1}{4\pi^2 i} \oint_C dq q \exp(iqr) \frac{\hat{c}(q)}{1 - \rho\hat{c}(q)}, \quad (121)$$

where the q -integration is extended to the complex plane via a closed (infinite) contour including the q -axis. Note, that the integrand of eq. (121) is supposed to vanish at infinity to ensure the convergence of the integral and to get only contributions from the q -axis. Obviously, the contour integral in eq. (121) is determined by the poles of the integrand, i. e., the n complex roots $q_n = \alpha_1 + i\alpha_0$ of $1 - \rho\hat{c}(q)$. Then, it is easily solved using the residue theorem where one encounters the special case with an integrand $f(q) = G(q)/H(q)$ with functions $G(q_n) \neq 0$ and $H(q_n) = 0$ at the simple pole q_n . The residue in this case is defined as $\text{Res}[f(q); q_n] = G(q_n)/H'(q_n)$ containing the derivative of H with respect to q . For eq. (121) one gets [48]

$$\begin{aligned} rh(r) &= \frac{1}{4\pi^2 i} 2\pi i \sum_n \text{Res} \left[\frac{G(q)}{H(q)}; q_n \right] \\ &= \frac{1}{2\pi} \sum_n \frac{\exp(iq_n r) q_n \hat{c}(q_n)}{\rho(\partial\hat{c}(q)/\partial q)|_{q=q_n}} \\ &= \sum_n A_n \exp(iq_n r) \end{aligned} \quad (122)$$

with complex coefficients A_n . From this result one can see that the poles $q_n = \alpha_1 + i\alpha_0$ with the smallest imaginary part yield a contribution to the exponential function with the smallest decay, i. e., it is the leading pole determining the asymptotic behavior of $h(r)$. Other poles with larger imaginary parts contribute to $h(r)$ at smaller r . Since we focus on the asymptotic range only the leading pole is taken into account. If the leading pole is purely imaginary the total correlation function shows a non-oscillating, exponential decay for large r , i. e., $rh(r) \approx A \exp(-\alpha_0 r)$. If $\alpha_1 + i\alpha_0$ is a root of the denominator in eq. (121) then $-\alpha_1 + i\alpha_0$ is a solution as well yielding

$$rh(r) \approx \exp(-\alpha_0 r) (A^+ \exp(i\alpha_1 r) + A^- \exp(-i\alpha_1 r)) \quad (123)$$

where the complex coefficients A^+ and A^- can be rewritten as $|\tilde{A}| = |A^+| = |A^-| = A^\pm \exp(\pm i\Theta^\pm)$ by introducing the phase $\Theta = \Theta^+ = -\Theta^-$. Hence, one gets

$$\begin{aligned} rh(r) &\approx \exp(-\alpha_0 r) \left(|\tilde{A}| \exp(i(\alpha_1 r - \Theta)) + |\tilde{A}| \exp(-i(\alpha_1 r - \Theta)) \right) \\ &\approx 2|\tilde{A}| \exp(-\alpha_0 r) \cos(\alpha_1 r - \Theta) \quad \text{for } r \rightarrow \infty. \end{aligned} \quad (124)$$

The physical interpretation of the coefficients α_0 and α_1 yields the decay length ξ_b and the wavelength λ_b of the total correlation function $h(r)$ reading $\alpha_0 = \xi_b^{-1}$ and $\alpha_1 = 2\pi/\lambda_b$. In a ρ - T phase diagram the region with purely imaginary poles and the region with non-purely imaginary poles is

separated by the Fisher-Widom line [36]. It divides the phase diagram into exponentially damped solutions which are oscillatory or non-oscillatory [34].

The local density profiles and the solvation pressure both introduced in sec. 3.4 exhibit an oscillatory behavior as well. Thus, the question arises whether there is a relation to the bulk correlations described above. The pressure oscillations are a direct consequence of the particle layering near a wall, i. e., the oscillating particle density. One might conclude that this effect induced by confinement might possess different properties than the correlations in bulk. In general, this is valid for small distances from the confining surface [105]. However, in the asymptotic range ($L_z \rightarrow \infty$) the direct influence of the walls (assuming short-range potentials) on the confined film becomes small. The layers far from the walls (i. e., in the center of the slit pore) are due to the particle correlations of the surrounding layers. In deed, from OZ theory it is possible to derive the same form of exponential decay for the local density $\rho(z)$ [55, 34, 105, 48]. To this end, a system of many small particles S and one particle B much bigger than the small ones is considered. This is the limit case of a mixture with $\rho_B \rightarrow 0$ and $\sigma_B \rightarrow \infty$. Applying this to the considerations above for the bulk correlation function yields

$$\rho(z) - \rho_b = A_f \exp\left(-\frac{z}{\xi_f}\right) \cos\left(\frac{2\pi}{\lambda_f}z - \Theta_f\right) \quad \text{for } z \rightarrow \infty. \quad (125)$$

with the amplitude A_f , the decay length ξ_f , the wavelength λ_f , and the phase Θ_f . DFT revealed that in the asymptotic range the characteristic lengths λ_f and ξ_f of the $\rho(z)$ given in eq. (125) equal λ_b and ξ_b of the bulk correlation function given in eq. (124) at same chemical potential [55, 34, 48]. On the other hand, A_f and Θ_f deviate from the values of the bulk correlations since they depend on the nature of the fluid-wall potential. It was shown by DFT as well that the solvation force, and thus the solvation pressure $P_{zz}(L_z)$, possesses the same features as $\rho(z)$ [41, 105, 75, 72]. Hence, in the asymptotic limit the normal pressure behaves as

$$P_{zz} - P_{bulk} = A_f \exp\left(-\frac{L_z}{\xi_f}\right) \cos\left(\frac{2\pi}{\lambda_f}L_z - \Theta_f\right) \quad \text{for } L_z \rightarrow \infty. \quad (126)$$

The experimentally measured force-distance curves are fitted according to

$$\frac{F(L_z)}{2\pi R} = A \exp\left(-\frac{L_z}{\xi}\right) \cos\left(\frac{2\pi}{\lambda}L_z - \Theta\right) + offset \quad \text{for } L_z \rightarrow \infty. \quad (127)$$

with R being the radius of the colloidal probe of the CP-AFM. The asymptotic expressions eqs. (125) and (126) are valid for interaction potentials

which are finite-ranged or exponentially decaying [34, 105]. Furthermore, the expressions discussed here are valid for systems without long-range order, i. e., frozen systems deviate dramatically from exponential decay. Freezing involves deviations from oscillatory behavior in $\rho(z)$ and P_{zz} since even for large r , z , or L_z more than one leading wave- and decay length can exist.

3.6 Phase transitions

In chapter 6 we focus on freezing of the charged suspensions. The challenge is how to determine and characterize such transitions. Thus, it is reasonable to consider the thermodynamic background and how the free energy and fluctuation quantities can give evidence for phase transitions.

In practice, it is difficult to calculate the free energy since it is not given as an average of functions which only depend on phase space coordinates during the simulation [52]. All quantities directly related to the partition function, as e. g. the free energy, rather depend on the available volume in phase space which is accessible to the system. These are called thermal quantities. There are different methods to determine free energies as, e. g., thermodynamic integration. For more details on this issue see [39]. In simulations but also in experiments it is easy to determine derivatives of the free energy F as, e. g., the pressure or the internal energy (see sec. 3.1).

However, there is a special case where the free energy can be measured directly via the pressure. This is possible if the system is homogeneous in the volume V (bulk system), or if a confined system is homogeneous in the area A where A is parallel to the plane surface(s) [110]. Here we consider the grand canonical ensemble with the grand potential Ω and

$$d\Omega = -SdT - Nd\mu + \tau_{||}s_{z0}dA + \tau_{\perp}A_0ds_z \quad (128)$$

with the stress tensor τ and the wall separation s_z (see sec. 3.2). Due to the symmetry breaking in z -direction by the confining walls the system is assumed to be homogeneous in x - and y -direction. Then, the homogeneity condition requires

$$\Omega(T, \mu, \lambda A, s_z) = \lambda \Omega(T, \mu, A, s_z) \quad (129)$$

with $\lambda \in \mathbb{R}$. Euler's theorem [110] states that a homogeneous function can be rewritten using derivatives of the function and coordinates which one gets by differentiation of eq. (129) with respect to λ yielding

$$A \frac{\partial \Omega(T, \mu, \lambda A, s_z)}{\partial(\lambda A)} = \Omega(T, \mu, A, s_z). \quad (130)$$

On the other hand substituting A by λA in eq. (128) and assuming T , μ and s_z to be constant yields

$$\frac{\partial \Omega(T, \mu, \lambda A, s_{z0})}{\partial(\lambda A)} d(\lambda A) = \tau_{||} s_{z0} d(\lambda A). \quad (131)$$

Finally, inserting eq. (130) into eq. (131) one gets a simple relation for the grand-potential energy density

$$\omega(T, \mu, A, s_{z0}) = \frac{\Omega(T, \mu, A, s_{z0})}{s_{z0} A} = \tau_{||}. \quad (132)$$

Under the condition of homogeneity with respect to A , the free energy density ω is useful to investigate phase transitions [110]. For two phases i and j at coexistence, a first-order phase transition (discontinuous transition) satisfies the conditions

$$\omega_i(\mu_{co}, T) = \omega_j(\mu_{co}, T) \quad (133)$$

$$\left(\frac{\partial \omega_i}{\partial \mu} \right)_T \Big|_{\mu=\mu_{co}} \neq \left(\frac{\partial \omega_j}{\partial \mu} \right)_T \Big|_{\mu=\mu_{co}} \quad (134)$$

with the chemical potential at coexistence μ_{co} . The intersection in eq. (133) states that both phases possess the same free energy at coexistence. In case of a second-order transition (continuous transition), the terms in eq. (134) would equal each other. From eq. (128) and eq. (132) it follows

$$\left(\frac{\partial \omega}{\partial \mu} \right)_{T, A, s_{z0}} = -\rho < 0 \quad (135)$$

with the density ρ of the system, i. e., the free energy density is a monotonic function in μ . Further calculation using Gibbs-Duhem equation shows that $\omega(\mu)$ is concave and the curvature depends on the compressibility [110].

As introduced in sec. 3.4, the bond order susceptibilities χ_n given in eq. (111) are a further method to get evidence for phase transitions. In the vicinity of the coexistence point, χ_n is supposed to increase significantly and reaches a maximum at coexistence. There, a transition into a crystal-like phase with order n occurs. In the thermodynamic limit ($N \rightarrow \infty$), a first-order transition is characterized by large but finite fluctuations whereas a second-order transition exhibits diverging fluctuations [16]. Since an infinitely large system is not realizable in computer simulations, it is possible to compute χ_n around the expected phase transition for several N . Whereas the maximum of χ_n in case of a first-order transition should not change in height, it diverges with increasing N for a second-order transition.

3.7 Ensembles for binary mixtures

An ensemble for binary mixtures differs from the ensembles for monodisperse systems in the number of fixed (independent) variables. The canonical ensemble for a mixture, introduced in sec. 3.1 for monodisperse systems, is characterized by two constant particle numbers N_A and N_B for particle species A and B , volume V , and temperature T . The total particle number is $N = N_A + N_B$. For separable kinetic and the potential energy in the Hamiltonian, the probability density reads

$$f^{[N_A, N_B]}(\mathbf{r}_A^{N_A}, \mathbf{r}_B^{N_B}) = \frac{1}{\Lambda_A^{3N_A} \Lambda_B^{3N_B} N_A! N_B!} \frac{\exp(-\beta E_{pot}(\mathbf{r}_A^{N_A}, \mathbf{r}_B^{N_B}))}{Q_{N_A, N_B}} \quad (136)$$

with particles A at positions $\{r_A\}$ and particles B at $\{r_B\}$. The interaction potential is $E_{pot}(\mathbf{r}_A^{N_A}, \mathbf{r}_B^{N_B}) = E_{pot}^{AA}(\mathbf{r}_A^{N_A}) + E_{pot}^{AB}(\mathbf{r}_A^{N_A}, \mathbf{r}_B^{N_B}) + E_{pot}^{BB}(\mathbf{r}_B^{N_B})$ and the thermal wavelengths depending on material properties read $\Lambda_i = (h^2/(2\pi k_B T m_i))^{1/2}$. The corresponding canonical partition function is given by

$$Q_{N_A, N_B} = \frac{1}{\Lambda_A^{3N_A} \Lambda_B^{3N_B} N_A! N_B!} \int \int \exp(-\beta E_{pot}(\mathbf{r}_A^{N_A}, \mathbf{r}_B^{N_B})) dr_A^{3N_A} dr_B^{3N_B}. \quad (137)$$

The grand canonical ensemble for a mixture, introduced in sec. 3.2 for monodisperse systems, is characterized by fixed chemical potentials for each particle species μ_A and μ_B , volume V , and temperature T . This yields a density probability of

$$f(\mathbf{r}_A^{N_A}, \mathbf{r}_B^{N_B}, N_A, N_B) = \frac{\xi_A^{N_A} \xi_B^{N_B}}{N_A! N_B!} \frac{\exp(-\beta E_{pot}(\mathbf{r}_A^{N_A}, \mathbf{r}_B^{N_B}))}{\Xi^{(mix)}} \quad (138)$$

with the activities $\xi_i = \exp(\beta \mu_i)/\Lambda_i^3$ and the grand partition function

$$\Xi^{(mix)} = \sum_{N_A=0}^{\infty} \sum_{N_B=0}^{\infty} \frac{\xi_A^{N_A} \xi_B^{N_B}}{N_A! N_B!} \int \int \exp(-\beta E_{pot}(\mathbf{r}_A^{N_A}, \mathbf{r}_B^{N_B})) dr_A^{3N_A} dr_B^{3N_B}. \quad (139)$$

3.8 Structural observables for binary mixtures

In binary mixtures one has to distinguish more structural observables since the different species are expected to behave differently. Therefore, it is reasonable to consider certain properties of the whole system (see sec. 3.4) as well as for a certain species. The suspension is determined by a particle number density for a certain species i given as

$$\rho_i = \frac{N_i}{V} \quad (140)$$

which is related to the volume fraction

$$\eta_i = \frac{\pi}{6} \rho_i \sigma_i^3 \quad (141)$$

with the particle diameter σ_i of species i . The most interesting quantities are the pair correlation functions in bulk and confinement and the local density profiles in confinement. Coming from eq. (108) the latter is easily defined for species i as

$$\rho_i(z) = \langle N_i(z)/V \rangle \quad (142)$$

with the particle number N_i of species i within a thin layer from z to $z + \Delta z$. The pair correlation functions (see sec. 3.4) also contain cross terms and read for two species i and j

$$\begin{aligned} g_{ij}(r) &= \frac{\left\langle \sum_k \sum_{l \neq k} \delta(|\mathbf{r}_k^{(i)} - \mathbf{r}_l^{(j)}|) \right\rangle}{N_i N_j 4\pi r^2 \Delta r / V} \\ &= \frac{\langle N_i(r^{(j)}, \Delta r) \rangle}{N_i N_j 4\pi r^2 \Delta r / V} \end{aligned} \quad (143)$$

with the particle number N_i of species i in the system and volume V . The function $N_i(r^{(j)}, \Delta r)$ gives the particle number of species i found in a thin shell with radius $r^{(j)}$ and thickness Δr around a particle of species j . The denominator ensures normalization of $g(r)$. Similarly, the in-plane pair correlation function for a two-component mixture reads

$$g_{||,ij}(r_{||}) = \frac{\left\langle N_i^{layer}(r_{||}^{(j)}, \Delta r) \right\rangle}{N_i^{layer} N_j^{layer} 2\pi r_{||} \Delta r / A} \quad (144)$$

with the particle number N_i^{layer} of species i in a certain layer of the confined system and volume V . The function $N_i^{layer}(r_{||}^{(j)}, \Delta r)$ has the analogous meaning as in eq. (143) with respect to the layer considered.

3.9 Asymptotic behavior in binary mixtures

Corresponding to OZ theory in sec. 3.5 the asymptotic behavior of the correlation functions is in general determined by the leading order pole and has the form

$$rh_{ij}(r) \propto A_{ij} \exp(-\alpha_0 r) \cos(\alpha_1 r - \Theta_{ij}) \quad \text{for } r \rightarrow \infty \quad (145)$$

with i, j being the particle species (see table 5). The bulk wavelength λ_b and correlation length ξ_b are given by $\alpha_0 = \xi_b^{-1}$ and $\alpha_1 = 2\pi/\lambda_b$. Note, that the poles α_0 and α_1 are the same for all pairs (i, j) whereas the amplitude A_{ij} and the phase Θ_{ij} are not. However, due to the fitting procedure of the numerical results the fit parameters yield wave- and decay lengths which are not exactly equal. Hence, in the following the results of all λ_{ij} and ξ_{ij} are presented.

Reduced variables $\lambda_b^* = \lambda_b/\sigma$ ($\lambda_{ij}^* = \lambda_{ij}/\sigma$) and $\xi_b^* = \xi_b/\sigma$ ($\xi_{ij}^* = \xi_{ij}/\sigma$) are used.

4 Simulation Methods

4.1 Reduced units

In order to employ computer simulations it is reasonable to introduce reduced variables. On one hand dimensionless quantities are considered, and on the other hand their values are around order 1 reducing numerical errors. Energy-related quantities are scaled by a characteristic energy in the system which is the thermal energy of particles $k_{\text{B}}T$. Lengths are scaled by the characteristic length σ , i. e. the particle diameter. The simulations are done in an imaginary box of lengths L_x , L_y , and L_z . Additionally, the particle positions within the simulation box are scaled by these lengths yielding a unit box which is useful to treat minimum image convention and periodic boundaries easily (see sec. 4.2).

The next sections use reduced particle positions $\tilde{\mathbf{r}}$ in the unit simulation box defined as

$$\tilde{\mathbf{r}}^T = (r_x/L_x, r_y/L_y, r_z/L_z). \quad (146)$$

Hence, the probability density eq. (96) can be rewritten as $\tilde{f}(\tilde{\mathbf{r}}^N, N) = V^N f(\mathbf{r}^N, N)$ yielding the transition probability eq. (160) in sec. 4.4.

The reduced variables are $\mathbf{r}^* = \mathbf{r}/\sigma$, $L_i^* = L_i/\sigma$, $\kappa^* = \kappa\sigma$, $E_{\text{pot}}^* = E_{\text{pot}}/(k_{\text{B}}T)$, $\mu^* = \mu/(k_{\text{B}}T)$, and $P^* = P\sigma^3/(k_{\text{B}}T)$.

4.2 Periodic boundaries and minimum image convention

Simulations of many-particle systems are used to determine macroscopic properties from a microscopic description of the particle interactions. To this end, the particles are localized in a simulation cell of finite size. However, a macroscopic level is reached if two conditions are fulfilled. First, it is reached on a length scale where correlations between two spatial points vanish, which is in general much bigger than the microscopic structure of the system. Second, if boundary effects of the particles at the boundaries of the cell are negligible. The latter might increase for decreasing system size since the fraction of particles at the boundaries of the cell is proportional to $N^{-1/3}$. Theoretically, a macroscopic system is given by the thermodynamic limit with particle number $N \rightarrow \infty$ and volume $V \rightarrow \infty$ while the mean density is fixed. Thus, depending on the specific interactions, an appropriate simulation cell might include billions of particles. Computer systems nowadays can handle hundreds to millions of particles. Hence, it might be necessary to limit the system to much smaller sizes.

Due to these limitations the boundaries of the simulation cell has to be chosen such that the system still represents the bulk behavior. Thus, the surrounding volume of the cell is taken into account which must possess the same properties as the simulation cell itself. An appropriate choice are periodic boundaries where an infinite number of copies of the original cell is put together [39]. It mimics bulk behavior since on a macroscopic scale no point, disregarding the boundaries, is distinguished. However, one must be aware of long-range correlations which might be changed by boundary effects. The total interaction energy of one particle interacting with all other particles (including the periodic images) reads

$$U = \frac{1}{2} \sum'_{i,j,\mathbf{n}} u(|\mathbf{r}_{ij} + \mathbf{n}L|) \quad (147)$$

with the interaction potential u , size L of the simulation box, and vector \mathbf{n} consisting of integers pointing to images of the box. The prime indicates that the case $i = j$ for $\mathbf{n} = 0$ is neglected, since it would be the interaction of a particle with itself. The prefactor $1/2$ is due to double-counted pairs ij and ji . In practice, it is not possible to determine eq. (147) due to the infinite number of particles. However, many systems are characterized by short-range potentials, e. g., LJ or Yukawa systems. In this case, the potential can be truncated at a certain r_c . The error resulting from the truncation of the tail beyond r_c can be estimated by integration of $u(r)$ from r_c to ∞ [39]. The potential must decrease stronger than r^{-d} with d being the spatial dimension. Otherwise, integration over the tail becomes infinity and cannot be neglected.

If the potential is short-ranged, then an appropriate cut-off radius r_c can be found. A quite common method is to set the length of the sides of the simulation cell to $2r_c$, i. e. the potential can be truncated within the size of the cell. There, the minimum image convention (MIC) is used where only the closest image of a particle contributes to the interaction energy of the particle considered. The advantage is that only the simulation cell and 26 neighboring images of it (in three dimensions) must be taken into account. Note, that in the MIC the potential is truncated at different distances r depending on the orientation of the bond vector connecting the two particles. Thus, a simple truncation might yield further errors.

A cut-off in systems decaying equally or slower than r^{-d} yields large errors since the potential tail beyond r_c is non-negligible. A typical example is the dipolar interaction potential. The tail must be taken into account by using summation methods which correct the error. A widely used summation method is the Ewald summation [110]. In this thesis the LJ and the screened

DLVO potential can be truncated. A more detailed discussion about the truncation of potentials is presented in sec. 4.3.

4.3 Truncated and shifted potential

In general, in an ensemble all particles can interact with each other depending on the interaction range of the potential. For computer simulations it is time-consuming to compute all pair interactions. However, if the potential is short-ranged, i. e. it drops down to small values at small distances r , it is possible to cut-off the potential. In order not to become discontinuous, it is reasonable to *shift* the potential which keeps it continuous and differentiable at the cut-off radius r_c . To this end, the ansatz $\tilde{u}(r) = u(r) + a + br$ with the assumptions $\tilde{u}(r_c) = 0$ and $\tilde{u}'(r_c) = 0$ with the prime being the derivative with respect to r is used. Solving this system of equations yields

$$\tilde{u}(r) = u(r) - u(r_c) - u'(r_c)(r - r_c) \quad (148)$$

$$\tilde{u}'(r) = u'(r) - u'(r_c). \quad (149)$$

Applying eqs. (148) and (149) to the potentials used in this thesis, i. e. DLVO with soft core, one has to care about the accuracy of the truncation. The cut-off radius must be large enough to ensure that the deviation from the non-truncated potential is negligible. In particular, for the DLVO interaction where the interaction range might be in the order of the size of the simulation box, it is reasonable to define a criterion how large r_c should be. Thus, a minimum for the shortest side $L = \min(L_x, L_y, L_z)$ of the simulation box is given as well where $L/2 = r_c$ due to the MIC (see sec. 4.2). Here, we use the criterion [85]

$$\frac{u(r_c)}{u(\sigma)} < \delta \quad (150)$$

which says that the potential at the cut-off radius compared to the potential at contact of the particles (distance σ) should be smaller than the relative accuracy δ . Reasonable values are $10^{-4} > \delta > 10^{-6}$ [85]. Here, we choose $\delta = 10^{-4} - 10^{-5}$. First, we consider the soft core potential given in eq. (51). Inserting the potential into eq. (150) yields

$$r_{c,LJ}^* > \delta^{-\frac{1}{12}} \quad (151)$$

where reduced units, introduced in sec. 4.1, are used. With $\delta = 10^{-5}$ it follows $r_{c,LJ}^* > 2.61$. For the simulations presented in the following chapters we chose $r_{c,LJ}^* = 2.5$. For the parameter ranges investigated in this work the DLVO interaction ranges are more or less in the order of the simulation

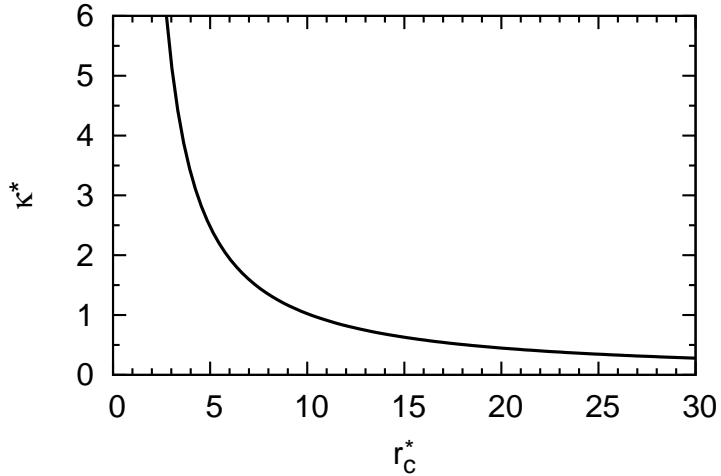


Figure 6: The minimal reduced screening parameter κ^* for a given cut-off radius r_c^* . The region above the curve is the “valid” region where truncation is allowed, i. e. κ^* (or r_c^*) is large enough to yield accurate results for simulations using the truncated potential.

boxes. Thus, the criterion eq. (150) gives an estimation of the minimal size of the simulation cell. Applying the DLVO potential given in eq. (47) to eq. (150) yields

$$\frac{\sigma \exp(-\kappa r_c)}{r_c \exp(-\kappa \sigma)} < \delta. \quad (152)$$

Rearranging eq. (152) gives a condition for the screening parameter κ which reads

$$\kappa^*(r_c^*) > -\frac{\ln(\delta r_c^*)}{r_c^* - 1} \quad (153)$$

using reduced units from sec. 4.1. In fig. 6 the function $\kappa^*(r_c^*)$ in case of equality in eq. (153) is plotted. The region above the curve is the “valid” range where the cut-off radius yields, to a given κ , an accurate truncated potential. In other words, the differences of the truncated potential from the non-truncated one are small enough to give simulation results with negligible deviations. For instance, a value of κ equal to 1.0 requires a minimal cut-off radius of $r_c^* \gtrsim 10$. Hence, the minimal spatial periodicity of the simulation cell is $L \approx 20$ due to MIC as mentioned above. Note, that the curve in fig. 6 also depends on the macroion charge Z , the salt concentration I , and the macroion density ρ since κ depends on them (see sec. 2.2).

4.4 Monte-Carlo method

A system in the canonical ensemble with constant N , V and T described in sec. 3.1 can be sampled via MC. Therefore a sequence of particle configurations is generated by random particle displacements sampling the phase space which corresponds to solving the integral in the partition function Z . Depending on the physics of the considered system, i. e., the interaction potential of the particles, some configurations have a larger probability than others. With the probability density of sec. 3.1 a transition probability can be derived which is used to decide whether a new configuration, i. e., a new state, is accepted or rejected. The ensemble average of physical quantities of interest as, e. g., the potential energy can then be evaluated as an unweighted average over the set of configurations. Since in this method no time involved only static properties can be investigated.

We briefly sketch the derivation of this method using the theory of Markov processes [52, 39] in which the probability $q_n(t)$ of finding a new state n at time t in a sequence of states only depends on the previous state at time t . Note, that there is no physical meaning of time in this method. Such a sequence is a Markov chain which can be written as

$$q_n(t) = \sum_m p_{nm} q_m(t-1) \quad (154)$$

or

$$\mathbf{q}(t) = \mathbf{p} \cdot \mathbf{q}(t-1) = \mathbf{p}^t \cdot \mathbf{q}(0) \quad (155)$$

with the probability vector $\mathbf{q}(t)$ and the transition matrix \mathbf{p} corresponding to $\{q_n(t)\}$ and $\{p_{nm}\}$, respectively, where p_{nm} is the probability of a transition from state m to state n . Furthermore $\mathbf{q}(0)$ is an initial probability distribution. Assuming the system is *ergodic*, i. e., all elements of \mathbf{p}^t are non-zero, the limit

$$\mathbf{\Pi} = \lim_{t \rightarrow \infty} \mathbf{p}^t \cdot \mathbf{q}(0) \quad (156)$$

exists and does not depend on the initial distribution $\mathbf{q}(0)$. A further transition does not change this limit, i. e.

$$\mathbf{p} \cdot \mathbf{\Pi} = \mathbf{\Pi} \quad (157)$$

which is called *steady-state condition* and the transition matrix \mathbf{p} has to be chosen appropriately. Assuming *microscopic reversibility* reading $p_{mn}\Pi_n = p_{nm}\Pi_m$ eq. (157) is automatically fulfilled.

In practice one generates a trial state n by applying a small, random displacement $\mathbf{r}_i \rightarrow \mathbf{r}_i + \Delta\mathbf{r}$ of an arbitrary particle. The probability α_{nm} of being in state m and choosing a trial state n depends on this displacement,

i. e., on $\Delta\mathbf{r}$. Metropolis et al. [88] made a choice for the transition probability, which is commonly used today, reading

$$p_{nm} = \begin{cases} \alpha_{nm} & \text{if } \Pi_n \geq \Pi_m \\ \alpha_{nm} \frac{\Pi_n}{\Pi_m} & \text{if } \Pi_n < \Pi_m \end{cases} \quad (158)$$

which satisfies eq. (157) assuming that choosing n while being in m is equally probable as choosing m while being in n . The first case in eq. (158) means that the probability of choosing a trial state equals the transition probability for $m \rightarrow n$ if n is more or equally probable than m , i. e., the trial state is *accepted* unconditionally. If n is less probable then the trial state will be accepted with a probability Π_n/Π_m . Otherwise it will be rejected and the system remains in state m . For a many-particle system with an interaction potential V_N the probability of finding the system in state n is given by the Boltzmann factor $\Pi_n = \exp[-\beta V_N(n)]$. With eq. (158) it follows that the trial state is accepted unconditionally for $V_N(n) \leq V_N(m)$, whereas for $V_N(n) > V_N(m)$ it is accepted with the probability

$$\frac{p(\tilde{\mathbf{r}}_n^N)}{p(\tilde{\mathbf{r}}_{n-1}^N)} = \min \left(1, \exp \left[-\frac{E_{pot}(\tilde{\mathbf{r}}_n^N) - E_{pot}(\tilde{\mathbf{r}}_{n-1}^N)}{k_B T} \right] \right) \quad (159)$$

which is derived using eq. (89). In eq. (159), the reduced units for \mathbf{r} are used given in eq. (146). In practice, this means that the simulation box with lengths L_x , L_y , and L_z can be treated as a unit cell (see sec. 4.1 for more details).

Applying changes in the form of the probability distribution (see sec. 3.1) and the generation of the trial states makes the MC method accessible for other ensembles which is briefly described in the following.

The grand canonical ensemble of sec. 3.2 is realized by inserting one particle at a arbitrary position or destructing an arbitrary particle. For one MC step $\tilde{\mathbf{r}}_{n-1}^N \rightarrow \tilde{\mathbf{r}}_n^{N \pm 1}$ where n denotes the step and \pm indicates insertion and destruction, respectively, this is done with the transition probability derived from eq. (96)

$$\frac{\tilde{p}(\tilde{\mathbf{r}}_n^{N \pm 1}, N \pm 1)}{\tilde{p}(\tilde{\mathbf{r}}_{n-1}^N, N)} = \min \left(1, \exp \left[\mp \ln N_\pm \mp \ln \frac{\Lambda^3}{V} \pm \frac{\mu}{k_B T} - \frac{\Delta E_{pot, \pm}}{k_B T} \right] \right) \quad (160)$$

with $\Delta E_{pot, \pm}$ being the difference between the energy after the step and before it.

One advantage of the grand canonical MC method is that the particle number N , i. e. the density, is not fixed and adapts due to a given chemical

potential which makes it interesting for confined systems with broken translational symmetry in contact with a bulk reservoir. However, GCMC fails if the density (or chemical potential) in the system becomes too large. Then the interparticle space becomes less and the algorithm hardly finds a place to insert a new particle at random. This problem is shown in fig. 7 where several bulk simulations have been applied comparing canonical and grand canonical MC. In fig. 7a the density ρ_b is given for the NVT ensemble and the chemical potential is computed and for the μVT ensemble vice versa. Both methods should yield the same results but the data points reveal that for $\mu^* \gtrsim 43$ consistency is not given any longer. The corresponding bulk pressure in fig. 7b shows this even more clear.

The isobaric-isothermal ensemble with fixed N , P , and T discussed in sec. 3.3 is sampled via MC by applying particle shifts and volume changes ΔV , i. e. for a MC step n the volume changes as $V_n = V_{n-1} + \Delta V$. The sampling step is accepted with the probability

$$\frac{\tilde{p}(\tilde{\mathbf{r}}_n^N, V_n)}{\tilde{p}(\tilde{\mathbf{r}}_{n-1}^N, V_{n-1})} = \min \left(1, \exp \left[-\beta P(V_n - V_{n-1}) + N \ln \frac{V_n}{V_{n-1}} - \beta(E_{pot}(\tilde{\mathbf{r}}_n^N, V_n) - E_{pot}(\tilde{\mathbf{r}}_{n-1}^N, V_{n-1})) \right] \right). \quad (161)$$

Compared to the NVT ensemble it allows changes in the density similar to the grand canonical ensemble. Therefore it is interesting for simulations in confinement as well since it allows to fix the parallel or the normal component of the pressure tensor which can be controlled in experiment. Note, that in practice a trial step to change the volume might be applied after several MC steps.

In an inhomogeneous system, e. g. with confining walls, the diagonal components of the pressure tensor are not equal indicating the broken symmetry. In case of a slit-pore with surfaces parallel to the x - y plane, it is $P_{||} \equiv P_{xx} = P_{yy} \neq P_{zz}$ (see sec. 3.4). Hence, in the isobaric-isothermal ensemble two different pressure values can be held constant, that is $P_{||}$ or P_{zz} . Additionally, L_z or V is constant as well. For the ensemble $NP_{zz}AT$ see [31]. Here, $NP_{||}L_zT$ is discussed. For fixed parallel pressure $P_{||}$ the volume changes are realized by changes in the surface area A of the confining walls, i. e. for a MC step n it is $A_n = A_{n-1} + \Delta A$. The resulting transition probability is

$$\frac{\tilde{p}(\tilde{\mathbf{r}}_n^N, A_n)}{\tilde{p}(\tilde{\mathbf{r}}_{n-1}^N, A_{n-1})} = \min \left(1, \exp \left[-\beta P_{||} L_z (A_n - A_{n-1}) + N \ln \frac{A_n}{A_{n-1}} - \beta(E_{pot}(\tilde{\mathbf{r}}_n^N, A_n) - E_{pot}(\tilde{\mathbf{r}}_{n-1}^N, A_{n-1})) \right] \right). \quad (162)$$

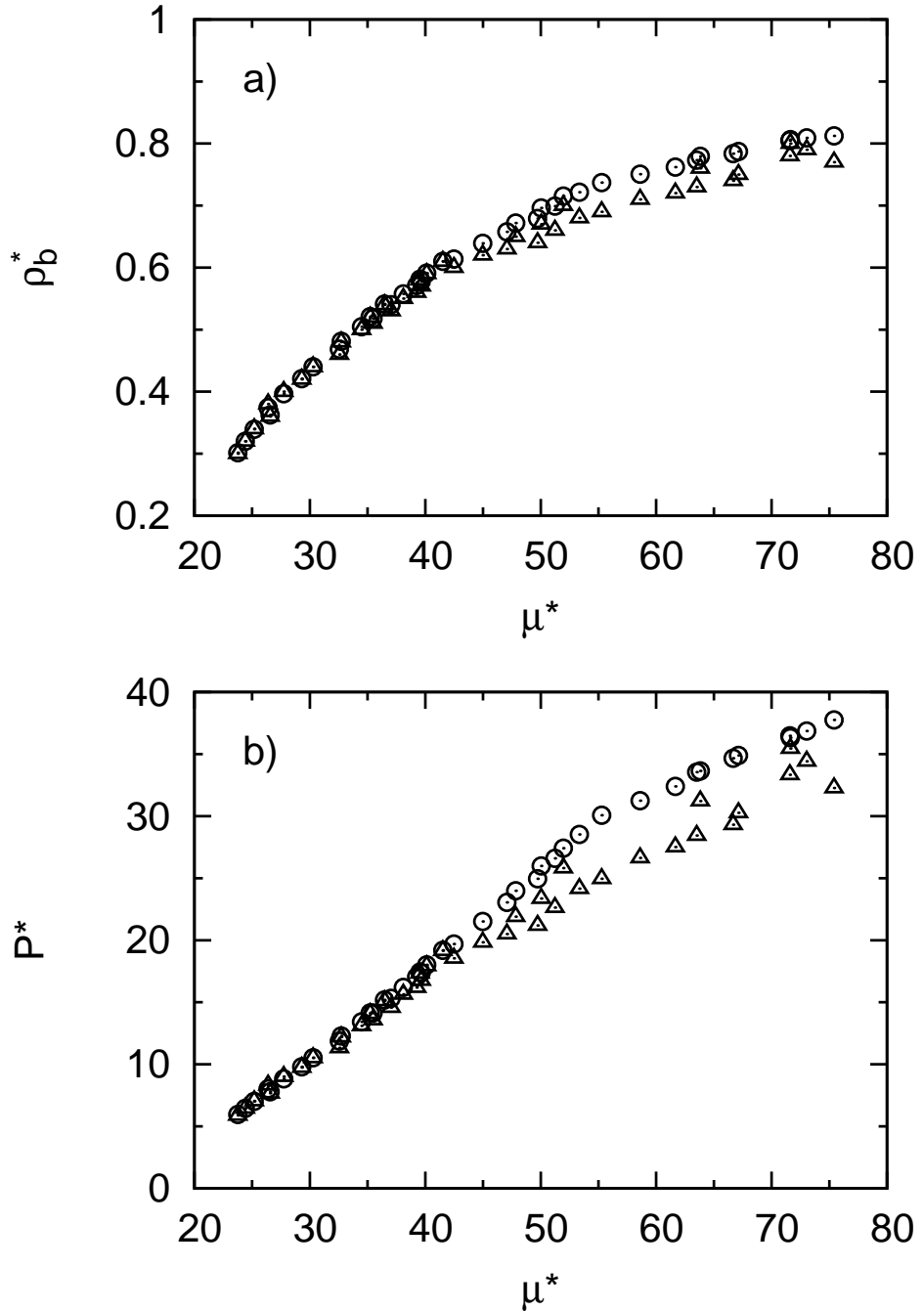


Figure 7: a) Bulk density ρ_b^* and b) bulk pressure P^* as functions of the chemical potential μ^* obtained from GCMC and canonical MC simulations.

4.5 Monte-Carlo method for binary mixtures

As for monodisperse systems, a canonical ensemble is sampled via MC by generating trial states with random particle displacements. One particle i of species j is shifted as $\tilde{\mathbf{r}}_{j,i} \rightarrow \tilde{\mathbf{r}}_{j,i} + \Delta\tilde{\mathbf{r}}$ by a random displacement $\Delta\tilde{\mathbf{r}}$ where we use the reduced units given in eq. (146). From the probability density is sec. 3.7 it follows an acceptance probability for a MC step $n - 1 \rightarrow n$ of

$$\frac{p(\tilde{\mathbf{r}}_{A,n}^{N_A}, \tilde{\mathbf{r}}_{B,n}^{N_B})}{p(\tilde{\mathbf{r}}_{A,n-1}^{N_A}, \tilde{\mathbf{r}}_{B,n-1}^{N_B})} = \min \left(1, \exp \left[-\beta(E_{pot}(\tilde{\mathbf{r}}_{A,n}^{N_A}, \tilde{\mathbf{r}}_{B,n}^{N_B}) - E_{pot}(\tilde{\mathbf{r}}_{A,n-1}^{N_A}, \tilde{\mathbf{r}}_{B,n-1}^{N_B})) \right] \right) \quad (163)$$

where the interaction potential E_{pot} is given in sec. 3.7. In other words, the transition probability is determined by the energy difference of the displaced particle in the potential of all other particles.

An efficient method of sampling a grand canonical ensemble of a binary mixture involves creation and destruction of particles but also identity swaps [6]. The latter changes a random particle into another species and can be considered as destruction and creation of a particle at the same position but with changing identity. Inserting or deleting a particle of species A the transition probability becomes (see sec. 3.7)

$$\begin{aligned} P_{N_A \rightarrow N_A \pm 1} &= \frac{p(\tilde{\mathbf{r}}_{A,n}^{N_A \pm 1}, \tilde{\mathbf{r}}_{B,n}^{N_B}, N_A \pm 1, N_B)}{p(\tilde{\mathbf{r}}_{A,n-1}^{N_A}, \tilde{\mathbf{r}}_{B,n-1}^{N_B}, N_A, N_B)} \\ &= \min \left(1, \left(\frac{V\xi_A}{N_{A,\pm}} \right)^{\pm 1} \exp [-\beta\Delta E_A] \right) \end{aligned} \quad (164)$$

with $N_{i,+} = N_i + 1$ and $N_{i,-} = N_i$ and the energy difference

$$\Delta E_A = E_{pot}(\tilde{\mathbf{r}}_{A,n}^{N_A \pm 1}, \tilde{\mathbf{r}}_{B,n}^{N_B}, N_A \pm 1, N_B) - E_{pot}(\tilde{\mathbf{r}}_{A,n-1}^{N_A}, \tilde{\mathbf{r}}_{B,n-1}^{N_B}, N_A, N_B). \quad (165)$$

Insertion or deletion of a particle of species B is defined analogously. In general for a particle of species i it is

$$P_{N_i \rightarrow N_i \pm 1} = \min \left(1, \exp \left[\mp \ln N_{i,\pm} \pm \ln \frac{V}{\Lambda_i^3} \pm \beta\mu_i - \beta\Delta E_i \right] \right) \quad (166)$$

where the activity $\xi_i = \exp(\beta\mu_i)/\Lambda_i^3$ was inserted. The energy difference is

$$\Delta E_i = E_{pot}(\tilde{\mathbf{r}}_{i,n}^{N_i \pm 1}, \tilde{\mathbf{r}}_{j,n}^{N_j}, N_i \pm 1, N_j) - E_{pot}(\tilde{\mathbf{r}}_{i,n-1}^{N_i}, \tilde{\mathbf{r}}_{j,n-1}^{N_j}, N_i, N_j) \quad (167)$$

with $i, j \in \{A, B\}$ and $i \neq j$.

Using eq. (166), it is straightforward to derive the acceptance probability for a particle swap where a particle of type i is replaced by a particle of type j . Then, the acceptance probability reads

$$\begin{aligned} P_{N_A \rightarrow N_A \pm 1, N_B \rightarrow N_B \mp 1} &= \frac{p(\tilde{\mathbf{r}}_{A,n}^{N_A \pm 1}, \tilde{\mathbf{r}}_{B,n}^{N_B \mp 1}, N_A \pm 1, N_B \mp 1)}{p(\tilde{\mathbf{r}}_{A,n-1}^{N_A}, \tilde{\mathbf{r}}_{B,n-1}^{N_B}, N_A, N_B)} \\ &= \left(\frac{\xi_A N_{B,\mp}}{\xi_B N_{A,\pm}} \right)^{\pm 1} \exp(-\beta \Delta E_{AB}) \end{aligned} \quad (168)$$

with

$$\Delta E_{AB} = E_{pot}(\tilde{\mathbf{r}}_{A,n}^{N_A \pm 1}, \tilde{\mathbf{r}}_{B,n}^{N_B \mp 1}, N_A \pm 1, N_B \mp 1) - E_{pot}(\tilde{\mathbf{r}}_{A,n-1}^{N_A}, \tilde{\mathbf{r}}_{B,n-1}^{N_B}, N_A, N_B). \quad (169)$$

This step can be considered as a deletion and an insertion at the same time. It speeds up the equilibration of the system during the simulation and reduces particle fluctuations in the equilibrium.

This method fails for high particle densities since the available free space for random insertion becomes small, i. e. difficult to sample. Compared to grand canonical monodisperse systems, deviations occur at even smaller densities which is related to the binary character of the system. The higher the asymmetry of the particle sizes is, the stronger are the deviations. This is explained by the fact that a large particle needs more free space than a small particle, i. e. the volume needed for a large particle might be occupied by several small particles. More advanced methods as, e. g., grand canonical cluster move algorithms, handle these problems [120].

4.6 Sampling the chemical potential

As discussed in sec. 3.2 the chemical potential μ is as an independent variable an essential quantity for the grand canonical ensemble. Although the free energy F in the canonical ensemble cannot be directly determined as an ensemble average, μ as an derivative of F can (see sec. 3.1) [52]. This derivative can be sampled within MC simulation via Widom's particle insertion method [125]. The method attempts to insert test particles and calculates the energy change. It is based on the simple thermodynamic relation (see secs. 3.1 and 3.3)

$$\mu = \left(\frac{\partial F}{\partial N} \right)_{VT} = \left(\frac{\partial G}{\partial N} \right)_{PT} \quad (170)$$

which is valid for the Helmholtz free energy and the Gibbs free energy and therefore it can be performed in the canonical and the isobaric ensemble. Here, we focus on the canonical ensemble. With the expression

$F = -k_B T \ln Z(N, V, T)$ (see sec. 3.1) the partial derivative eq. (170) can be approximated for large N using the difference quotient yielding

$$\frac{\partial F}{\partial N} \approx -k_B T \ln \frac{Z(N+1, V, T)}{Z(N, V, T)} \quad (171)$$

where $\partial N = 1$ due to insertion of one test particle. With the partition function $Z(N, V, T)$ from sec. 3.1 the chemical potential can be easily calculated where it splits into an ideal and an excess part reading

$$\mu_{id} \approx -k_B T \ln \left(\frac{V}{(N+1)\Lambda^3} \right) \quad (172)$$

and

$$\begin{aligned} \mu_{ex} &\approx -k_B T \ln \frac{\int d\mathbf{r}_1 \dots \int d\mathbf{r}_{N+1} \exp \left\{ -\frac{U(\mathbf{r}_1, \dots, \mathbf{r}_{N+1})}{k_B T} \right\}}{\int d\mathbf{r}_1 \dots \int d\mathbf{r}_N \exp \left\{ -\frac{U(\mathbf{r}_1, \dots, \mathbf{r}_N)}{k_B T} \right\}} \\ &\approx -k_B T \ln \int d\mathbf{r}_{N+1} \left\langle \exp \left\{ -\frac{\Delta U}{k_B T} \right\} \right\rangle_N \end{aligned} \quad (173)$$

where the last step includes the definition $U(\mathbf{r}_1, \dots, \mathbf{r}_{N+1}) = U(\mathbf{r}_1, \dots, \mathbf{r}_N) + \Delta U$. The brackets $\langle \dots \rangle_N$ in eq. (173) stand for an canonical ensemble average which can be sampled with MC by generating test particles at random positions \mathbf{r}_{N+1} . These uniformly distributed test particles carry out the integral in eq. (173).

This method is limited to small densities in case of hard-core interactions due to technical limitations. At large densities the free space for trial particle insertions becomes small causing many MC trial steps to be rejected, but also a bad sampling of phase space. There are more advanced technics which ensure better sampling of phase space [91]. However, for the density range of interest, Widom's method works quite well.

5 Structure formation at low densities

Confining suspensions induces several effects which cannot be found in bulk systems. At low densities, discussed in this chapter, a slit pore is considered which yields a layering of particles as well as structural forces (or solvation forces). The former is related to a gain of entropy by rearranging the particles in layers parallel to a surface [124]. The structural forces are a consequence of the layering of particles confined between two surfaces. It arises from the mismatch between the thickness of several particle layers (regarding one surface) and the real thickness (separation) of the two surfaces. Thus, the confined suspension film deviates from perfect layering which causes structural forces normal to the surfaces. This effect is also known for molecular fluids, e. g., water [66] and OMCTS [63] using SFA. In this chapter charged, monodisperse suspensions containing silica spheres are modeled and compared with AFM experiments. The real suspension contains spherical, charge-stabilized silica particles. These results were produced and published within this thesis and in cooperation with Yan Zeng and Regine von Klitzing from the TU Berlin [72, 45, 73]. Based on the experiment, the impact of certain system parameters on the structure formation is investigated. These parameters are the particle density, particle size, salt concentration, and the charge of the confining surfaces. The results focus on low densities. High densities are not accessible to the AFM experiment since the particle charge is too small to stabilize them yielding coagulation.

The system parameters are chosen corresponding to the AFM experiments, i. e., $I = 10^{-5} - 10^{-3} \text{ mol l}^{-1}$, $Z = 35, 13$ with corresponding particle diameter $\sigma = 26, 16 \text{ nm}$, and the permittivity of water $\varepsilon_r = 78.5$.

5.1 Layering effect

The layering of interacting particles near a flat surface is an entropy-driven effect which is found for many systems containing interacting particles, e. g., hard spheres [29, 124] and LJ spheres [7]. Closed systems without any exchange of matter or energy tend towards an equilibrium accompanied by an increase of the entropy S . In other words, the change in entropy in this case is $\Delta S \geq 0$ and in equilibrium S reaches a maximum. Without external potentials the particles try to distribute homogeneously in space. Inserting a hard surface prohibits the particles to penetrate the volume taken by the wall. Hence, they form a layer directly at the wall (called contact layer). This layer acts as a "surface" as well possessing a more irregular structure, i. e. a "soft surface". It cannot be penetrated by the particles above it which form a second layer. Coming from thermodynamics, the introduced wall reduces the

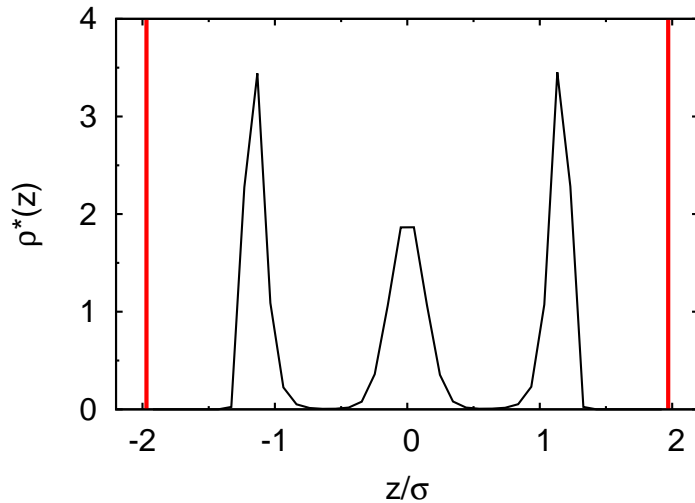


Figure 8: Local density profile of the colloids with $\mu^* = 40.4$ between uncharged, smooth walls (thick, red lines) with $L_z = 3.94\sigma$.

accessible free volume for the particles which is related to a loss in entropy. The same effect has each particle layer on the above particles. Thus, a way to gain entropy is the increase of accessible space. This is done by forming a layer above the wall or above another layer since the particles can "move" more freely in x - and y -direction. Otherwise, they would be stuck between the other particles which decreases their accessible volume.

Now, considering the charged suspension as defined in the introduction of this chapter, fig. 8 depicts an example of a layered film by plotting the local particle density $\rho(z)$ (see sec. 3.4). The corresponding bulk density is set to $\rho_b^* = 0.585$ and the wall separation is $L_z = 3.94\sigma$. One layer corresponds to a peak in $\rho(z)$ and the border between two layers is defined as the density minimum between them. The "softening" of the layers is characterized by the decreasing height and the broadening of the peaks. Considering two facing walls confining the particles, i. e. a slit pore, at small separations a certain number of layers forms for an appropriate separation. Decreasing this separation is inappropriate to promote this number of layers. Hence, the two inner layers begin to merge. The analog behavior is obtained for increasing the separation where the inner layer separates into two layers. The example in fig. 9 demonstrates it in case of a one-layer system. From figs. 9a to c the wall distance increases yielding a separation of the layer into two layers.

This structural effect results in the emergence of structural forces (or solvation forces). The normal component of the pressure tensor $P_{zz}(L_z)$ as

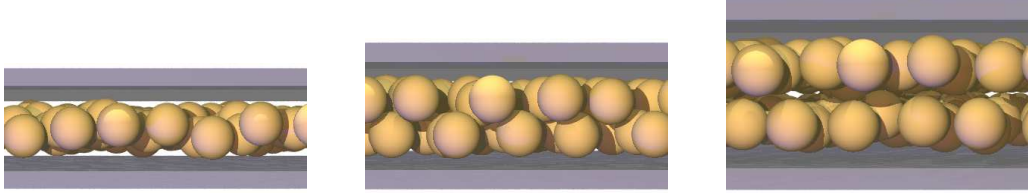


Figure 9: Confined system with $\mu^* = 40.4$ for different wall separations in the side view. The snapshots show a) a single layer at $L_z = 1.9\sigma$, b) two merging layers at $L_z = 2.26\sigma$, and c) two separated layers at $L_z = 2.8\sigma$. The walls are depicted in gray.

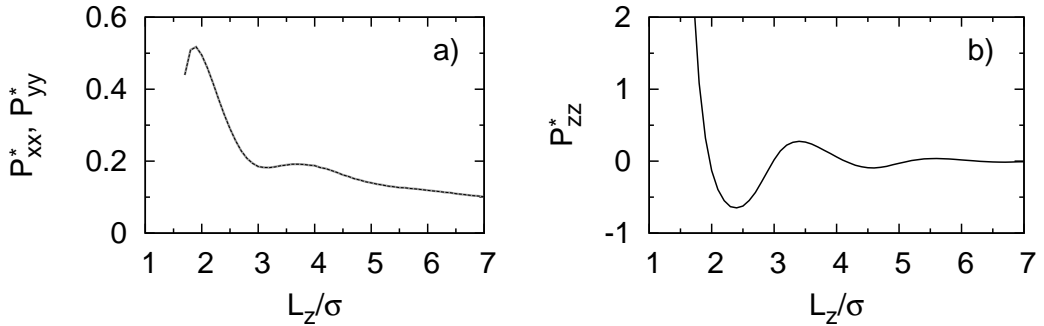


Figure 10: a) Lateral and b) normal pressure components as function of the wall separation L_z for a volume fraction of $\phi = 0.05$. In (a) P_{xx} is plotted as a solid gray line and P_{yy} as a dashed black line.

function of the wall separation L_z exhibits oscillations as well with the same periodicity as the local density profile (see fig. 10). Assume there are two layers and the wall separation is reduced then the layers are pressed together yielding a larger pressure P_{zz} . The pressure reaches a maximum but the pore is getting too narrow for two layers. Hence, both layers begin to merge as shown in fig. 9 which lowers the pressure in z -direction until a minimum in P_{zz} where only one layer exists. Further reduction of the separation yields again an increase of the pressure.

5.2 Influence of the salt concentration

Besides the ions dissolved from the colloidal particles, the concentration of additional salt ions in the solvent (e. g. $NaCl$) has a large influence on the solvation forces induced by the walls. They change the screening of the interaction between the colloids (see eq. (50)). CP-AFM experiments [72]

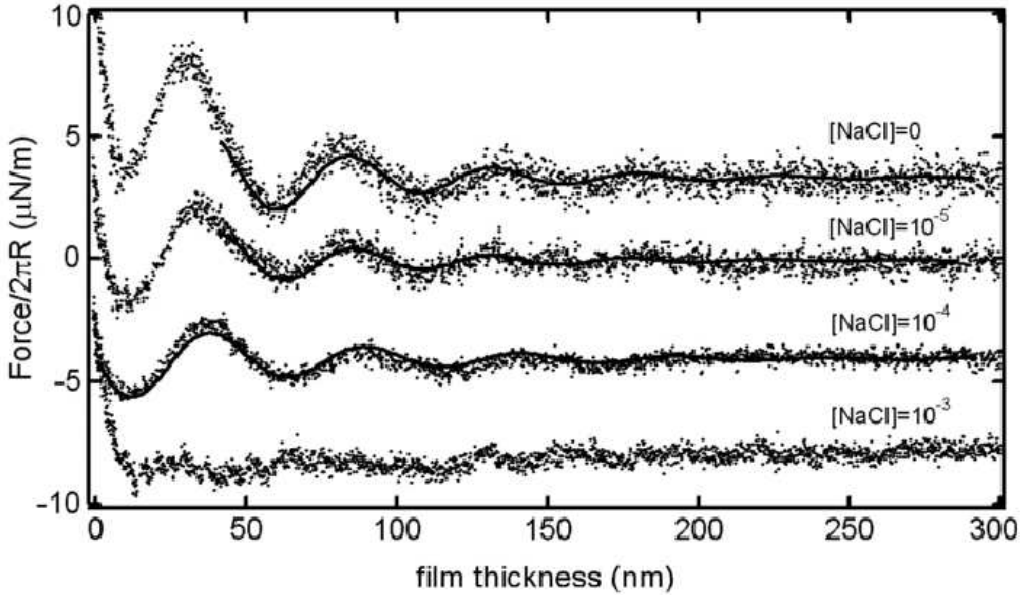


Figure 11: Experimental data of the solvation forces gathered by CP-AFM at $\phi = 7\text{vol}\%$. Four different ionic strengths $I = 0, 10^{-5}, 10^{-4}$, and 10^{-3}mol l^{-1} are considered adjusted by NaCl . The curves are shifted vertically for clarity. The solid lines are fits according to eq. (127).

showed that an increasing salt concentration I damps the amplitude of the solvation forces. As shown in fig. 11, a suspension without salt ($I = 0$) at a volume fraction of $7\text{vol}\%$ clearly shows oscillations up to wall separations of several particle diameters, whereas they almost vanish for $I = 10^{-3}\text{mol l}^{-1}$. In order to verify these experimental findings MC simulations at three different I at the same volume fraction are employed which was published in [72]. Figure 12a contains the results of the normal pressure $f(h)$ and the corresponding solvation force $F(h)$ in reduced units for $I = 10^{-5}, 10^{-4}$ and $5 \times 10^{-4}\text{mol l}^{-1}$ (see sec. 2.4). As found in the experiment the amplitude decreases while increasing I . The fit functions (solid lines) using eq. (126) are valid for the asymptotic regime but provide a good approximation even at small distances. This becomes more clear in the inset of the figure where the logarithm of the simulation results $f(h)$ and the fit functions are plotted. It shows that the wavelength λ_f and the decay length ξ_f of $f(h)$ nicely fit together. These wave- and the decay lengths correspond to the bulk lengths λ_b and ξ_b of the leading order pole of the bulk correlation function at the same chemical potential which is consistent with DFT predictions (see sec. 3.5). We therefore assume that $\lambda_f = \lambda_b$ and $\xi_f = \xi_b$. In fig. 12b simulation results

of the bulk correlation functions for two different I are plotted together with the fit functions using eq. (124). From this plot one can conclude that the salt concentration have an impact on the decay length ξ_b and therefore on ξ_f . The slope $-\xi_b^{-1}$ of the straight line decreases for increasing I which is consistent with the stronger damping of the amplitude of the solvation forces.

In order to complete these results we consider in more detail the volume fraction dependence of the solvation pressure for different salt concentrations. As known from [75] the wavelength of the correlation function behaves like $\lambda_b \propto \phi^{-b}$ where b is around 1/3 which describes an isotropic particle distribution in a three-dimensional space [101]. Even the normal pressure determined in the experiment or via GCMC shows the same dependence, i. e., $\lambda_f \propto \phi^{-b}$, although the system is confined by walls. It states that the interparticle separation in the bulk system is not affected by surfaces. This behavior is also found for varying I . More precisely, λ_f (or λ , see eqs. (126) and (127)) is not affected at all by a changing salt concentration which is shown in fig. 13a. Both GCMC simulations and AFM experiments yield quantitatively the same wavelengths at least for $I = 10^{-5}$ and $10^{-4} \text{ mol l}^{-1}$. Higher salt concentrations are difficult to realize in the experiment. These results verify that the wavelengths of the structural forces are determined by the particle density rather than specific properties of the particle interaction. The latter changes for varying I but does not yield changes in the wavelengths.

The same behavior can be found for the bulk system comparing MC and HNC results in fig. 13b. Again, for varying I between 10^{-5} and $10^{-3} \text{ mol l}^{-1}$ the differences between the wavelengths are negligible. Only for $I = 10^{-3} \text{ mol l}^{-1}$ the values of λ_b are slightly smaller for small ϕ which is in agreement with the HNC results. The same qualitative behavior was found by HNC calculations in [74] where the wavelength was determined by the first peak of the structure factor. However, these results show a more pronounced decrease of the wavelengths for $I = 10^{-3} \text{ mol l}^{-1}$ than the asymptotics results of fig. 13b.

The correlation (decay) lengths exhibit a pronounced dependence on the salt concentration. Keep in mind that as predicted by DFT calculations (see sec. 3.5) both decay lengths ξ_b and ξ_f of the bulk correlation function and the structural forces, respectively, are equal. The asymptotic behavior of ξ_b extracted from MC and HNC is plotted in fig. 14 as function of the volume fraction ϕ . Considering a small fixed volume fraction the results show that ξ_b decreases while increasing I . This effect comes from a stronger screening between the particles since more salt ions are present. For $\phi \gtrsim 0.15$ this influence vanishes and the correlations are more dominated by the hard core of the particles. In this range the correlations behave more like as a HS fluid.

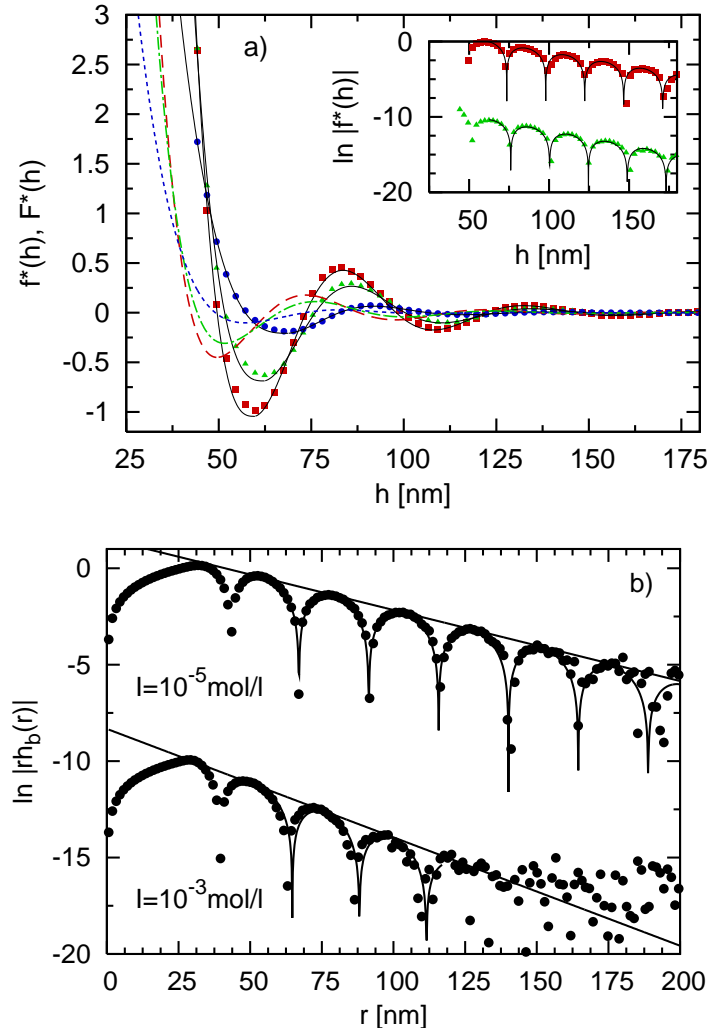


Figure 12: a) GCMC simulation of the solvation pressure $f(h)$ at $\phi = 0.07$ for $I = 10^{-5} \text{ mol l}^{-1}$ (red boxes), $I = 10^{-4} \text{ mol l}^{-1}$ (green triangles) and $I = 5 \times 10^{-4} \text{ mol l}^{-1}$ (blue circles). The black solid lines correspond to the asymptotic fit function eq. (126) using the bulk values λ_b and ξ_b . The dashed and dotted lines show the resulting structural forces $F(h)/2\pi R$ using the corresponding colors as for $f(h)$. The inset shows the logarithm of $f(h)$ and the corresponding fit functions for two of the ionic strengths illustrating the oscillations and the exponential decay with λ_f and ξ_f . b) Corresponding MC data for the bulk system showing $\ln(r|h_b(r)|)$ for $I = 10^{-5} \text{ mol l}^{-1}$ and $I = 10^{-3} \text{ mol l}^{-1}$. The fit function eq. (124) giving the wavelength λ_b (two times the distance between neighboring poles) and the slope of the maxima giving the correlation length ξ_b are plotted as solid lines.

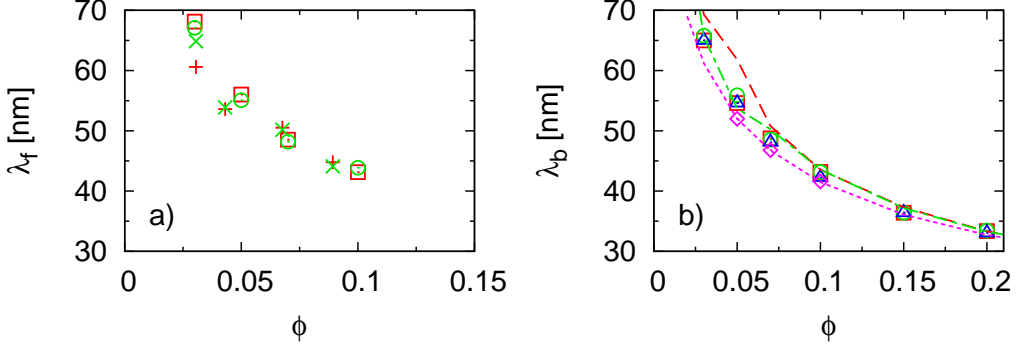


Figure 13: a) Asymptotic wavelength λ_f for different I (in $mol\ l^{-1}$) extracted from GCMC simulations (red boxes for $10^{-5} mol\ l^{-1}$ and green circles for $10^{-4} mol\ l^{-1}$) and CP-AFM experiments (red plus for $10^{-5} mol\ l^{-1}$ and green crosses for $10^{-4} mol\ l^{-1}$) in confinement. b) Canonical MC simulations (red boxes for $10^{-5} mol\ l^{-1}$, green circles for $10^{-4} mol\ l^{-1}$, blue triangles for $5 * 10^{-4} mol\ l^{-1}$, and purple rhombi for $10^{-3} mol\ l^{-1}$) and HNC results (red dashed line for $10^{-5} mol\ l^{-1}$, green dot-dashed line for $10^{-4} mol\ l^{-1}$, and purple dotted line for $10^{-3} mol\ l^{-1}$) in bulk.

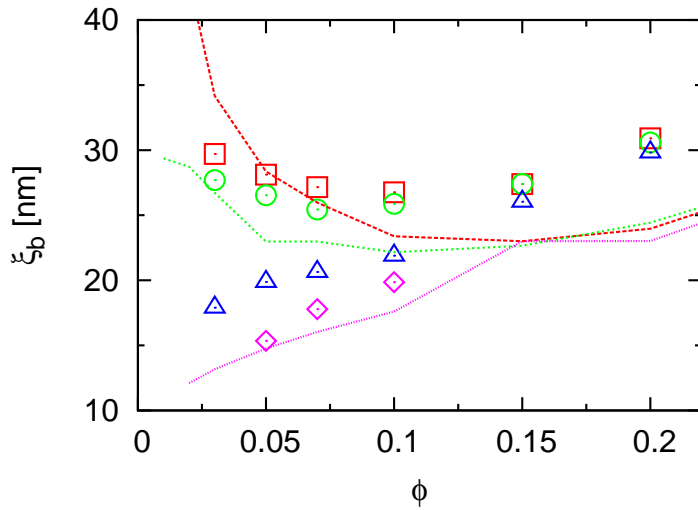


Figure 14: Bulk results for the correlation lengths ξ_b at different values of I (in $mol\ l^{-1}$). The point and line styles are the same as in fig. 13.

But there is another qualitative difference between small and large I . For $I \gtrsim 5 \times 10^{-4}$ the correlation length increases monotonically for increasing ϕ in the considered parameter range which is, as for large ϕ , typical for a HS fluid. On the contrary for small I and $\phi \lesssim 0.1$ the length ξ_b decreases for increasing ϕ . This can be explained by the fact that for increasing volume fraction more counterions are solved which yields a larger screening κ and ξ_b becomes smaller similar to the stronger damping of the correlations for increasing I mentioned above. The MC and HNC results shown in fig. 14 predict the same qualitative behavior as described, but HNC tends to overestimate the dependence on the volume fraction keeping in mind that MC is quasi-exact.

5.3 Influence of the particle size

In this section we investigate the impact of the particle size and the corresponding particle surface charge on characteristic length scales discussed in [73]. The interaction potential of suspensions with, e. g., HS or LJ interactions simply scale with the particle diameter σ , i. e., there are no further changes in the coupling parameter or the interaction range of the potentials. This allows to map wave- and correlation/decay lengths of correlation functions or structural forces for different particle sizes onto each other. This is not necessarily valid for charged suspensions where the surface charge changes with the square of the diameter (see eq. (8)). As a consequence the coupling parameter given in eq. (48) and the screening parameter given in eq. (50) changes as well with the diameter.

Employing MC simulations we choose the particle sizes corresponding to materials used in the CP-AFM experiments (see table 1). These results were published in [73]. For our simulations we set $\sigma = 26\text{nm}$ and 16nm . Using the Grahame equation (see eq. (7)) the corresponding surface charges are set to $Z = 35$ and 13 , respectively. With extensive MC simulations for these two diameters, a wall separation range of several σ , two salt concentrations ($I = 10^{-5}\text{mol l}^{-1}$ and $I = 10^{-4}\text{mol l}^{-1}$) and varying volume fraction ϕ we determined solvation pressure curves from which we extracted wavelengths λ_f and decay lengths ξ_f . Figure 15 contains the resulting solvation pressures. As expected the salt concentration affects the wavelength only marginally which is consistent with [72] (see sec. 5.2). On the other hand one can see a strong impact of the particle size on the amplitude and the wavelength. The latter is visualized in the logarithmic plot of the inset where the distance between the poles corresponds to λ_f . The correlation lengths are also affected and will be discussed later.

Analyzing the oscillating solvation forces obtained in the experiment using eq. (127) one can see that the wavelengths for a certain particle size in a

| Type | Diameter σ [nm] |
|--------|------------------------|
| SM 30 | 9 ± 2 |
| HS 40 | 16 ± 2 |
| TMA 34 | 25 ± 2 |

Table 1: Experimental results for the diameters of the Ludox particles investigated.

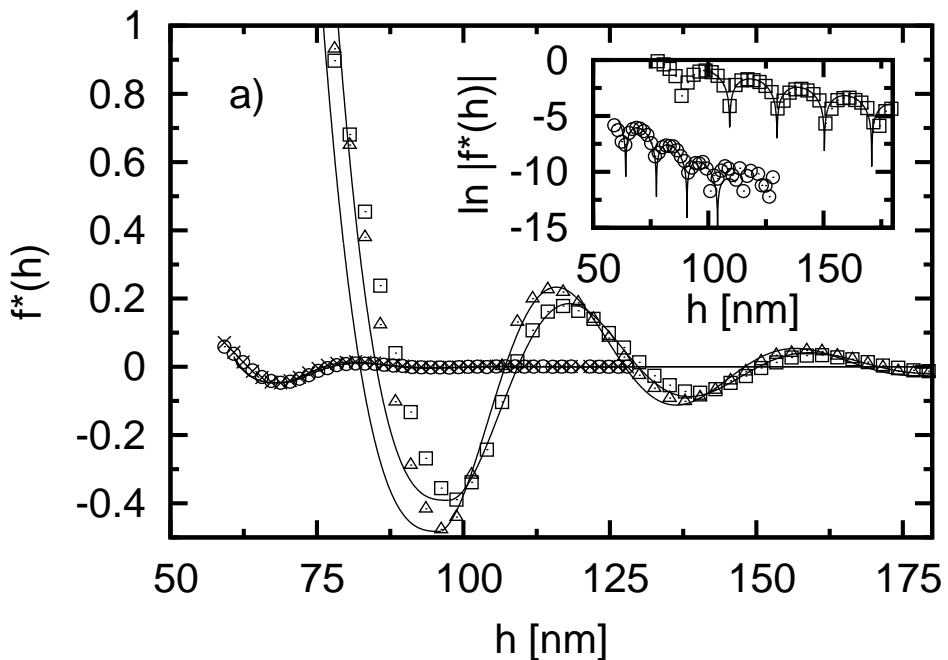


Figure 15: Impact of particle size on the solvation pressure shown via GCMC simulations in confinement using particles of diameter 26 nm (squares: $I = 10^{-4} \text{ mol l}^{-1}$, triangles: $I = 10^{-5} \text{ mol l}^{-1}$) and 16 nm (circles: $I = 10^{-4} \text{ mol l}^{-1}$, crosses: $I = 10^{-5} \text{ mol l}^{-1}$). The chemical potential of the systems corresponds to a bulk volume fraction of $\phi = 0.1$. The inset shows the solvation pressure on a logarithmic scale.

logarithmic plot against particle density $\rho = (6/\pi)\phi\sigma^{-3}$ lay on lines with a slope of about $-1/3$ (see fig. 16a). One would expect that λ obeys the scaling rule $\lambda = c\rho^b$ with $b = -1/3$ and an intercept of $c = 1$ [101, 74]. This would mean that the wavelength equals the mean interparticle distance. In fig. 16a this case, which we refer to as the "ideal" case, is indicated by a dashed line. Assuming that the scaling rule holds for silica spheres as well all data points should fall on one master curve. However, the prefactor c somewhat differs from this ideal case and the extracted prefactors are $c_{SM} = 1.23$, $c_{HS} = 0.93$ and $c_{TMA} = 1.04$. The data points are within the error bars which originate from an uncertainty in the size of the particles. Assuming that these deviations mainly come from this uncertainty we decided to adapt the particle sizes for these results within the error bars which changes the particle densities ρ . Figure 16b shows that the data points fall onto the master curve (ideal case) using slightly different diameters which are 26nm , 15nm and 11nm for TMA 34, HS 40 and SM 30, respectively. The resulting prefactors are $c_{SM} = 1.0095$, $c_{HS} = 0.9936$ and $c_{TMA} = 0.9988$.

For the MC simulations we used similar diameters which are $\sigma = 26\text{nm}$ for TMA 34 and 16nm for HS 40. Since for the smallest particles SM 30 the simulated solvation pressure curves decay very fast, it is difficult to determine λ_f . The MC results are drawn in fig. 16c together with the experimental data from fig. 16b. They again obey the scaling rule $\lambda_f = c\rho^b$ but deviations from $c = 1$ and $b = -1/3$ occur which cannot come from an uncertainty of the particle size since σ clearly determines λ_f and ρ in the simulation. The values for λ_f decay faster than the ideal case (see table 2). Using two different values for I we can also exclude that the data points are sensitive to an uncertainty of the salt concentration which is difficult to measure in the experiment. The results are more or less independent of I which was discussed in sec. 5.2. Hence, we think that beyond the particle size other effects exist influencing the structure of the confined suspension. One aspect, which might have an influence on the wavelength and might yield a deviation from the "ideal" case, is the fact that the particle charge $Z \propto \sigma^2$ (see eq. (8)). Thus, the coupling parameter W and the screening κ given in eqs. (48) and (50), respectively, change with σ as well. This yields a dramatic change of the screened Coulomb potential. However, we note that the analysis of the solvation pressure curves is not exact since the used fit function given in eq. (126) is only valid for the asymptotic range where the amplitudes of the pressure are getting very small in the order of numerical fluctuations.

The oscillatory behavior of the solvation pressure originates from the microscopic particle interaction. To illustrate the non-trivial impact of the particle size on the interaction we consider bulk correlation functions $g(r)$. Remind that the asymptotic bulk wave- and decay length λ_b and ξ_b of $g(r)$

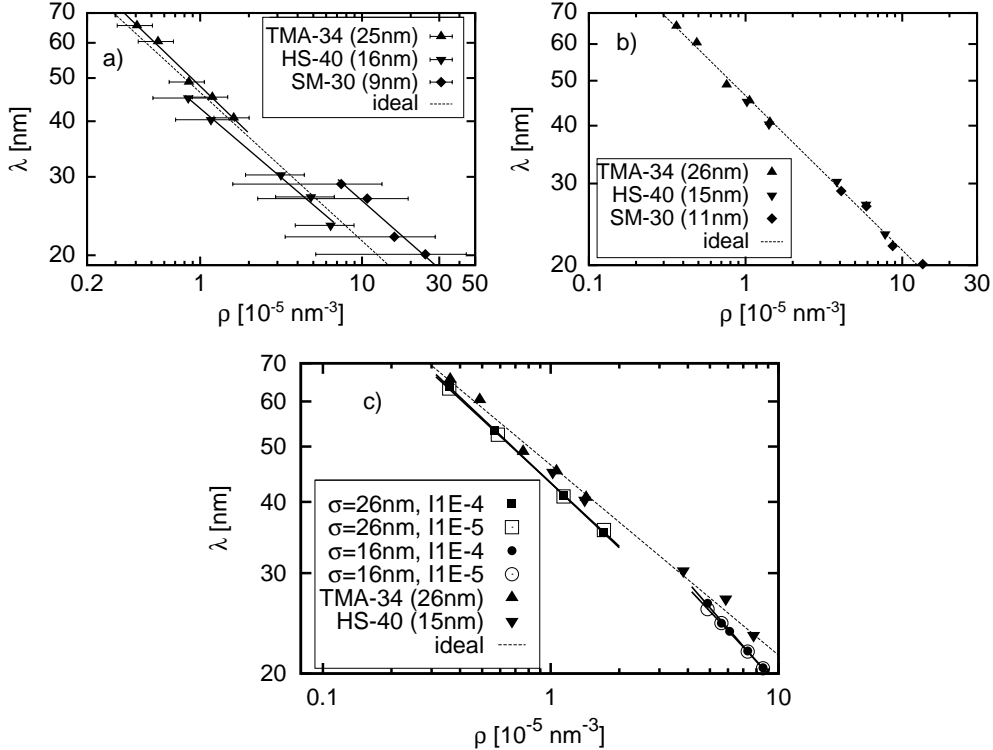


Figure 16: a) Experimental results for the wavelength λ extracted from CP-AFM as function of the particle number density ρ using the determined diameters σ of table 1. The error bars originate from the uncertainties of the particle diameters. The "ideal" curve corresponds to the ideal scaling law $\lambda_f = \phi^{-1/3}$. Same as (a) but assuming slightly different diameters σ yielding a better matching with the ideal scaling law. c) Comparison of GCMC with CP-AFM results for the wavelength as function of particle number density for two different I . The CP-AFM data correspond to the diameters of (b). The smallest particle type $SM - 30$ is neglected. The "ideal" curve scales as $\lambda^{id}/\sigma = (6/\pi)^{-1/3}\phi^{-1/3}$. The CP-AFM data correspond to the diameters of (b).

| Diameter [nm] | I [mol/l] | b |
|---------------|-------------|------|
| 26 | 10^{-4} | 0.38 |
| 26 | 10^{-5} | 0.37 |
| 16 | 10^{-4} | 0.46 |
| 16 | 10^{-5} | 0.43 |

Table 2: GCMC results for the exponents b of the wavelengths resulting from a fit according to $\lambda_f = c\phi^{-b}$.

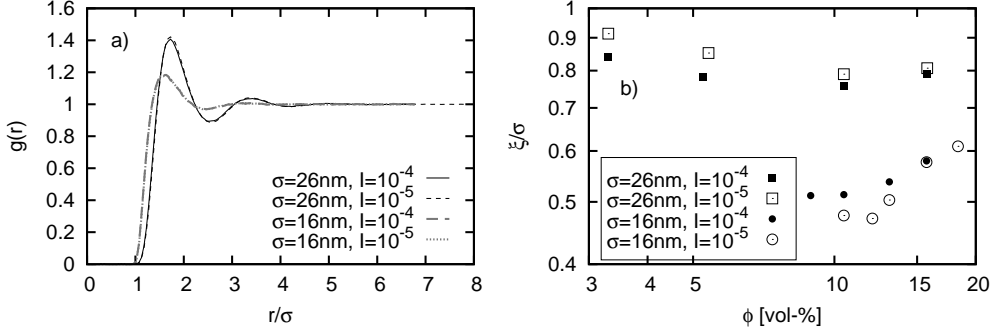


Figure 17: GCMC bulk simulation results for two different particle sizes and two ionic strengths: a) bulk pair correlation functions at $\phi = 0.105$ and b) dimensionless bulk correlation lengths as function of ϕ .

are assumed to equal λ_f and ξ_f of the solvation pressure (see sec. 3.5). For the two particle sizes 26nm and 16nm and a fixed volume fraction $\phi = 0.105$ the correlation functions are plotted in fig. 17a. The amplitudes for the big particles are more pronounced compared to the small particles which is consistent with the relation between Z and σ , since the big particles possessing a larger charge have a stronger interaction. Again, the salt concentration I does not seem to have a big influence on $g(r)$ for the considered parameters. A more detailed information is given by the correlation length ξ_b which we determined by a pole analysis using eq. (124) for varying ϕ (see fig. 17b). In contrary to the wavelength the quantity ξ_b scaled by the particle diameter σ cannot be mapped onto a master curve. This was described in the previous section 5.2 in fig. 14. The correlation lengths for the big particles are much higher than for the small particles. This is consistent with the finding in fig. 17a and the relation between diameter and charge. The influence of I on ξ_b for the big particles is consistent with the results from [72] where a larger value of I slightly decreases ξ_b especially for small ϕ . For the particles with 16nm it is the other way round. This might originate from other effects we did not include in our model. However, we note that the determination of ξ_b in the asymptotic range, where the used fit function is valid, is more inaccurate than for λ_b , especially for the small particles with faster decaying correlations. Furthermore, the findings of fig. 17b for the bulk system are not consistent with the experimental findings in confinement, keeping in mind the assumption $\lambda_b = \lambda$ and $\xi_b = \xi$. There, the fit function eq. (127) gives the decay lengths $\xi = 54\text{nm}$ and $\xi = 37\text{nm}$ for TMA 34 at $\phi = 0.07$ and HS 40 at $\phi = 0.068$, respectively. The scaled correlation length is $\xi/\sigma \approx 2$ for both particle types. This might be an inaccuracy of the model or the

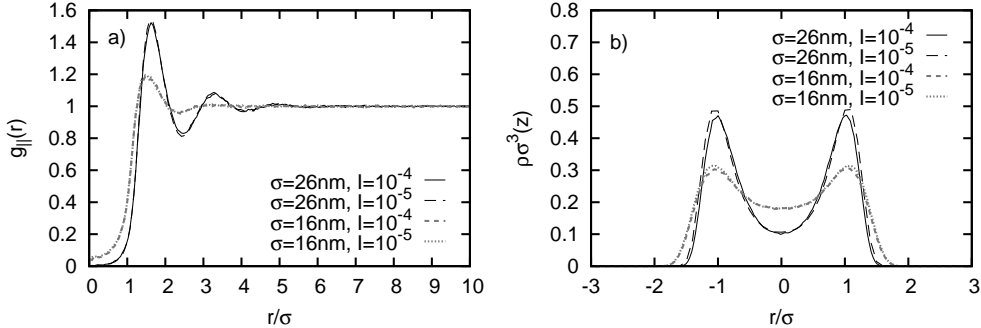


Figure 18: GCMC simulations in confinement for different I and $\sigma = 26(16)\text{nm}$ yielding a) in-plane pair correlation functions and b) local density profiles at bulk packing fraction $\phi = 0.105$ and $L_z = 5.3(5.9)\sigma$.

used parameters since the correlation (or decay) length is a highly sensitive quantity. On the other hand the experimental extracted values for ξ have large error bars.

It is interesting that the influence of σ on the microscopic structure also occurs in the confined system. The in-plane correlation functions $g_{\parallel}(r)$ of the particle layers between the confining walls in fig. 18a exhibit the same behavior as $g(r)$ in fig. 17a, i. e., the amplitudes and the correlation lengths for the small particles are smaller than for the big particles. The corresponding local density profiles scaled on the diameter of the particle type exhibit a softening of the layers for smaller particles which is a fingerprint of the changed particle interaction. However, the mean layer distance is only slightly affected which is consistent with the findings from figs. 16a to c concerning the scaled wavelengths since both quantities are related with the mean particle distance in the system.

5.4 Impact of surface charges on structural forces

CP-AFM experiments showed that the material of the confining surfaces has a crucial impact on the solvation forces. One aspect is the presence of surface charges resulting, e. g., from hydration or dehydration processes [20]. In order to model this a modified fluid-wall interaction potential was introduced given in eq. (70) [45]. The theoretical background and the results, presented in this section, were published in [45]. This section will discuss these effects and compares the theoretical results with the experimental findings. It is shown that surface charges have a crucial impact on the interaction between surface and macroions whereas the soft-wall potential given in eq. (51) fails

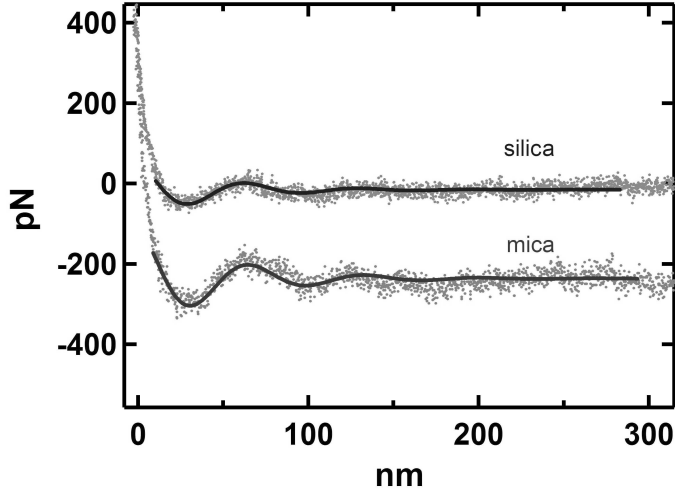


Figure 19: Solvation forces determined by CP-AFM using silica or mica surfaces for $\phi = 0.033$ and $\sigma = 25 \pm 2\text{nm}$ (see table 1). The solid lines correspond to eq. (127) and the data points are shifted for clarity.

to reproduce the experimental findings.

The origin of the impact of the surfaces is a surface potential $\psi_S \neq 0$ which determines the surface charge density depending on the ion concentration of the surrounding solution. A theoretical expression for this is given by the Grahame equation given in eq. (7). On one hand the surface charges increase the Coulombic repulsion of the surface. On the other hand the surface charge results from the solvation of counterion from the surface which are solved in the solution and change the screening in the whole system.

In the experiment a suspension of silica spheres at fixed volume fraction $\phi = 0.033$ ($\rho_b^* = 0.063$) and salt concentration $I = 10^{-5}\text{mol l}^{-1}$ was considered. The force-distance curves using a silica or mica sphere at the top of the AFM cantilever are shown in fig. 19. The higher surface charge of the mica walls yields a pronounced enhancement of the oscillating force compared to the silica walls. The amplitudes and the wavelengths quantifying the influence of the charge can be determined using the fit function eq. (127). The results summarized in table 3 shows that the amplitude A is about twice times larger for mica than for silica surfaces whereas the wavelength λ is unaffected. The fact that the asymptotic wavelength λ does not change is reasonable since it is determined by the local structure of the suspension but not affected by the confinement. It verifies the theoretical prediction from OZ theory and DFT (see eq. (127)).

| ψ_S [mV] | A [N] | λ [nm] |
|---------------|-----------------------|----------------|
| -80 (silica) | 6.9×10^{-11} | 66.6 |
| -160 (mica) | 1.3×10^{-10} | 67.0 |

Table 3: Amplitudes and wavelengths corresponding to CP-AFM results shown in fig. 19.

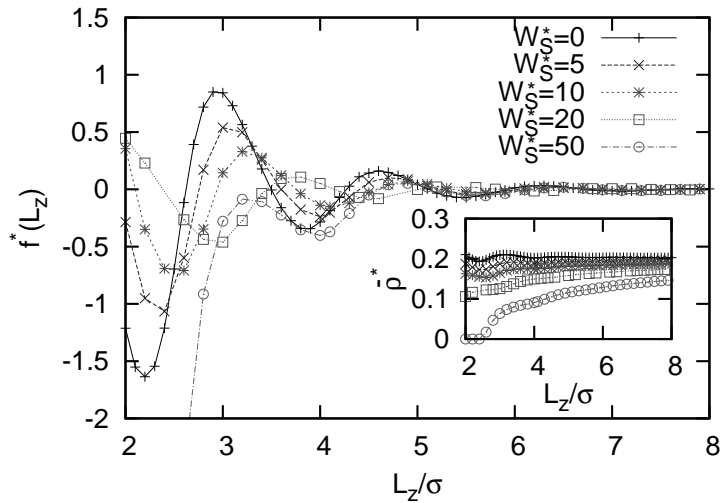


Figure 20: Solvation pressure results at a bulk density $\rho_b^* = 0.2$ for varying surface charges using eq. (126). The coupling parameter $W_S^* = \beta W_S$ corresponds to $\psi_S = 0, -2.7, -5.4, -10.9$, and -27.7mV . The related mean pore density is depicted in the inset.

A first attempt to model the wall charge dependence observed is given in eq. (76) which is a Yukawa-like interaction potential between a sphere and a plate. The wall charge is taken into account in the coupling parameter W_S whereas the screening is described by the fluid-fluid κ , i. e., additional counterions dissolved from the walls do not change the screening in the system. An increasing surface potential ψ_S yields an increasing W_S where $W_S = 0$ corresponds to a uncharged soft wall. The GCMC results are plotted in fig. 20 for $\psi_S = 0, -2.7, -5.4, -10.9$ and -27.7mV . The oscillating solvation pressure $f(L_z) = P_{zz} - P_{bulk}$ is damped with increasing W_S and shifted to larger wall separations which is consistent with the picture of an increasing repulsion and effective narrowing of the slit pore. The mean density $\bar{\rho}^*$ decreases with increasing W_S especially at small distances. As expected the pressure goes to the bulk pressure for $L_z \rightarrow \infty$ and the mean pore density reaches the bulk density. For the largest coupling parameter considered ($W_S^* = 50$)

the particles are squeezed out of the slit pore in the range $L_z \lesssim 4.5\sigma$ and the pressure drops down, i. e. in this range it does not oscillate around the bulk pressure. This surface potential of $|\psi_S| = 27.7mV$ is much smaller than $|\psi_S| = 80mV$ or $180mV$ for silica and mica surfaces, respectively, used in the experiment. For both values the considered fluid-wall potential would squeeze out all particles in the considered L_z range due to the monotonically increasing repulsion. This contradicts the experimental results. Especially the force enhancement cannot be reproduced.

With this background it is clear that our ansatz for the fluid-wall interaction needs to be modified. The simplest step in this direction is a modification of the screening as introduced in sec. 2.6 which takes additional wall counterions for the fluid-wall potential into account. Following the arguments of sec. 2.6 saying that the counterions tend to localize near the walls, the new contributions are marginal for the fluid-fluid interaction within DLVO theory. In [26] the ff-interaction including wall counterions yielded a marginal impact on local density profiles of the macroions. Further simulations (not published) have been employed for supporting our paper [45] where different wall separations and densities were considered. Comparing local density profiles and correlation functions including or excluding the wall counterion contributions to the ff-interaction showed that an influence of the additional counterions is visible but small. It is shown for two examples in figs. 21a to d where the local density $\rho^*(r^*)$ and the correlation function $g_{||}(r^*)$ is plotted for the bulk densities $\rho_b^* = 0.2$ and 0.5 at $L_z = 4.0\sigma$. The impact can be seen more clearly in the normal density profiles rather than in the in-plane correlations. The former shows for small densities a somewhat more pronounced layering if the counterions are included. The latter, plotted in figs. 21b and d, does not reveal clear evidence of an impact on the interaction between the particles. The impact found in $\rho^*(r^*)$ is, however, small. Thus, we neglect the wall counterion contribution to the ff-interaction in this thesis [45].

Solvation pressure curves for the surface potential range $|\psi_S| = 0-160mV$ have been determined using the modified fluid-wall interaction potential given in eq. (70) within GCMC simulations (see fig. 22a). In order to analyze characteristic lengths the results are fitted using eq. (126). This fitting function holds even for small distances as can be seen in the plot although it is only exact for the asymptotic range. Different effects induced by the wall charge are obtained from the fitting data summarized in table 4. Within the range $0 < |\psi_S| < 40mV$ the amplitude of $f(L_z)$ decreases which was also found for the simple model of eq. (76). However, for larger ψ_S the amplitude increases again. Furthermore, the oscillations are shifted towards larger wall separations up to $|\psi_S| \approx 40mV$ and for larger $|\psi_S|$ they are shifted back. Both observations reflect the non-monotonic behavior of the repulsion of the

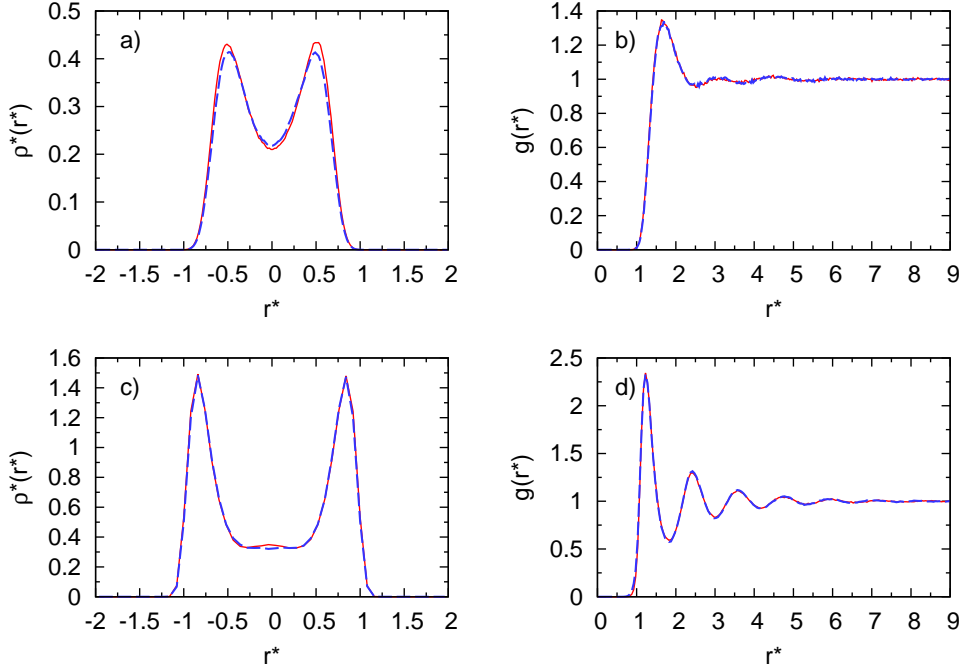


Figure 21: Local density profiles $\rho^*(r)$ at $L_z = 4.0\sigma$ for a) the bulk density $\rho_b^* = 0.2$ and c) $\rho_b^* = 0.5$. The corresponding in-plane correlation functions $g_{||}(r)$ are shown for b) $\rho_b^* = 0.2$ and d) $\rho_b^* = 0.5$. The red solid lines are results using ff-interactions containing the wall counterions whereas the blue dashed lines are without counterion contributions.

| ψ_S [mV] | P_{max}^* | A_f^* | θ_f | λ_f^* | ξ_f^* | F_{max}^* |
|---------------|-------------|---------|------------|---------------|-----------|-------------|
| 0 | 0.850 | 15.17 | 5.82 | 1.600 | 1.076 | 0.2657 |
| -40 | 0.138 | 15.52 | 11.72 | 1.650 | 1.088 | 0.0629 |
| -80 | 0.228 | 17.84 | 11.54 | 1.628 | 1.106 | 0.0755 |
| -120 | 0.372 | 18.20 | 9.75 | 1.600 | 0.965 | 0.1203 |
| -160 | 0.586 | 18.31 | 8.14 | 1.600 | 0.997 | 0.1802 |

Table 4: Fitting parameters related to the results of fig. 22 at $\rho_b^* = 0.2$ showing the height of the first peak of the solvation pressure, P_{max}^* , the resulting maximum of the force, F_{max}^* , the amplitude $A_f^* = A_f \sigma^3 / k_B T$, the wavelength $\lambda_f^* = \lambda_f / \sigma$, and the decay length $\xi_f^* = \xi_f / \sigma$.

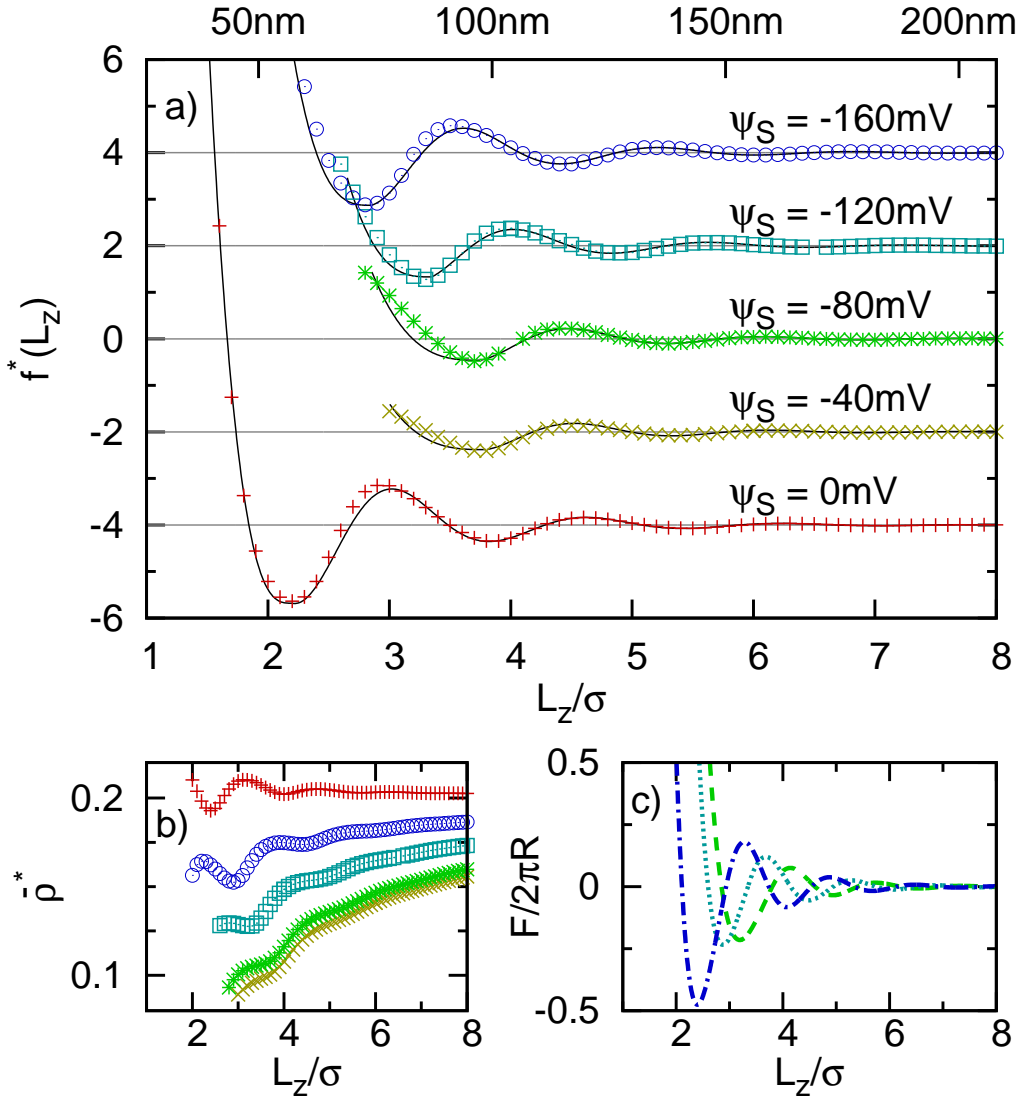


Figure 22: GCMC simulations at $\rho_b^* = 0.2$. a) Solvation pressure curves using the modified fluid-wall interaction eq. (70) for different $\psi_S = 0, -40, -80, -120$, and $-160mV$. The curves are shifted for ease of the eye. b) Corresponding mean pore densities. Part c) shows solvation forces $F(L_z)/2\pi R$ for the experimentally interesting surface potentials $\psi_S = -80$ (dashed), -120 (dotted), and $-160mV$ (dot-dashed).

fluid-wall interaction. In more detail, $|\psi_S| \approx 40mV$ plays the role of a “reversal point”. Due to the strong repulsion at small distances in the range $40mV \lesssim |\psi_S| \lesssim 120mV$ all particles are squeezed out even at separations of several particle diameters, i. e. for $L_z \lesssim 3\sigma$. The fitting parameter A_f for the amplitude is affected by the phase shift θ_f and thus inappropriate for investigating the impact of the surface charge. Hence, the height P_{max} of the first maximum of $f(L_z)$ is shown in table 4 reflecting the non-monotonicity. Considering the wall charges $|\psi_S| = 80mV$ and $160mV$, which are relevant for the experiment, P_{max} of the mica surfaces is more than two times larger than for silica surfaces. This qualitatively verifies the experimental findings. The wavelength λ_f and the decay length ξ_f are more or less unaffected by ψ_S . All these findings are consistent with DFT predictions (see sec. 3.5). In more detail, λ_f and ξ_f of the confined system correspond to λ_b and ξ_b of the correlation function in the bulk system at the same chemical potential and temperature since they are related to the microscopic (local) structure of the particles. Therefore, they should not depend on specific properties of the wall potential. Indeed, the fit parameters of the bulk correlation function at $\rho_b^* = 0.2$ which are $\lambda_b^* \approx 1.60$ and $\xi_b^* \approx 1.025$ compared to the values of table 4 verify the DFT predictions.

The mean pore density $\bar{\rho}$ plotted in fig. 22b oscillates as a function of L_z due to the layering of the particle. Furthermore, it reflects the reversing behavior at $|\psi_S| \approx 40mV$ as well as the solvation pressure does. Considering a fixed value of L_z the mean pore density strongly decreases for $0 < |\psi_S| \lesssim 40mV$ and slowly increases for $40mV \lesssim |\psi_S| \lesssim 160mV$. This quantity shows nicely that the particles are squeezed out of the pore in the range $40mV \lesssim |\psi_S| \lesssim 120mV$ due to the strong repulsion as mentioned above, i. e., the value of $\bar{\rho}$ decreases strongly while the ”effective width of the pore“ is decreased.

Corresponding to experiments the solvation forces obtained by integrating the solvation pressure is shown in fig. 22c for three different ψ_S . As observed in fig. 19 the force exhibits a wall-charge induced enhancement in the experimentally accessible range $80mV \lesssim |\psi_S| \lesssim 160mV$.

The influence of ψ_S on the mean pore density $\bar{\rho}$ in fig. 22b is accompanied by changes in the local particle density perpendicular to the surfaces since a stronger repulsion yields an effective narrowing of the slit pore. For the experimentally relevant range $80mV \lesssim |\psi_S| \lesssim 160mV$ the effective broadening might increase the number of particle layers which is shown in fig. 23a. Going from silica walls to mica walls at fixed $L_z = 3\sigma$ broadens the width of the density profile and induces a ”transition“ from a one-layer to a two-layer system. Furthermore, it changes even the inner structure of the layers which becomes clear by assuming a constant mean distance between the two

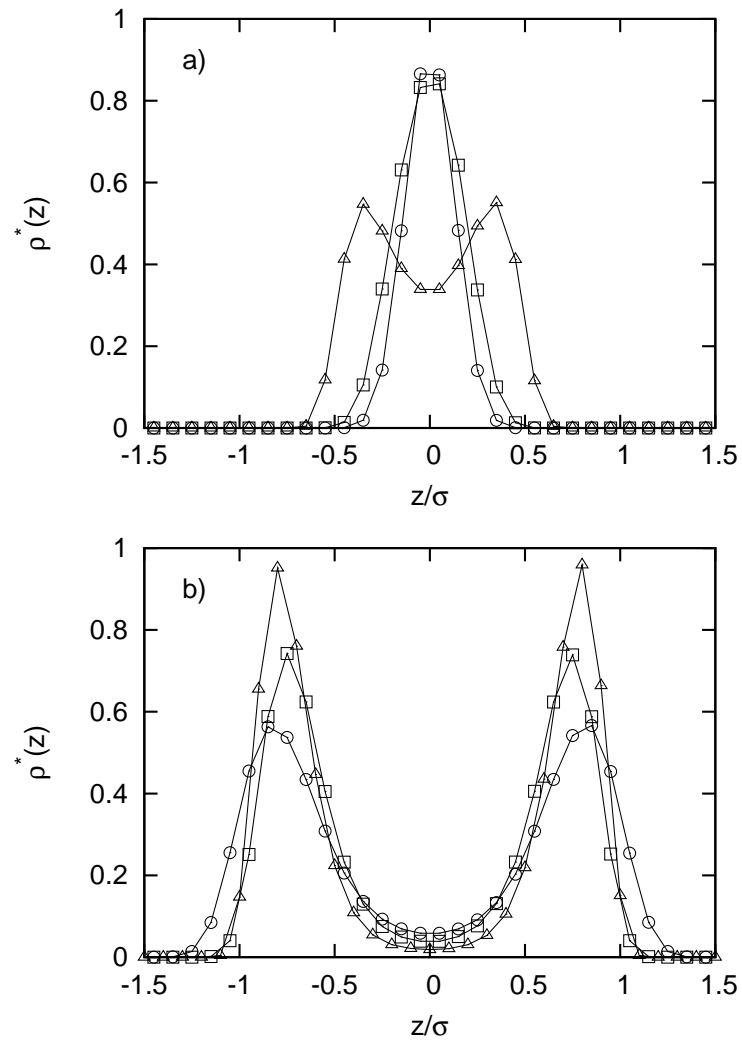


Figure 23: Local density profiles of silica particles at $\rho_b^* = 0.2$ between different charged wall types $\psi_S = -80$ (circles, silica), -120 (squares), and $-160mV$ (triangles, mica) at a) constant wall separation $L_z = 3.0\sigma$ and b) different separations $L_z = 4.8\sigma$ (silica), 4.2σ , and 3.9σ (mica), respectively.

layers of a two-layer system where different ψ_S are related to different L_z . Figure 23b shows the density profiles for $L_z = 4.8\sigma$, 4.2σ and 3.9σ yielding a softening of the layers for decreasing wall charge (mica to silica) characterized by decreasing peak heights and broadening peak width which is an indication for a changed inner structure.

These considerations have been done for a fixed bulk density $\rho_b^* = 0.2$. In order to get a wider view of the system's behavior additional simulations for the density range $0.103 \leq \rho_b^* \leq 0.44$ are employed and summarized in fig. 24. As found before the amplitude A_f and the height of the first maximum P_{max} of the solvation pressure is influenced by ψ_S as shown in figs. 24a and b. Since A_f is affected by the phase shift the quantity P_{max} yields more clear results how strong the oscillations are pronounced. For $|\psi_S| < 40mV$ this quantity decreases and increases for larger values with $|\psi_S| \approx 40mV$ as a reversing point as found in table 4. This effect is enhanced for larger ρ_b , i. e., the wall charge dependence is characterized by larger gradients. Furthermore the absolute values of P_{max} increase with increasing ρ_b . Both observations might reflect the larger interparticle correlations due to a larger density. The wall charge dependence of the phase shift θ_f in fig. 24c showing an increasing and decreasing value with the same reversing point at $|\psi_S| \approx 40mV$ is more pronounced for smaller ρ_b , i. e., smaller densities yield larger gradients of $\theta_f(\psi_S)$, which might reflect the importance of the larger mean particle distance for smaller densities. Keep in mind that θ_f is related to the mean particle distance, i. e., a certain phase shift θ_f for a small density corresponds to a larger distance shift than the same θ_f for a large density. In other words, considering the distance shift as function of ψ_S would exhibit stronger changes of the gradients for varying densities. It is interesting to note that for strong repulsive walls ($|\psi_S| \approx 40mV$) the density dependence of the phase shift becomes small. As predicted by DFT calculations λ_f in fig. 24d is more or less unaffected by ψ_S as discussed before but decreases with increasing ρ_b which is consistent with the picture that the wavelength is related with the interparticle distance of the bulk system [74, 101]. The same is observed for the decay length ξ_f where a trend to increasing values for increasing ρ_b can be seen. However, as mentioned before these results are plagued by large errors since the determination of ξ_f as a fit parameter is inaccurate due to the fast decaying oscillations.

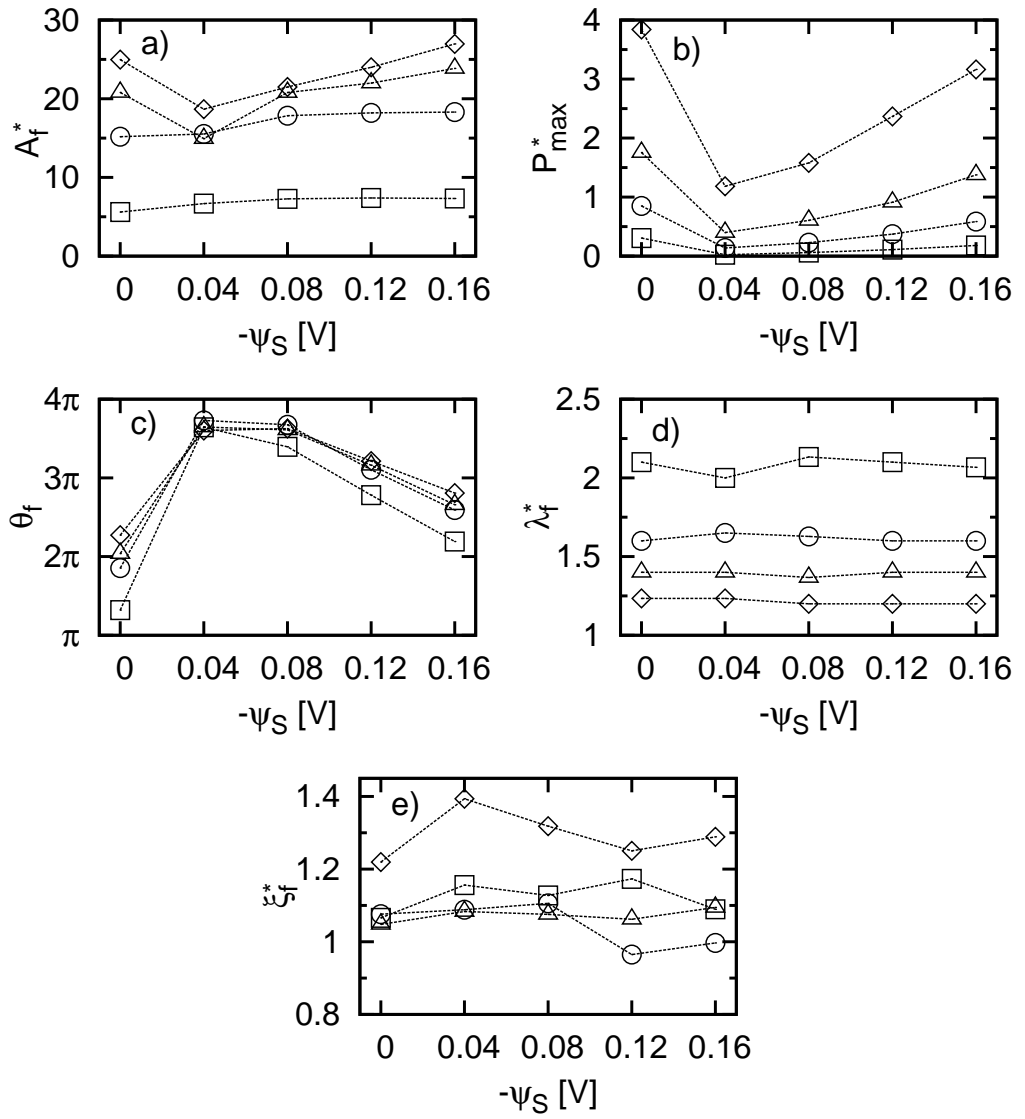


Figure 24: Impact of surface charges on a) the amplitude A_f , b) the height P_{max} of the first maximum of $f(L_z)$, c) the phase θ_f , d) the wavelength λ_f , and the decay length ξ_f . The symbols correspond to the bulk densities $\rho_b^* = 0.103$ (squares), 0.2 (circles), 0.301 (triangles), and 0.44 (rhombi).

6 Crystal-like structuring at moderate and large densities

Fluid-solid phase transitions for charged suspensions modeled via DLVO (see sec. 2.2) are investigated in more detail in this chapter. From former studies it is known that confining surfaces have a deep impact on crystallization phenomena [1, 37]. Beginning with a brief consideration in bulk, the impact of confining walls is studied where we focus on confinement-induced transitions [29] as well as on density-induced transitions. Furthermore, the influence of surface charges of the confining walls is examined. Depending on the system parameters, different crystalline structures are found [107, 108, 37, 102]. These investigations were published in [43, 44].

6.1 Freezing transitions in bulk

Before discussing structural details of confined systems it is interesting to take a look on bulk systems in order to map out the changes induced by the walls [43].

Previous studies [51, 58] showed that pure bulk Yukawa systems without hard cores freeze into body-centered cubic (bcc) or face-centered cubic (fcc) phases for large coupling parameters. The moderate coupling parameters considered here are too small to drive freezing transitions for point Yukawa particles at densities $\rho_b^* < 1.0$. However, as shown in fig. 25 the considered Yukawa particles exhibit at least metastable fluid and solid states which are induced by the soft core of the particles (see eq. (51)) and not by the Yukawa potential. The results of fig. 25 have been obtained using MC within the isobaric-isothermal *NPT* ensemble (see sec. 3.3) since the simple GCMC method fails at these densities. In order to get the (meta)stable branches of the fluid and the solid states the simulations have been performed starting at low or high bulk pressures with random or fcc initial configurations, respectively. The equilibrated configuration was used to simulate the system at a slightly higher or lower pressure in order to avoid jumps to the other branch. The fluid branch is (meta)stable up to $P \approx 90$ whereas the solid branch becomes unstable for $P \lesssim 24$. For the latter the corresponding densities are $\rho_f^* \approx 0.68$ and $\rho_s^* \approx 0.69$. Remind that these densities do not correspond to the coexistence point but to the spinodal line. These densities for a SS system are $\rho_f^* \approx 0.77$ and $\rho_s^* \approx 0.80$ [57] which is higher than for the considered Yukawa system with soft core. In other words, although the Yukawa interaction cannot drive a freezing in this density (pressure) range it shifts the SS freezing transition towards smaller densities. These findings

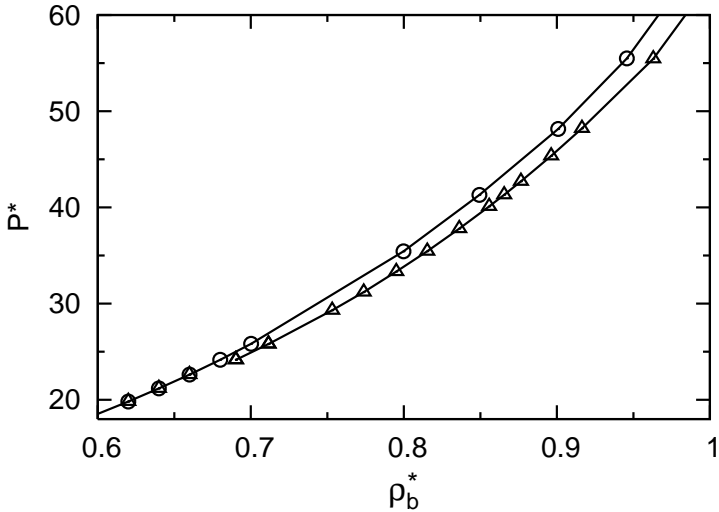


Figure 25: Equation of state for the bulk system. The symbols indicate results from *NPT* simulations started from a random configuration (circles) or a fcc lattice (triangles), respectively. The lines are guides for the eye.

are consistent with HCY models [65].

6.2 Capillary freezing

Introducing soft walls we investigate systems within the grand canonical ensemble where the confined system is in contact with a bulk system of same chemical potential and temperature. We choose $\mu^* = 40.4$ ($\rho_b^* \approx 0.59$) which corresponds to a stable fluid bulk system (see fig. 25). Decreasing the wall separation L_z starting from 10σ , structural changes can be observed considering the solvation pressure given in eq. (112) and in-plane bond order parameters determined via eq. (110). The results are shown in fig. 26. The solvation pressure in fig. 26a exhibits typical oscillations which are a fingerprint of the particle layering. How many layers exist is indicated by numbers which are determined by analyzing local density profiles. As an example, starting at 4σ the pressure is small and increases upon decreasing L_z since the existing layers are compressed which yields for this purely repulsive model enhanced interaction energies and therefore a larger pressure component P_{zz} . At $L_z = 3.5\sigma$ the pressure reaches a maximum where it is energetically favorable to squeeze out one layer or, in other words, to merge one layer into the others. During this process the pressure goes down to a minimum since the mean distance between the layers increases. As known from DFT predictions

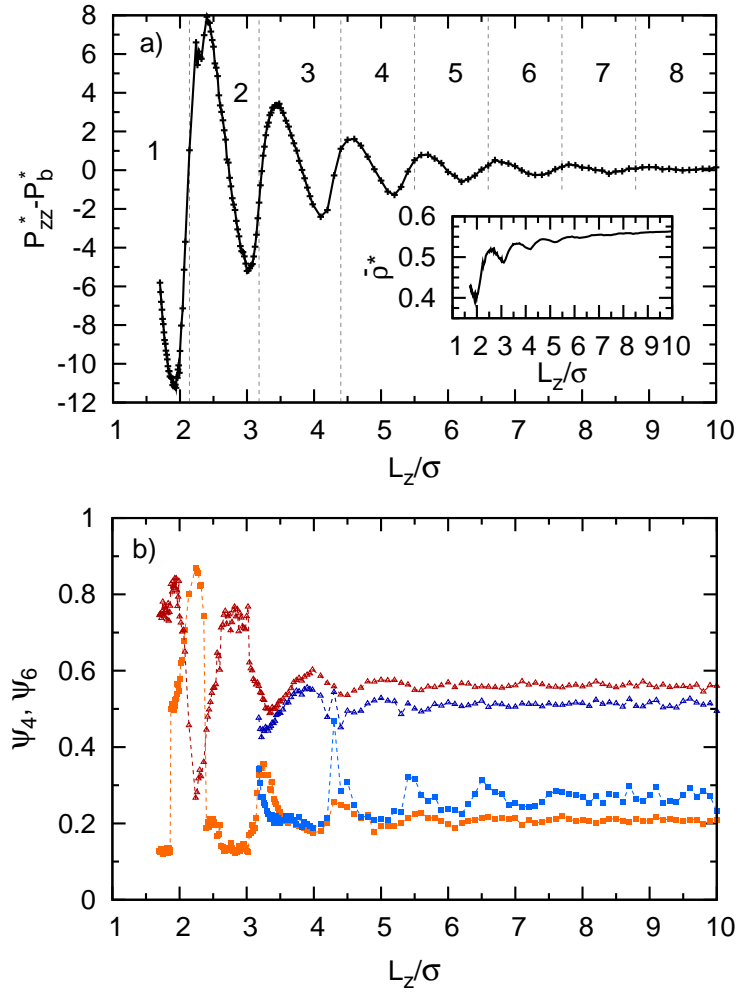


Figure 26: GCMC results for (a) the solvation pressure and the average pore density (inset), and (b) the bond-angle order parameters in the contact layer (ψ_6 : dark red triangles, ψ_4 : light red squares) and in the next inner layer (ψ_6 : dark blue triangles, ψ_4 : light blue squares) as function of the wall separation at $\mu^* = 40.4$. In (a) we have indicated the number of layers related to a given range of wall separations.

(see sec. 3.5) the oscillating pressure can be fitted using eq. (126) for small densities. For small separations this becomes impossible at higher densities as in the considered case. This is due to additional effects influencing the structure of the layers. In the asymptotic range $L_z \rightarrow \infty$, eq. (126) should still hold unless the system is totally frozen. For $L_z \lesssim 5.5\sigma$, the oscillations are apart from the exponential damping somewhat asymmetric.

This picture of additional effects is confirmed by the bond order parameters ψ_6 and ψ_4 determined in each layer. In the same range $L_z \lesssim 5.5\sigma$ these quantities for the contact layers (next to the walls) show deviations from their asymptotic (bulk) behavior in fig. 26b. Decreasing L_z they begin slightly to oscillate and exhibit for $L_z \lesssim 3.5\sigma$ strong alternations between regions of large ψ_4 or ψ_6 values which correspond to crystal-like states. This effect is called *capillary freezing*. Taking a closer look the hexagonal states at $L_z \approx 1.9\sigma$ and 2.8σ correspond to a small pressure P_{zz} in fig. 26a whereas a large pressure is observed for the squared state at $L_z \approx 2.3\sigma$ which is explained as follows. The minimum of P_{zz} emerges by pressing two layers together as mentioned before. This yields a greater amount of particle per layer which prefer (in the capillary freezing regime) a hexagonal structure due to its closer in-plane packing (see sec. 5.1). For the same reason the squared structure emerges. Before two layers are completely merged while decreasing L_z particles are squeezed out which decreases the number of particles per layer. Therefore it is favorable to build a squared structure with a smaller packing compared to hexagonal needing less particles per area. Between these regions L_z is inappropriate to induce crystal-like phases. There, the phase switches from squared to hexagonal or vice versa. Summarizing the important results of fig. 26 we find a crystal structure sequence $1\Delta \rightarrow 2\square \rightarrow 2\Delta$. Such sequences have been found for HS [37] and LJ systems [7] as well. Remind, that the corresponding bulk phases are stable fluid phases, i. e. the crystal-like structures are induced by the confinement. In other words, the confining surfaces seem to shift down the metastable solid branch of fig. 25 which drives for $L_z < 3.5\sigma$ the structural changes in fig. 26.

6.3 Density-induced freezing and solid-solid transition

The capillary freezing was investigated in the previous section for a fixed $\mu^* = 40.4$ ($\rho_b^* \approx 0.59$) where crystal-like states of the contact layers were found for $L_z < 3.5\sigma$ (see fig. 26). To examine the impact of the density on the crystallization simulations at the fixed separation $L_z = 2.9\sigma$ are employed for varying μ . To this end the bond order parameters ψ_4 and ψ_6 for the contact layer are plotted in fig. 27. Upon increasing μ^* the parameter ψ_6 has a value around 0.5 for small $\mu^* \approx 25$ and slowly increases. These states

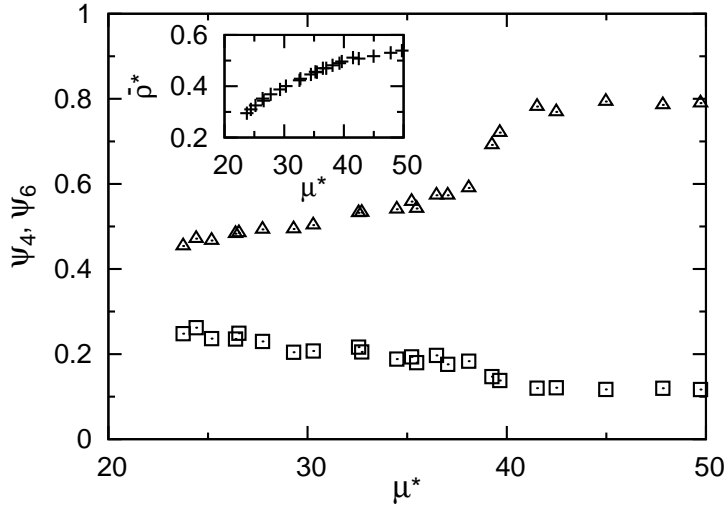


Figure 27: GCMC data for the bond order order parameters ψ_6 (triangles) and ψ_4 (squares), and the average pore density (inset) in the contact layer as functions of μ^* at $L_z = 2.9\sigma$. Since μ^* varies with the bulk density each data point corresponds to a different value of κ .

correspond to fluid-like layers as shown in snapshot fig. 28a. For $38 \lesssim \mu^* \lesssim 41$ the hexagonal order strongly increases up to values of about $\psi_6 \approx 0.8$ which corresponds to hexagonal phases shown in fig. 28b. This onset of crystallization can also be identified by a small kink in the mean pore density in the inset of fig. 27. In fig. 29a the local density profiles are considered for the chemical potentials $\mu^* = 30.28$ and 41.52 . The higher μ^* exhibits more pronounced peaks defining the particle layers which reflects the higher density (or higher chemical potential). The layer distance does not change with μ^* in the considered case pointing out that this quantity is determined by the wall separation but not the density. A typical behavior at high values of μ^* is that the local density drops down to zero between the two layers, i. e. the layers are separated and the exchange of particles between both is a rare event. Keep in mind that the local density considers the center of the spherical particles, i. e. even if $\rho(z)$ drops down to zero the particle layers might penetrate each other in z -direction which is not the case here. However, to maximize the interparticle distances, i. e. minimize the interaction energy in the repulsive system, the layers tend to form staggered structures as in fig. 28b.

The in-plane correlation functions of fig. 29b draw the inner structure of these layers. Whereas for $\mu^* = 30.28$ the function $g_{||}(r)$ has a fluid-like exponential decay long-range correlations are observed for $\mu^* = 41.52$. The latter

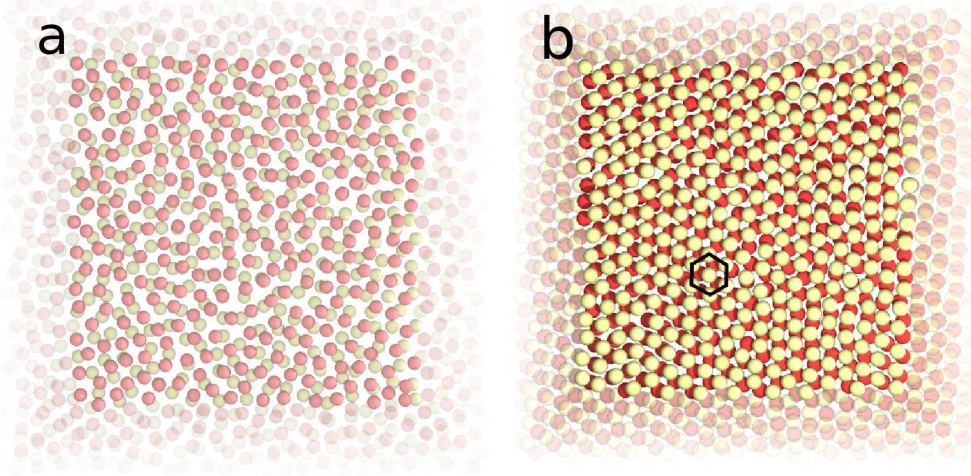


Figure 28: a) Snapshot (top view) of the fluid structure for $L_z = 2.9\sigma$ and $\mu^* = 24.4$, b) Snapshot (top view) of the hexagonal structure for $L_z = 2.9\sigma$ and $\mu^* = 41.5$. The hexagon indicates the arrangement of the nearest in-plane neighbors of a particle. The different colored particles indicate the particle layers.

are typical for hexagonal order characterized by the splitting second peak. Both findings are consistent with the results of the bond order parameters in fig. 27. The fluid-like behavior of the bulk system for both chemical potentials is demonstrated in the inset of fig. 29b. These results are independent of the system size at least up to $N \approx 2500$. It is interesting to note that ground-state calculations of perfect Yukawa bilayers [87] also found hexagonal order for the same system parameters considered here. Note, that the particles in our investigations with moderate charges $Z = 35$ yield weak coupling parameters corresponding to high temperatures whereas for the ground state $T \rightarrow 0$. For more details see [43].

These observations of structural ordering indicated by the bond order parameters are related to freezing phase transitions. The parameters ψ_n alone do not prove the existence of a phase transition, in particular they do not jump. A discontinuity in the order parameter would indicate a first order transition. To this end thermodynamic quantities are considered. In fig. 30 the pressure parallel to the walls is plotted as function of μ . At $\mu^* \approx 41$ the function exhibits a small kink and the slope above this chemical potential is slightly decreased. Comparing with fig. 27 this point is in the vicinity of the strong increase of ψ_6 (onset of crystallization). Similar to the bond order it gives evidence for a transition around this chemical potential since the changed slope reflects the different compressibilities of a fluid and a solid

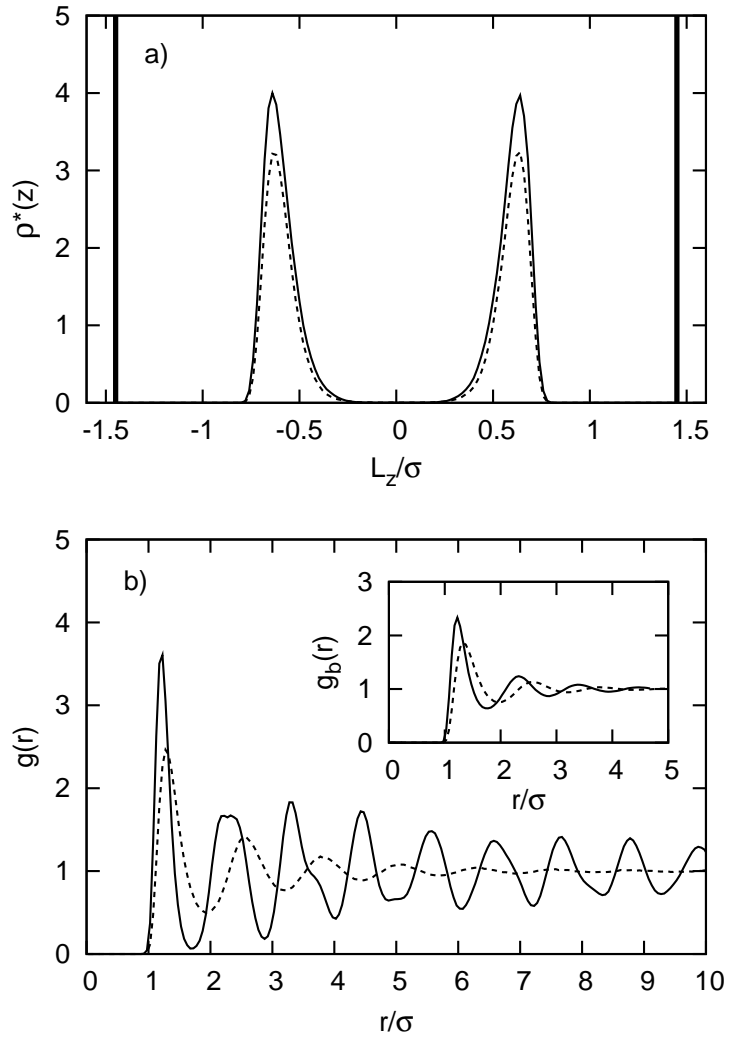


Figure 29: GCMC results for a) density profiles and b) in-plane correlation functions at $\mu^* = 30.28$ ($\rho_b^* = 0.44$, $\kappa^* = 2.322$, dashed line) and $\mu^* = 41.52$ ($\rho_b^* = 0.61$, $\kappa^* = 2.728$, solid line) and $L_z = 2.9\sigma$. In (a) the walls are marked with thick solid lines. The inset in (b) shows the corresponding bulk correlation functions.

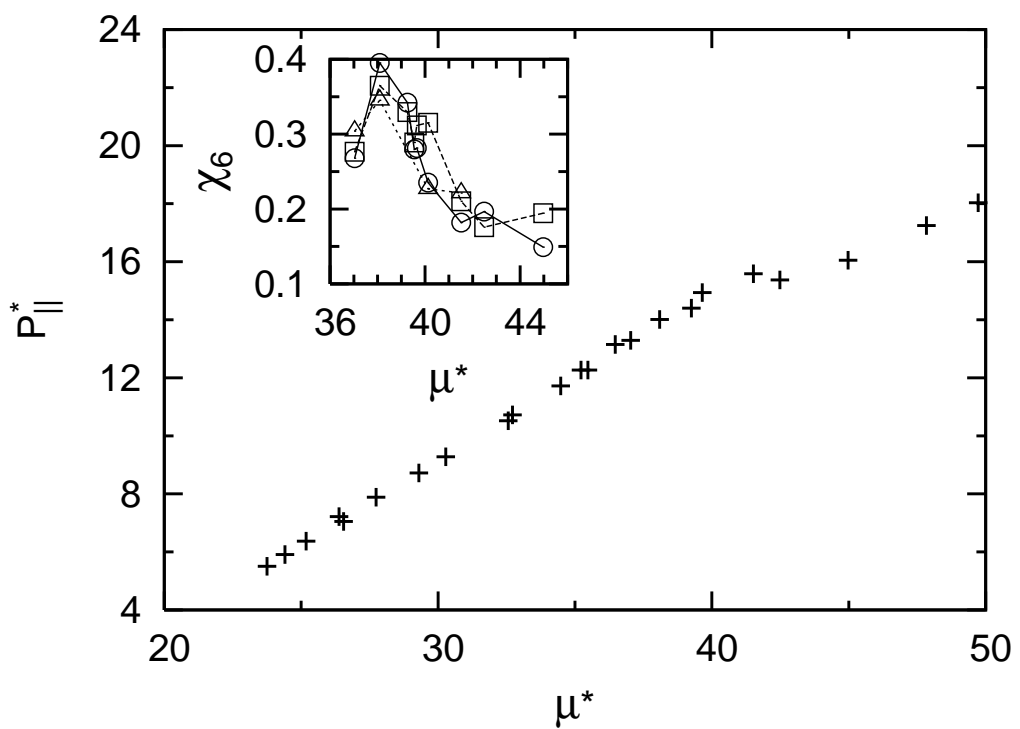


Figure 30: Lateral pressure as function of the chemical potential at $L_z = 2.9\sigma$. The inset shows the order parameter susceptibility χ_6 of the contact layer for $N \approx 500$ (circles), 1000 (squares) and 2000 (triangles).

state. The parallel pressure equals the negative free energy density $\omega_{||}$ in case of a homogeneous system which means here homogeneous in the plane (see sec. 3.6). Of course, this is not completely correct since on the scale of the particles there is a structure but on a larger scale, e. g. the simulation box, it can be considered as merely homogeneous. Further evidence is found by computing bond order susceptibilities χ_n (see eq. 111). These quantities are a measure for the fluctuations of the corresponding bond order parameter ψ_n which are supposed to increase in the vicinity of phase coexistence (see sec. 3.6). In the thermodynamic limit $N \rightarrow \infty$ they diverge for a second order transition at coexistence whereas for a first-order transition they keep finite, i. e. they do not depend on N [16]. The inset of fig. 30 shows χ_6 in a small μ range for different system sizes $N \approx 500, 1000$ and 2000 . A maximum is observed at $\mu^* \approx 38$ which does not increase with N . The small deviations are related to statistical errors. Furthermore, these strong fluctuations are located in the range of onsetting crystallization of fig. 27. From this observation one can observe that this onset of crystallization indicated by bond order parameters and the parallel pressure is related to a first-order transition with a coexistence point at $\mu^* \approx 38$.

Next, this system was investigated at a smaller wall separation $L_z = 2.2\sigma$. Following the results of fig. 26b it corresponds to a squared state at high chemical potentials. A typical in-plane correlation function at this L_z and $\mu^* = 41.52$ is shown in fig. 31 which is characterized by an additional peak emerging between the first and the second peak. Remind that the corresponding bulk state at the same chemical potential is fluid-like. The inset of the figure with the local density profile shows a smaller mean distance between the particle layers (distance of the peaks) compared to fig. 29a, i. e. the smaller wall distance presses the layers together. This explains that the particles cannot form a staggered hexagonal structure as for $L_z = 2.9\sigma$ which needs more space in the normal direction. For $L_z = 2.2\sigma$ the layers have to penetrate each other to fit between the walls. This is energetically favorable with a staggered squared structure due to the less dense in-plane packing. The bond order parameter ψ_4 indicates an onset of crystallization while increasing μ (see fig. 32). At small μ^* both ψ_4 and ψ_6 have similar values around 0.6, i. e. there are strong translational correlations yielding these rather high values of ψ_n but no preferred structure. It can be described as a "coexistence" of weak hexagonal and squared structure [109]. For $\mu^* \gtrsim 35$ this behavior changes and ψ_4 increases slowly up to values of about 0.8 – 0.9 whereas ψ_6 strongly decreases and remains small with $\psi_6 \approx 0.3$. This corresponds to a highly ordered (staggered) squared structure (see fig. 33). The chemical potential where the onset of crystallization occurs is somewhat smaller for $L_z = 2.2\sigma$ than for $L_z = 2.9\sigma$. This is expected for those wall separations

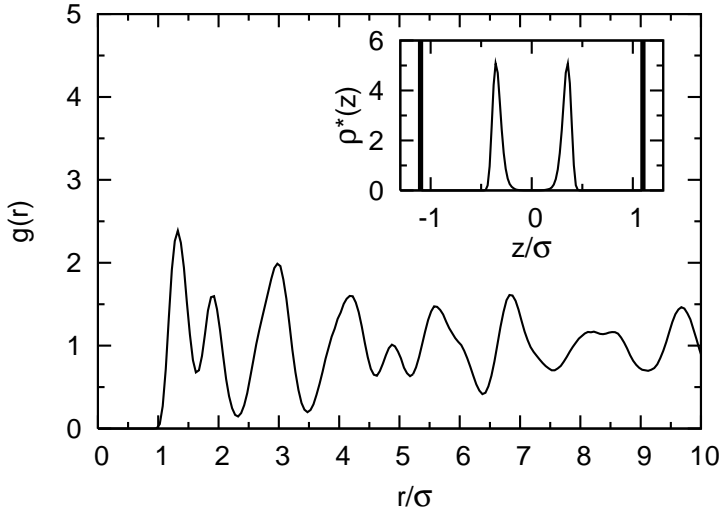


Figure 31: In-plane correlation function and density profile (inset) at $L_z = 2.2\sigma$ and $\mu^* = 41.52$ ($\kappa^* = 2.728$). The corresponding bulk correlation function is shown in fig. 29.

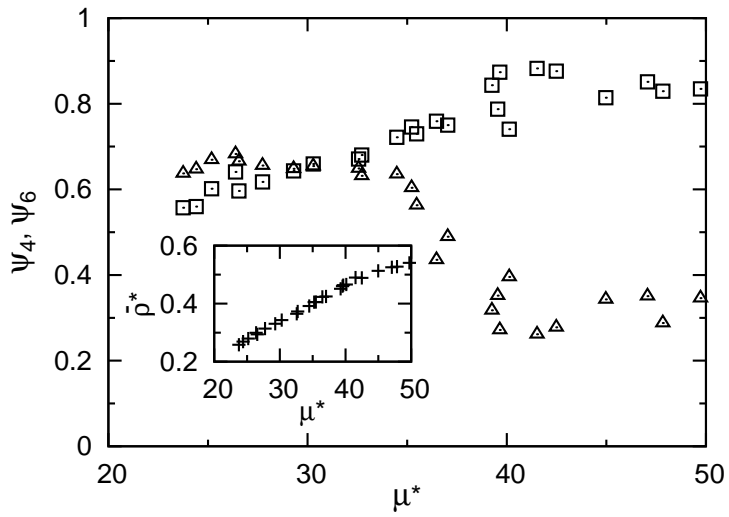


Figure 32: GCMC data for the order parameters ψ_6 (triangles) and ψ_4 (squares), and the average pore density (inset) as functions of μ^* at $L_z = 2.2\sigma$.

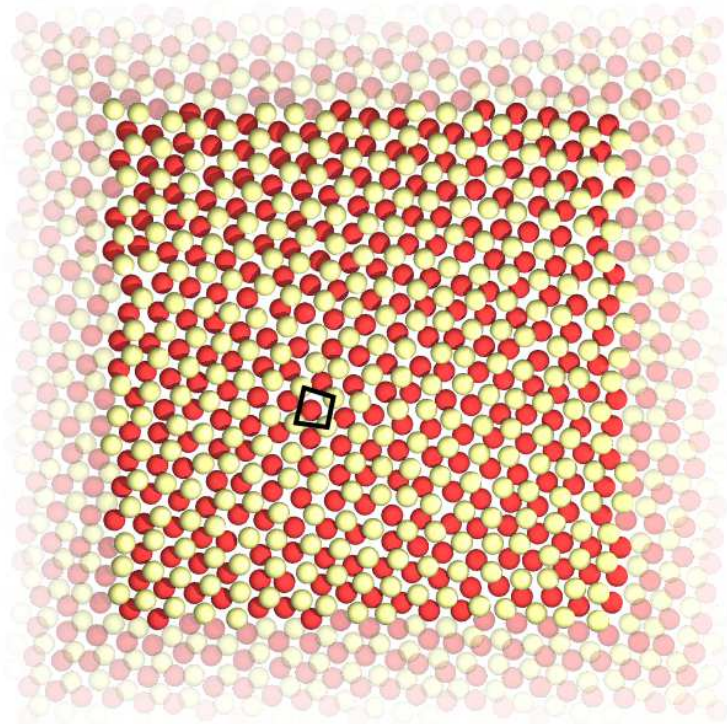


Figure 33: Snapshot (top view) of the "staggered-square" structure for $L_z = 2.2\sigma$ and $\mu^* = 41.52$. The different colored particles indicate the particle layers. The square indicates the arrangement of the nearest in-plane neighbors of a particle.

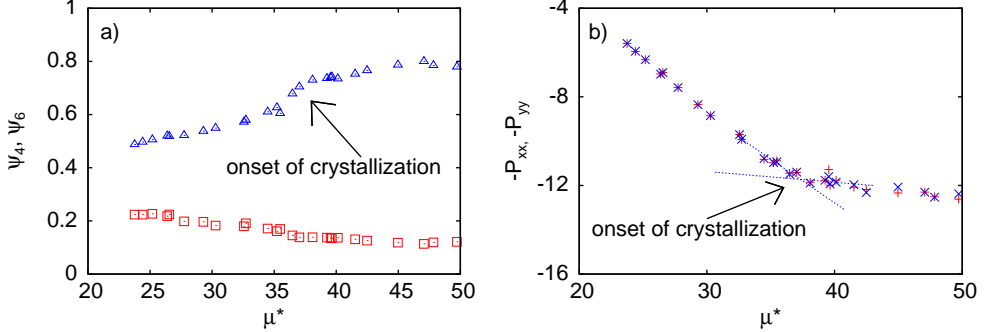


Figure 34: a) Bond order parameters ψ_6 (triangles) and ψ_4 (squares) as function of the chemical potential for a one-layer system at $L_z = 1.8\sigma$. b) In-plane pressure tensor components P_{xx} (plus) and P_{yy} (cross) as function of the chemical potential.

which are appropriate for crystal-like structures as concluded from fig. 26 (they are not in the distance regimes where the in-plane structure changes). For those wall separations one can say that smaller L_z promote the capillary freezing and therefore shift the chemical potential and the corresponding bulk density to smaller values. For L_z between these values the onset might shift to larger μ . This is also known from confined HS fluids [37].

Additionally, a monolayer system at $L_z = 1.8\sigma$ was computed showing an onset of crystallization from fluid to hexagonal order for increasing density as shown in fig. 27. This transition takes place at $\mu^* \approx 37.5$ plotted in fig. 34a. A look on the negative parallel pressure in fig. 34b reveals a more clear evidence of a phase transition than for the two-layer system in fig. 30. The slope of the curve changes abruptly at $\mu^* \approx 37.5$ indicating different compressibilities of the fluid and the solid phase. Assuming homogeneity in the plane parallel to the walls, the negative pressure equals the free energy density ω of the grand canonical system (see sec. 3.6). However, in case of a first-order transition, the solid phase is supposed to have a stronger slope of $\omega(\mu)$ than the fluid phase which we did not find. Thus, one must question the assumption of homogeneity in the plane for the solid phase which is characterized by long-range correlations.

Beyond the fluid-solid transition solid-solid transitions can be found for the confined charged colloids as well. These simulations are drawn out within the $NP_{||}L_zT$ ensemble (see sec. 4.4) since the high densities considered here are not accessible for GCMC. Here a wall separation of $L_z = 2.9\sigma$ is chosen. Upon increasing the external control parameter $P_{||}$ the mean pore density $\bar{\rho}$ monotonically increases (see fig. 35a). At $P_{||}^* \approx 33$ a metastable regime with

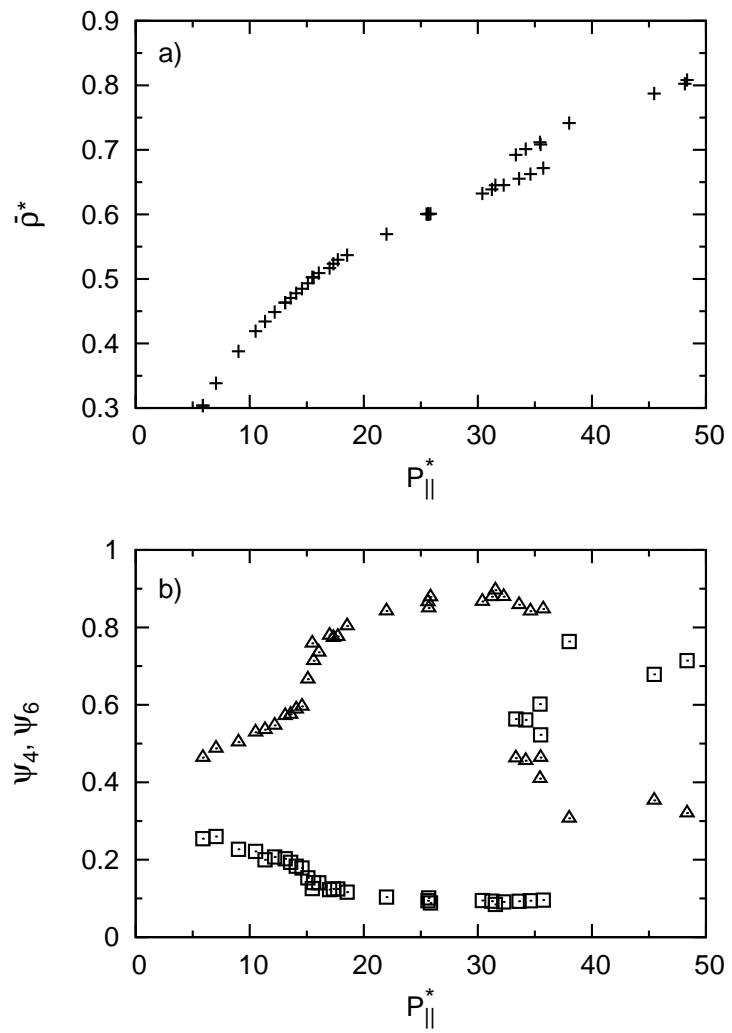


Figure 35: $NP_{\parallel}L_zT$ results for (a) the average pore density and (b) the bond order parameters ψ_6 (triangles) and ψ_4 (squares) as functions of the externally applied lateral pressure at $L_z = 2.9\sigma$.

two branches emerges. At $P_{\parallel}^* \approx 37$ the first branch becomes unstable and the second one stable. This "jumping" density clearly states the existence of a first order transition with a coexistence point within the metastable region. Taking a look at the in-plane structure in fig. 35b provides more details. Consistent with the GCMC results from fig. 27 ψ_6 strongly increases at $P_{\parallel}^* \approx 15$ yielding a solidification into a two-layer hexagonal state (2Δ) which reaches large values of $\psi_6 \approx 0.9$. The value of ψ_4 decreases monotonically. For $33 \lesssim P_{\parallel}^* \lesssim 37$ both bond order parameters jump yielding two branches which correspond to the metastable regime found in fig. 35a. On the emerging (metastable) branch ψ_4 becomes larger than ψ_6 although both values are rather small. For larger P_{\parallel} where the first branch becomes unstable ψ_4 jumps to large values of about 0.7 corresponding to a three-layer squared state ($3\square$). These findings give clear evidence that two solid states (hexagonal and squared) coexist in the parameter range considered. This first order transition is, physically spoken, driven by the fact that above a certain L_z it is energetically favorable to form three layers with smaller layer spacing. Although the hexagonal phase possesses a more efficient in-plane packing than the squared phase the two layers of 2Δ would yield large structural forces at such wall separations. A similar $2\Delta \rightarrow 3\square$ transition was also observed for HS systems confined between hard walls [37]. Comparing these results yields quantitative differences in the transition densities which are smaller in the presented results than for the HS system which might be founded by the longer range of DLVO repulsion. The wall separation where this transition is observed in fig. 35 is shifted to higher values as well compared to the HS system ($L_z = 2.3\sigma$) due to the different fluid-wall potential. Other intermediate structures as, e. g., prism structures [37] have not been found here at least at the considered separation of $L_z = 2.9\sigma$. However, the long-range character of the DLVO interaction (intermediate values of κ) might prohibit these complex structures [94, 86]. The rather small bond order values ψ_4 for the square-like structures in the metastable range (for small values of ψ_6) in fig. 35b might originate from strong fluctuations between the two states. Another reason for these moderate values even at large $P_{\parallel}^* \gtrsim 37$ could be a symmetry breaking. An example found for $P_{\parallel}^* = 48.21$ is shown in the snapshot fig. 36 where only one contact layer is depicted in the top view of the three-layer system. Two "domains" of squared order in this layer emerge which are distinguished just by a different orientation. The other layers exhibit the same domains as well yielding staggered-squared domains. These structures have a long life-time, i. e. they do not vanish within 50,000 MC cycles. The boundaries between the domains are characterized by defects which might be the reason for the lower values of ψ_4 . If this is the case ψ_4 should show a system size dependence since the length of the domain

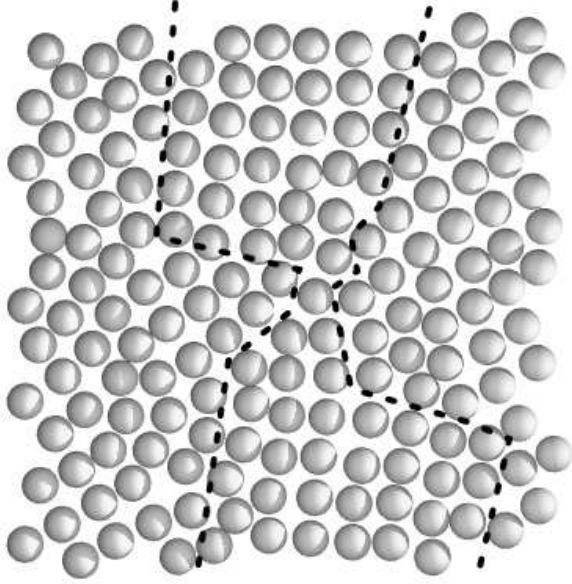


Figure 36: Snapshot (top view) of the in-plane structure of one layer in the high density ($3\bar{\square}$) phase at $L_z = 2.9\sigma$ and $P_{\parallel}^* = 48.21$. The dashed lines indicate the domain boundaries.

boundaries grows with the square root of N whereas the average of the local bond order parameter (see eq. (110)) goes over all N particles.

6.4 Surface-charge-induced freezing

In order to complete the results of sec. 5.4, which uses the modified fluid-wall interaction for charged walls introduced in sec. 2.6, we explore in this section density parameter ranges for varying wall charges concerning in-plane ordering and fluid-solid phase transitions. The systems simulated with GCMC are equilibrated using $(5 - 50) \times 10^4$ MC steps and relevant physical quantities are collected using $(1 - 10) \times 10^5$ MC steps for different particle numbers $N = 500, 1000$ and 2000 .

Since we expect an impact of the surface charges on the in-plane structure of the suspension we consider at first bond order parameters for varying wall separations to determine interesting parameter ranges. In fig. 37 the bond order parameters ψ_6 and ψ_8 are plotted as function of L_z for different wall charges at the fixed bulk density $\rho_b^* = 0.61$. The alternation of $\psi_n(L_z)$ known for uncharged walls (see sec. 6.2) also occurs for charged surfaces. The equilibrium state changes from non-ordered to ordered structures with a period of about the particle diameter σ while increasing L_z . Replacing these

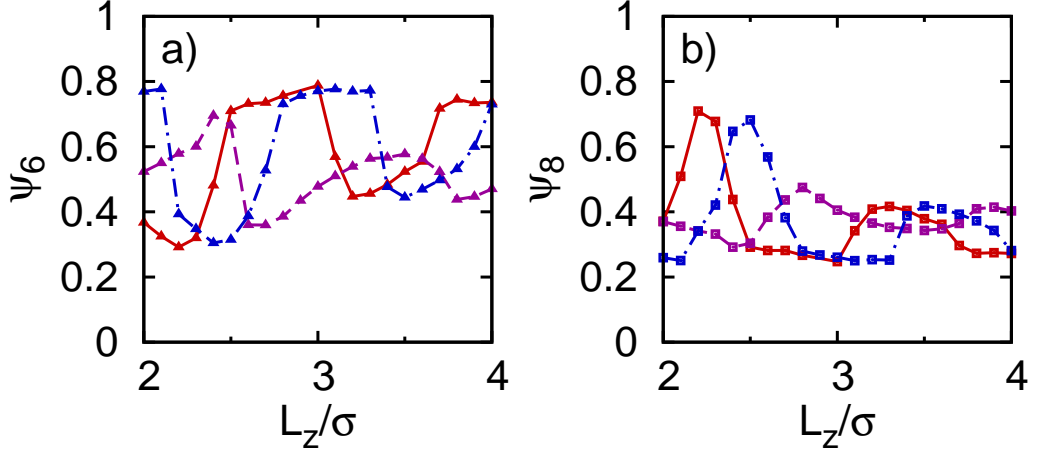


Figure 37: Bond order parameters a) ψ_6 and b) ψ_8 as function of the wall separation L_z at $\rho_b^* = 0.61$ for uncharged (red solid line), silica (purple dashed line), and mica (blue dot-dashed line) walls. The triangles and squares are the simulation data, and the lines are a guide to the eye.

walls by charged silica walls yields two effects. On one hand the maxima and minima of the alternation are shifted towards larger densities and on the other hand the amplitudes decrease. Both effects are consistent with the qualitative behavior of the fluid-wall potential (see sec. 2.6) and originate from an effective narrowing of the slit pore and softening of the layers with increasing repulsion. Replacing the silica walls by mica walls the opposite effect can be seen. The non-monotonic behavior of the potential is reflected by these results since the silica walls with a large repulsion exhibit a bigger phase shift and stronger damping of the amplitudes than the mica walls with a smaller repulsion. This is observed for both the hexagonal (see fig. 37a) and the squared structures (see fig. 37b). Taking a closer look at the wall separation $L_z = 2.4\sigma$ shows that the in-plane order is crucially influenced by the wall charge. The value of ψ_6 changes from 0.5 (uncharged) via 0.7 (silica) to 0.3 (mica) whereas ψ_8 changes from 0.45 (uncharged) via 0.3 (silica) to 0.65 (mica). In other words, silica walls show a significant hexagonal and mica walls a squared order whereas uncharged walls seem to be inappropriate for ordering at the considered L_z . The corresponding in-plane correlation functions $g_{||}(r)$ in fig. 38a underline these results. For the uncharged case $g_{||}(r)$ behaves almost fluid-like. The charged walls yield a slower (non-exponential) decay of the correlations and changes of the maxima typical for hexagonal and squared structures emerge. Especially, the squared structure (mica) possesses an additional peak between the first and the second one. Results for

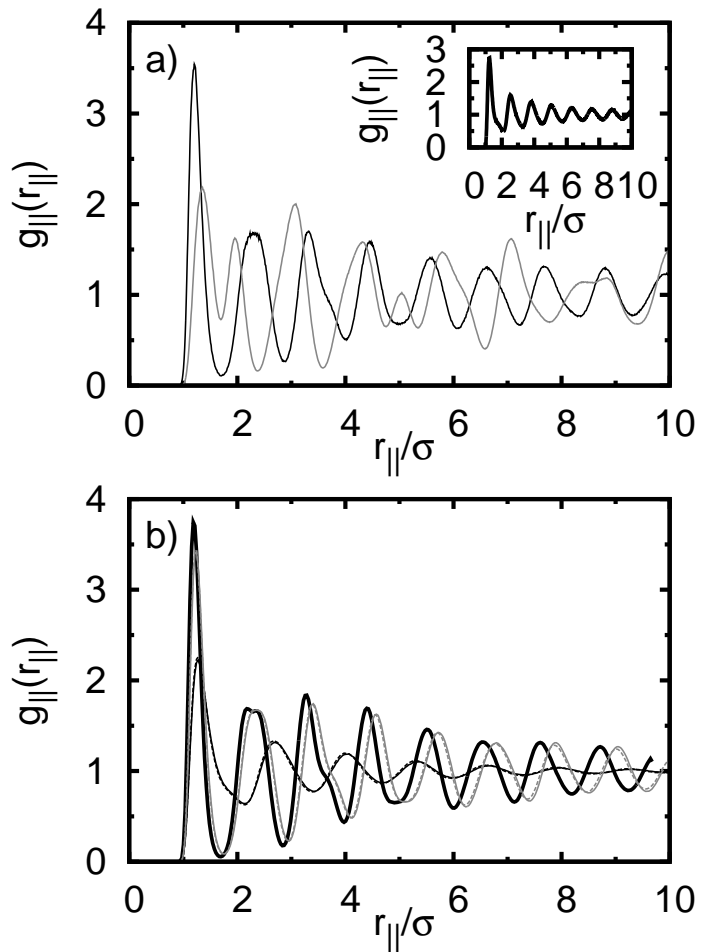


Figure 38: a) In-plane correlation functions for $L_z = 2.4\sigma$ using the wall types uncharged (inset, thick black solid line), silica (thin black solid line) and mica (thin gray solid line). b) In-plane correlation functions for $L_z = 2.9\sigma$ with wall types as in (a). Included are results involving the wall-counterion contribution in the fluid-fluid interaction for silica (thin black dashed line) and mica (thin gray dashed line).

$L_z = 2.9\sigma$ are shown in fig. 38b where the behavior for uncharged walls does not change and both charged wall types are related to hexagonal structures with the emerging splitting of the second peak.

Using the previous considerations it is interesting to ask for the impact of the wall charge on the transition behavior induced by the density or chemical potential of the suspension. We expect that the surface charges influence the onset of crystallization investigated in sec. 6.3. The results are summarized in fig. 39. For silica walls a slow increase of ψ_6 with increasing chemical potential μ^* is observed in fig. 39a until $\mu^* \approx 40.5$. For larger μ^* a stronger increase of the order yielding values above 0.6 occurs which we relate to an onset of crystallization. The other wall types exhibit constant or decreasing small values of ψ_6 . For mica walls ψ_8 in fig. 39b shows a strong increase at $\mu^* \approx 39.5$ also yielding values above 0.6. It is interesting to note that the onset of crystallization for mica walls begins at smaller chemical potentials, i. e. at smaller densities, than for silica walls. This reflects the stronger softening by the repulsive silica walls. The snapshot in fig. 39e shows the top view at a chemical potential of $\mu^* = 41.52$ for silica walls. Consistent with the finding that $\psi_6 \approx 0.7$ the system forms one particle layer with a (non-perfect) hexagonal structure marked by the hexagon. The snapshot in fig. 39f shows the same for mica walls forming a two-layer system with a staggered squared structure.

The structural changes induced by the particle density showed in figs. 39a and b give evidence for phase transitions which we confirm by computing the corresponding bond order susceptibilities $\chi_n = N(\langle \psi_n^2 \rangle - \langle \psi_n \rangle^2)$. These fluctuations increase near a phase transition and become maximal at the coexistence point. As shown in fig. 39c χ_6 exhibits a maximum for silica walls at the chemical potential $\mu^* = 41.5$ where ψ_6 increases stronger. Mica walls yield a maximum in χ_8 at $\mu^* = 39.5$ where the strong increase of ψ_8 occurs. From these findings we can conclude that the onset of ordering correspond to fluid-solid phase transitions. It is interesting that the parameter χ_8 in fig. 39d also shows a maximum for silica walls at the same $\mu^* = 41.5$ although the corresponding value of ψ_8 remains small for this wall type. This unexpected maximum is related to strong fluctuations while the hexagonal order emerges.

In order to better understand these unexpected strong fluctuations we take a closer look on the bond order parameters. Therefore we plotted the development of the non-averaged value of ψ_6 with MC “time” for $\mu^* = 41.52$ and silica walls shown in fig. 40a. The spontaneous bond order ψ_6^{act} exhibits not only the expected fluctuations on a short scale but also long scale fluctuations, i. e., the system “jumps” between two coexisting phases which is typical for first-order transitions. Although the free energy barrier between a fluid and a solid state is large the fluctuations are strong enough to over-

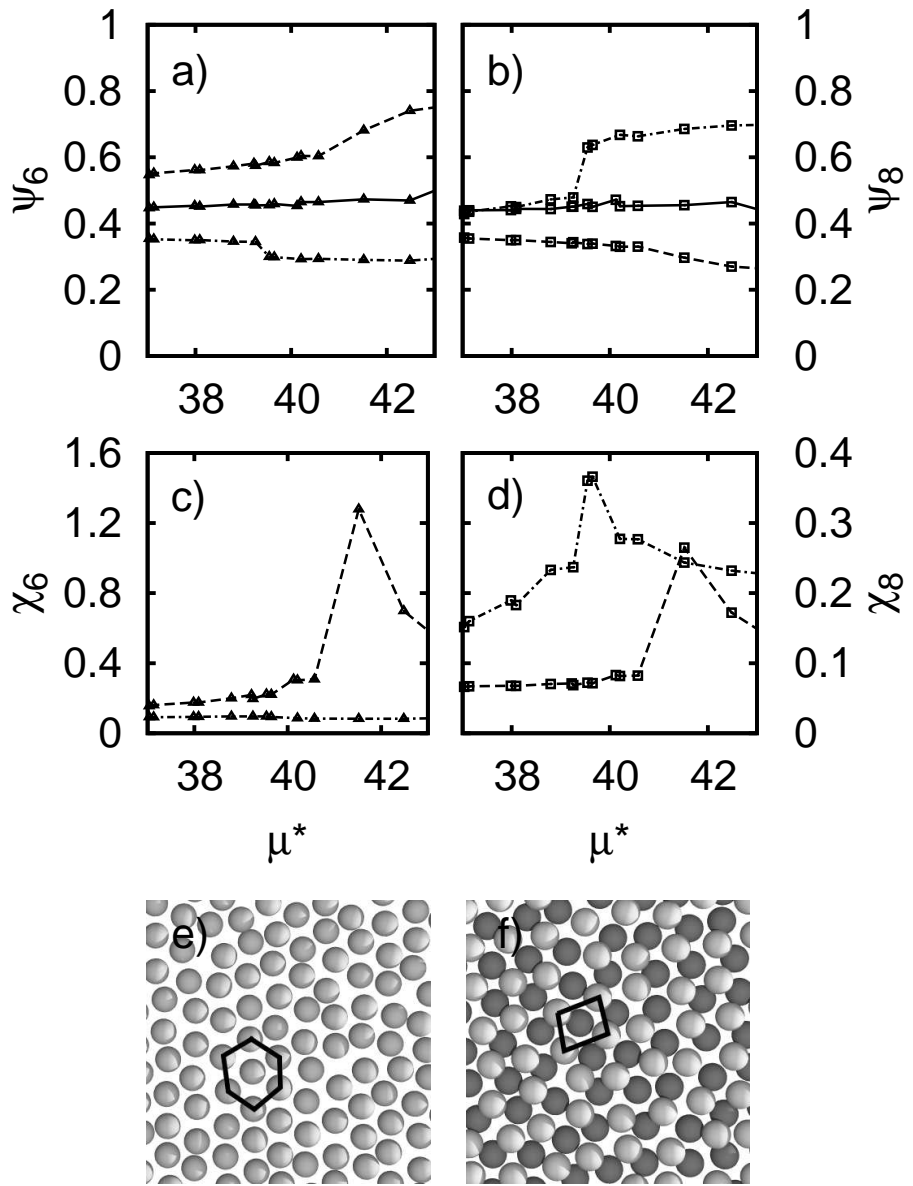


Figure 39: Bond angle order parameters (a) ψ_6 and (b) ψ_8 with corresponding susceptibilities (c) χ_6 and (d) χ_8 as function of μ^* for uncharged (solid line), silica (dashed line), and mica (dot-dashed) walls with a separation of $L_z = 2.4\sigma$. The triangles and the squares are simulation results, whereas the lines are a guide to the eye. Corresponding top-view snapshots for $\mu^* = 41.52$ and (e) silica walls (hexagonal phase) and (f) mica walls (squared phase).

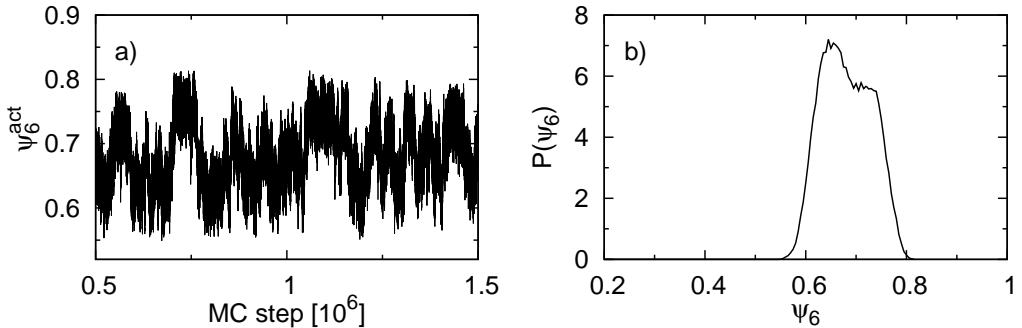


Figure 40: System at $L_z = 2.4\sigma$ and $\rho_b^* = 0.61$ ($\mu^* = 41.52$) using silica walls. a) Actual non-averaged values of ψ_6 during the MC simulation in the averaging interval. b) Corresponding distribution $P(\psi_6)$ of the bond angle order ψ_6 .

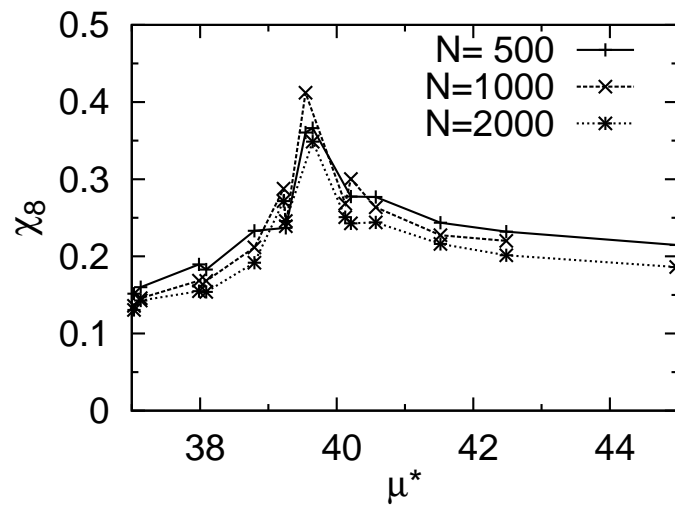


Figure 41: System size dependence of the bond order fluctuations χ_8 as function of the chemical potential μ^* for mica surfaces at $L_z = 2.4\sigma$, varying chemical potentials, and different particle numbers $N = 500, 1000, 2000$. The symbols are the simulation data and the lines are a guide to the eye.

come this barrier. As known from vapor-liquid transitions the histogram of the fluctuating quantity reveals a double-peak structure near the coexistence point which is shown in fig. 40b [123, 39]. Both peaks are overlapping in this case since the difference between the mean densities of the two phases is small. At the coexistence point the peaks are supposed to cover the same area which cannot be measured for overlapping peaks. This also explains the large fluctuations at $\mu^* = 41.52$ and 42.48 in fig. 39c and d. First-order phase transitions are characterized by an independence of χ_n on the system size in opposite to second-order transitions where the fluctuations diverge with increasing particle number at coexistence [16]. As an example fig. 41 shows χ_8 for mica walls in the chemical potential range of the emerging squared phase using particle numbers $N = 500, 1000$ and 2000 . At $\mu^* = 39.5$ the susceptibilities exhibit a maximum indicating the phase transition which is consistent with the findings from fig. 39b. Since the maximum does not diverge for increasing N we conclude that this phase transition is of first order. The small deviations are expected to originate from statistical errors.

These density-induced freezing transitions are highly sensitive on the wall charge. Therefore it is worth to consider wall charge driven transitions in more detail by using the wall charge (or surface potential ψ_S) as a continuous parameter at fixed chemical potential, whereas in the previous investigation we concentrated on three wall types varying μ . As shown in figs. 42a and b we found such charge-induced transitions for $L_z = 2.4\sigma$ and $\rho_b^* = 0.61$. Different changes occur in the suspension while increasing ψ_S concerning the particle layering and the in-plane structure. The first effect is characterized by an abrupt change from a two-layer to a one-layer system at $|\psi_S| \approx 25mV$. At $|\psi_S| \approx 125mV$ the system goes back to a two-layer system. This behavior reflects the non-monotonicity of the fluid-wall interaction (see eq. (2.6)). The second effect concerns the in-plane structure. Starting with uncharged walls ($\psi_S = 0$) both order parameters ψ_6 and ψ_8 have small values around 0.45. Increasing $|\psi_S|$ up to $10mV$ yields a first maximum of ψ_8 with a value of about 0.65 which corresponds to a two-layer squared structure. At a slightly smaller $|\psi_S|$ the corresponding χ_8 exhibits a maximum indicating a phase transition between the fluid and the crystal-like (squared) state. For larger wall charges the system again becomes fluid-like (one-layer system) accompanied by an abrupt change of ψ_6 and ψ_8 where the latter becomes small. The value of ψ_6 , which is at first slightly below 0.6, exhibits a strong increase at $|\psi_S| \approx 80mV$ with values of about 0.8. At this point χ_6 shows a maximum indicating the fluid-to-hexagonal transition. Increasing $|\psi_S|$ the value of ψ_6 drops down to small values (transition to two-layer system) and ψ_8 increases up to values of about 0.7. At $|\psi_S| \approx 150mV$ the corresponding χ_8 shows a maximum related to this fluid-to-squared transition. From the behavior of ψ_6 and ψ_8

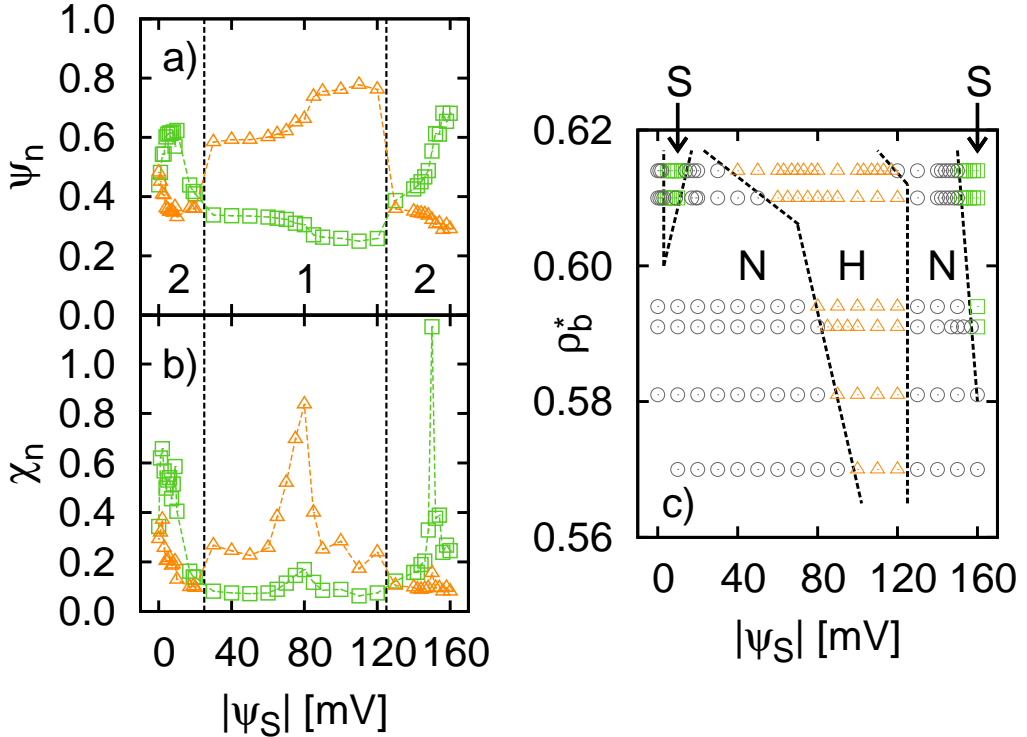


Figure 42: Influence of surface charges (surface potential ψ_S) on the in-plane order for $L_z = 2.4\sigma$. (a) Bond order parameters ψ_8 (green squares) and ψ_6 (orange triangles) as function of ψ_S . The number of layers are indicated by the vertical dashed lines and the numbers. (b) Corresponding bond order susceptibilities χ_8 (green squares) and χ_6 (orange triangles). (c) Phase diagram as function of ψ_S and bulk density ρ_b^* showing squared phases (green squares, 'S') with $\psi_8 \geq 0.6$, hexagonal phases (orange triangles, 'H') with $\psi_6 \geq 0.6$, and non-ordered phases (gray circles, 'N'). The dashed lines are a schematic representation of the phase boundaries.

one can see that the fluid-wall interaction is not a symmetric narrowing and broadening of the slit pore. Values of $|\psi_S| > 80mV$ promote crystal-like structures indicated by the larger bond order parameters. Furthermore, at $|\psi_S| \approx 125mV$ the system “jumps” from a two-layer system into a hexagonal one-layer system whereas at $|\psi_S| \approx 25mV$ the system “jumps” into a fluid one-layer system.

To get an overview of the behavior of the considered system a phase diagram is plotted in fig. 42c with wall charges $|\psi_S|$ between $0mV$ and $160mV$ and bulk densities ρ_b^* between 0.57 and 0.614 also containing the results of figs. 42a and b. Phase regions corresponding to non-ordered (N), squared (S) and hexagonal (H) phases are separated by dashed lines. The diagram shows nicely the reentrant freezing into a hexagonal structure. The crystal-like phase regions S and H broaden with increasing bulk density which is related to the density-induced onset of crystallization discussed before. The squared phases at small wall charges vanish for $\rho_b^* < 0.6$. For bulk densities above the considered range we expect that the non-ordered phases will vanish completely and solid-solid phase boundaries might be observed. The reentrant freezing observed reflects the non-monotonic behavior of the fluid-wall interaction (see eq. (2.6)) combined with the chosen L_z . As mentioned above it promotes freezing for larger wall charges $|\psi_S| > 80mV$ reflecting that the non-monotonicity is not symmetric in ψ_S . The phase boundaries are determined by defining a structure as crystal-like if the bond order $\psi_n \gtrsim 0.6$. This is motivated by the fact that ψ_n in fig. 42a is about 0.6 where the corresponding χ_n in fig. 42b exhibits a maximum, i. e., the fluid-solid transition is characterized by a threshold of about 0.6. However, a qualitative change of the phase diagram using a different definition of the threshold is not expected. Note, that other complex structures as buckled, rhombic or prism phases in the considered parameter range which are known from HS systems [37] or ground-state Coulombic systems [95] have not been found in the considered system. The relatively small screening strength κ and the finite temperature might inhibit these structures. Indeed, in a recent ground-state study [94] complex structures have been only observed for larger κ . An investigation of Yukawa bilayers using MC at finite temperature [86] found staggered phases without buckling as well. Buckling as an example is supposed to emerge between a one-layer and a two-layer system but in this parameter range (see fig. 42a) the suspension investigated in this work behaves fluid-like.

7 Binary mixtures

The present chapter focuses on charged particles with two different diameters accompanied by different surface charges. The impact of different particle sizes described via DLVO interaction was studied in a previous study discussed in sec. 5.3. The ratio of diameters considered is far from one, i. e. the study takes a look on strongly asymmetric mixtures in order to investigate structural crossover. This effect is characterized by a change in the asymptotic wavelength of the correlation functions while changing the densities of the mixture components, i. e. the composition of the mixture. It was found theoretically earlier for HS systems [47, 48] and non-additive HS systems [61] in bulk. Furthermore it was observed in confinement for HS mixtures [48] as well as in 2D systems [10]. In experiment it was seen via confocal microscopy in [10]. This effect concerns the wavelength of the correlations in the system which is, at moderate or large densities, characterized by the particle diameter. In the binary mixture there are two particle sizes where one of them dominates the correlations depending on the composition of the mixture. The particle species used in this chapter are summarized in table 5.

A second issue considered in this chapter concerns the adsorption of a mixture confined to a slit-pore and the resulting structure formation perpendicular to the walls. It is found that the components of the mixture influence each other depending on system parameters as size ratio, wall separation, and density. As a result the composition deviates from bulk behavior and the layering of the species must be distinguished from that in monodisperse systems. The adsorption process and the structuring in confined mixed suspensions have been investigated for LJ particles [23], non-polar and polar HS particles [19], as well as for one planar wall concerning the wetting of point Yukawa mixtures [60] and the adsorption of a colloid-polymer mixture [30]. The effect of a confining soft-sphere matrix on a supercooled binary mixture was investigated via MD and mode coupling theory (MCT) in [40].

| Type i | σ_i^* | Z_i |
|----------|--------------|-------|
| A | 1.0 | 35 |
| B | 0.5 | 10 |
| C | 0.62 | 13 |

Table 5: Particle species used for the binary mixtures with diameters $\sigma_i^* = \sigma_i/\sigma$, where $\sigma = 26\text{nm}$, and valencies Z_i . The valencies are determined via the Grahame equation (see eq. (7)) and ionic strength $I = 10^{-5}\text{mol l}^{-1}$.

7.1 Structural crossover in bulk systems

Employing canonical MC simulations with 2500 particles a binary mixture in bulk has been studied. The size ratio is $q = \sigma_B/\sigma_A = 0.5$ with $\sigma_B^* = 0.5$ and $\sigma_A^* = 1.0$. The diameters are scaled by the diameter $\sigma = 26\text{nm}$ used in sec. 5. Following the Grahame equation (eq. (7)) the species have charges $Z_A = 35$ and $Z_B = 10$, respectively, and the salt concentration is set to $I = 10^{-5}\text{mol l}^{-1}$ (see table 5). Simulating these systems the challenge is to handle a large number of small particles depending on the given volume fractions η_A and η_B . In the case $\eta_B > \eta_A$ the total particle number N has to be large. Otherwise there are too few large particles in the ensemble resulting in bad statistics. The considered surface charges of the colloids yield moderate screening strengths $\kappa^* > 1.0$.

The structural crossover in binary mixtures is characterized by a change of the asymptotic wavelengths of the pair correlation functions g_{ij} where i and j are the particle species. According to ref. [47] OZ theory (see sec. 3.5) predicts that the wavelengths λ_{AA} , λ_{AB} and λ_{BB} are equal in the asymptotic range, i. e. the internal structure of the suspension is in the asymptotic range only determined by one of the species depending on the composition of the mixture. In ref. [47] DFT calculations revealed that this behavior is observed at intermediate distances as well. Taking many large particles A the wavelength λ_b is more or less in the order of σ_A , for many small particles B it is of the order of σ_B as found for HS systems [48]. Note, that at small volume fractions η_A the wavelengths λ_{ij} rather obey the power-law behavior $\lambda_{ij}^* = a\phi^{-b}$ than the particle size [74]. In the ideal case it is $b = 1/3$.

Fig. 43 shows the results of the wavelengths for the considered charged particle mixture. One observes that all three wavelengths are within statistical errors equal. This remarkable observation verifies the results of ref. [47]. The particle diameters of A and B are drawn as gray planes. For small η_B the value of $\lambda_{ij}^* \gtrsim 1.0$, i. e. the inner structure of the system is determined by the big particles but shows a significant dependence on η_A for small densities. For increasing η_B the value of λ_{ij}^* drops at $\eta_B \approx 0.1$ bellow 1.0 indicating a *structural crossover* and tends towards σ_B where the inner structure is characterized by the small particles. At large η_B the wavelength is about σ_B as found for HSs [48, 61]. This crossover region is expected to extend to larger η_B at large η_A , i. e. the regime where the system is characterized by σ_B should exhibit an increase of λ_b towards σ_A upon increasing η_A . Simulations are under way. This region exhibits a small decrease of λ_b which is related to interference effects where two wavelengths characterize the asymptotic behavior. However, this is expected at a certain point where the two leading order poles in the OZ result (see sec. 3.5) equal each other and yield these

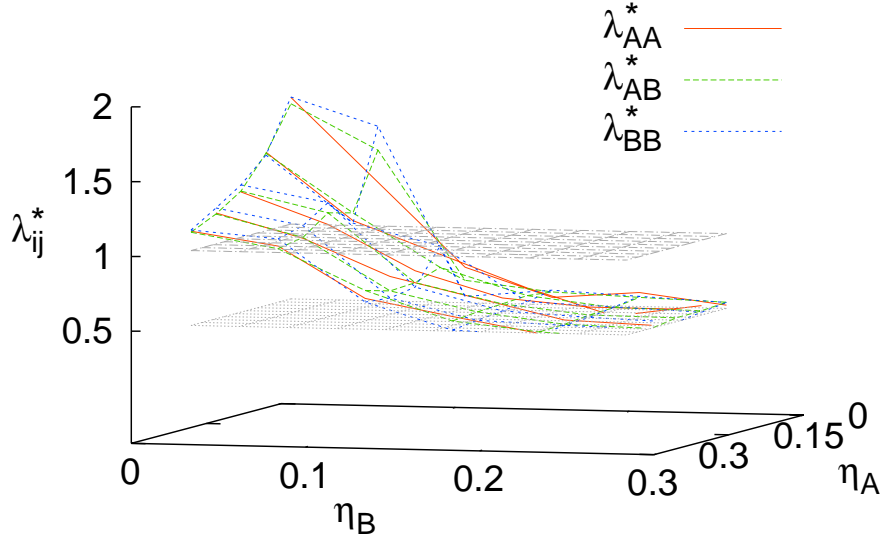


Figure 43: Reduced wavelengths λ_{ij}^* of the bulk pair correlation functions g_{AA} (red), g_{AB} (green), and g_{BB} (blue) as function of the volume fractions of big (η_A) and small particles (η_B). The gray planes mark the particle diameters $\sigma_A^* = 1.0$ (upper plane) and $\sigma_B^* = 0.5$ (lower plane).

interferences even at large distances. It is important to note that the determination of λ_b via eq. (145) is not accurate since the correlations decay fast for the volume fractions considered, i. e. the extraction of the characteristic lengths is done at a moderate distance. To observe a discontinuous jump in λ_b it would be necessary to consider $r \rightarrow \infty$ which is not possible within numerical MC simulations. Three examples for the correlation functions g_{ij} and the corresponding fit functions eq. (145) at different volume fractions η_B and fixed $\eta_A = 0.25$ are shown in figs. 44-46. Additionally, $\ln(rh(r))$ is plotted with the fit function which shows more clearly the wavelength characterized by the poles. In fig. 44 the results for a small value of $\eta_B = 0.02$ are plotted where the wavelengths are slightly above 1.0. Fig. 45 is for $\eta_B = 0.12$ within the crossover region showing the interferences in the correlations in the considered distance range r . In the spirit of pole analysis (see sec. 3.5) the second order pole becomes important in this regime and should be involved in the fitting procedure. However, the MC simulations employed here

are not precise enough especially in the asymptotic range (large distances). An analysis including two leading poles was done as well but did not yield clear results. Using DFT it is possible to determine a more accurate value of η_B where both poles possess the same decay, i. e. where the asymptotic behavior is characterized by both poles. At other volume fractions one of the poles dominate the other. This was done in [48] for a HS system using the Percus-Yevick approximation for the direct correlation function. At a large value $\eta_B = 0.27$ shown in fig. 46 the wavelength is about 0.5, i. e. the other pole corresponding to the small particles dominates the system. From the logarithmic plots it becomes clear that the MC results lack from inaccuracy concerning the asymptotic range and the choice of the fitting range might not be appropriate. Within these limits the assumption, that all λ_{ij} are equal, is verified by the results in figs. 44-46. However, the most accurate results in the asymptotic range are obtained for the correlation functions corresponding to the species characterizing the dominant wavelength. In other words, in fig. 44 where $\lambda_b \sim \sigma_A$ the function $g_{AA}(r)$ is more accurate than $g_{AB}(r)$ or $g_{BB}(r)$, whereas for fig. 46 with $\lambda_b \sim \sigma_B$ the function $g_{BB}(r)$ yields better results. In fig. 47, which is the projection of fig. 43 onto the η_B - λ_b plane, one can see for λ_{AA} more clearly the crossover for different values of η_A . The wavelength drops below σ_A at $\eta_B \approx 0.75$ and reaches σ_B at $\eta_B \approx 0.2$. For smaller volume fractions $\eta_B \lesssim 0.75$ the value of λ_b^* is greater than 1.0 and depends on η_A which is in contrast to the findings in [48] for HS. However, values of $\eta_B < 0.75$ have not been studied in detail in [48]. Comparing their results with the results of fig. 47 the crossover takes place at a similar volume fraction, e. g. $\eta_A = 0.1$ and $\eta_B = 0.125$ in [48]. On the other hand, at $\eta_B = 0.1$ the results in fig. 47 already exhibit a value of $\lambda_b^* < 1.0$ whereas in [48] still $\lambda_b \sim \sigma_A$. This might be due to the inaccuracy of the MC simulations at large distances. Furthermore, for $\eta_A \rightarrow 0$ the values $\lambda_b^*(\eta_B)$ are expected to show a power-law behavior for small η_B as known from monodisperse suspensions (see secs. 5.2 and 5.3) [74, 75]. There the characteristic length is related to the interparticle distance, i. e. to the inverse cubic root of the density (or volume fraction). In other words, if there are only a few small particles the mixture behaves similar to the monodisperse system which can be considered as a limit case. Indeed, for the smallest $\eta_A = 0.05$ considered the data possess a behavior similar to power law $\lambda_b^* = a\eta_B^{-b}$ within numerical errors but the exponent $b \approx 0.5$ deviates from the expected value 1/3. Note, that η_A considered is not zero, and the determination of λ_b from the correlation functions is more erroneous for mixtures than for monodisperse systems. The same results are plotted in fig. 48 as function of η_A . For small values $\eta_B \lesssim 0.05$ the wavelength again exhibits clearly a power-law decay $\lambda_b^* = a\eta_A^{-b}$ with an exponent $b \approx 1/3$. Increasing the number of small par-

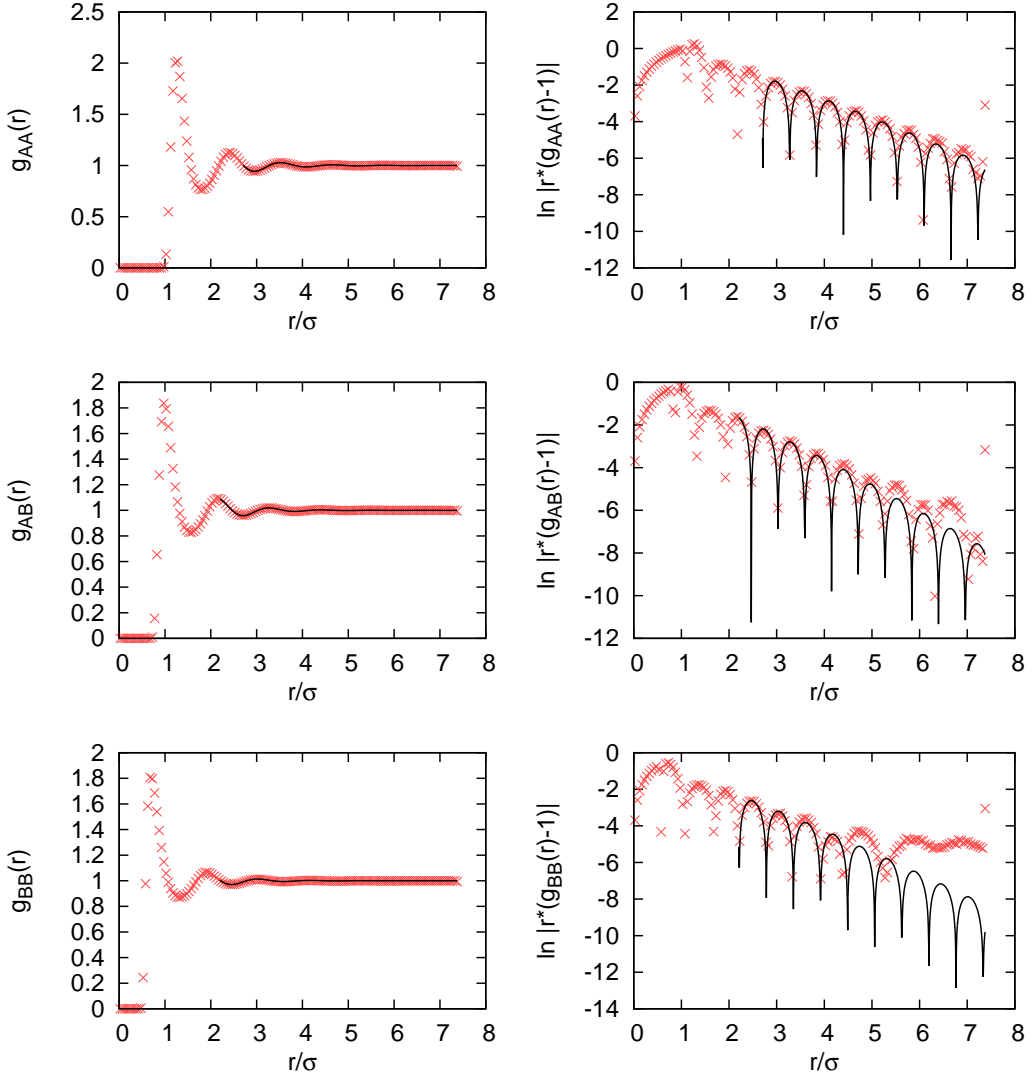


Figure 44: Pole analysis of the bulk correlation functions g_{ij} at $\eta_A = 0.25$ and $\eta_B = 0.02$.

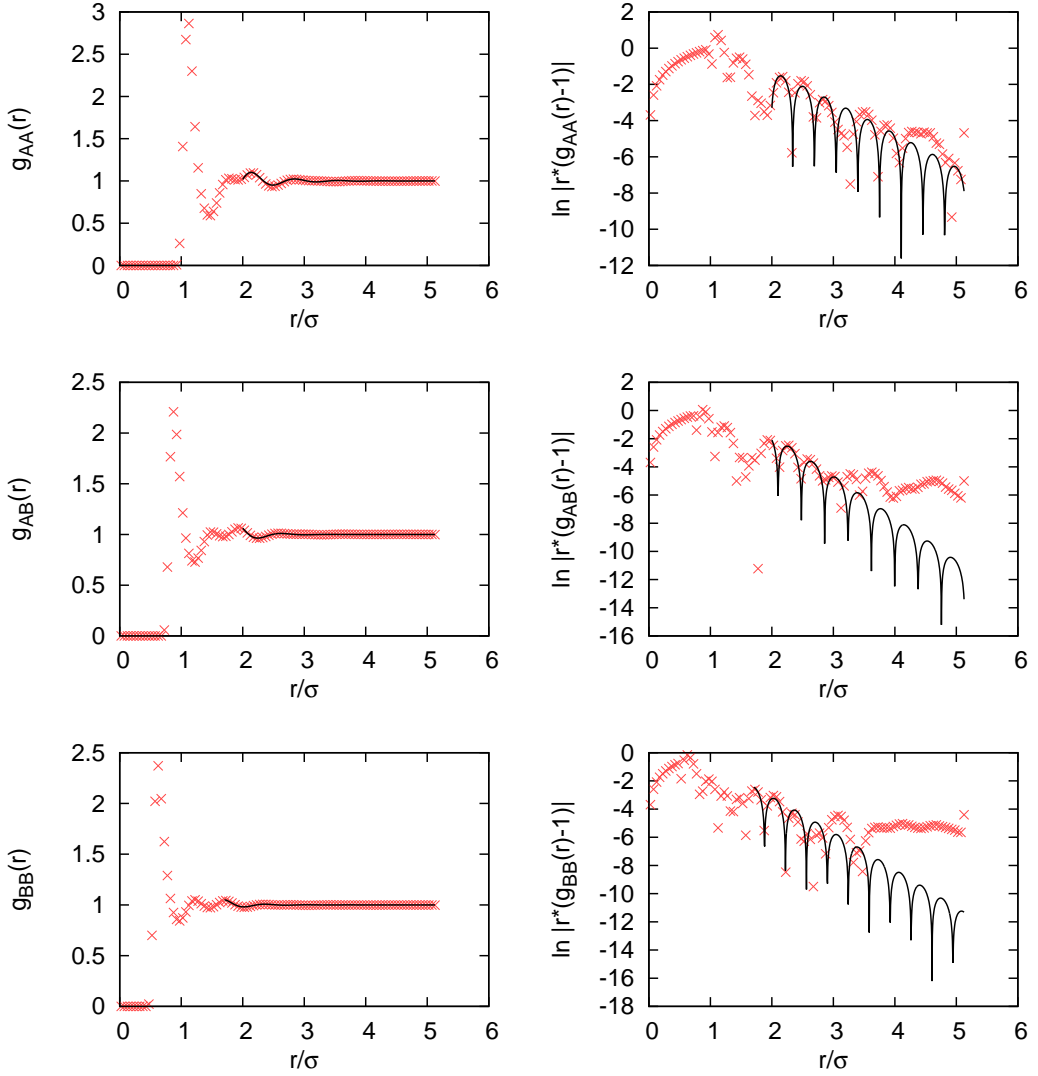


Figure 45: Pole analysis of the bulk correlation functions g_{ij} at $\eta_A = 0.25$ and $\eta_B = 0.12$.

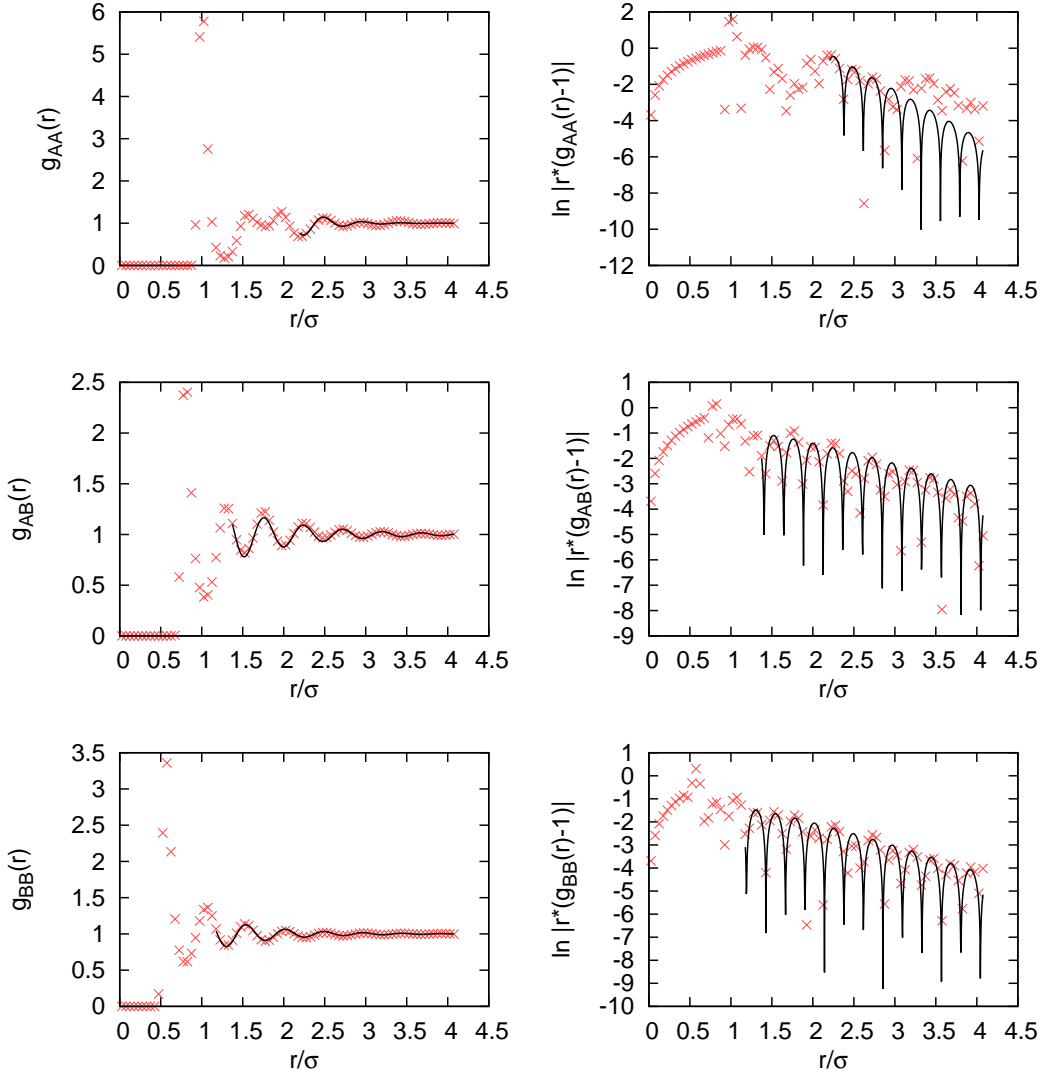


Figure 46: Pole analysis of the bulk correlation functions g_{ij} at $\eta_A = 0.25$ and $\eta_B = 0.27$.

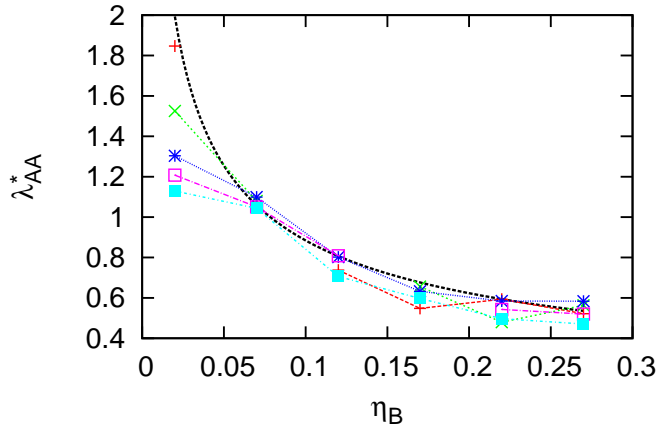


Figure 47: Reduced wavelength λ_{AA}^* as function of η_B for different volume fractions of big particles $\eta_A = 0.05$ (red), $\eta_A = 0.1$ (green), $\eta_A = 0.15$ (blue), $\eta_A = 0.2$ (purple), and $\eta_A = 0.25$ (turquoise). The lines connecting the data points are a guide to the eye. The data for $\eta_A = 0.05$ obey a behavior similar to power law decay with exponent $b \approx 0.5$ (black line).

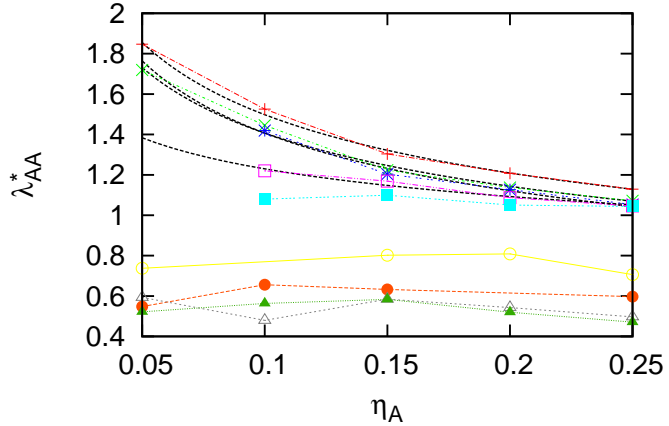


Figure 48: Reduced wavelength λ_{AA}^* as function of η_A for different volume fractions of small particles $\eta_B = 0.02$ (red), $\eta_B = 0.04$ (green), $\eta_B = 0.05$ (blue), $\eta_B = 0.06$ (purple), $\eta_B = 0.07$ (turquoise), $\eta_B = 0.12$ (yellow), $\eta_B = 0.17$ (orange), $\eta_B = 0.22$ (gray), and $\eta_B = 0.27$ (dark green). The dashed black lines are power-law functions $\lambda_{AA}^* = a\eta_A^{-b}$ fitted to the data points of $\eta_B = 0.02, 0.04, 0.05, 0.06$ with exponents $b = 0.31, 0.3, 0.33$, and 0.17 , respectively.

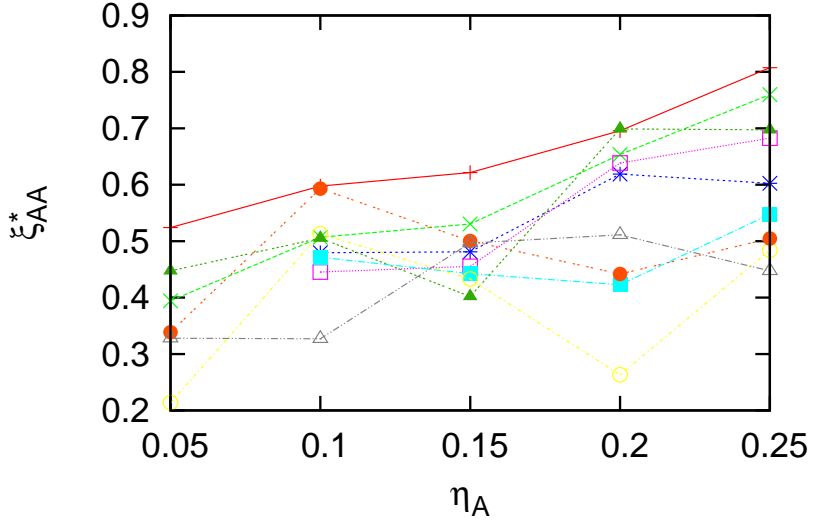


Figure 49: Reduced correlation length ξ_{AA}^* as function of η_A for different volume fractions of small particles $\eta_B = 0.02$ (red), $\eta_B = 0.04$ (green), $\eta_B = 0.05$ (blue), $\eta_B = 0.06$ (purple), $\eta_B = 0.07$ (turquoise), $\eta_B = 0.08$ (yellow), $\eta_B = 0.09$ (orange), $\eta_B = 0.12$ (gray), and $\eta_B = 0.17$ (dark green).

ticles one finds a significant decrease of b . The fit parameters are given in the caption of fig. 48. For $\eta_B \gtrsim 0.07$ the wavelength keeps within numerical errors constant. The relation of the characteristic length scale to the interparticle distance is perturbed by the inclusion of the small particles. Although, this exponential behavior has vanished for $\eta_B = 0.07$ the structure is still characterized by the big particles with σ_A . Further increase of the volume fraction of small particles yields a shift of the (constant) λ_b to smaller values down to σ_B .

Further evidence for a structural crossover is given by the correlation lengths ξ_{ij} extracted from the pair correlation functions. Fig. 49 shows ξ_{AA}^* as function of η_A . For few small particles ($\eta_B = 0.02$) this is a monotonically increasing function, i. e. the correlations enhance for larger densities. In the parameter range considered this behavior was found for the monodisperse system in [72] using MC and HNC methods. Note, that for smaller $\eta_A \lesssim 0.1$ and small ionic strength $I = 10^{-5} - 10^{-4} mol l^{-1}$ a decrease of ξ_{ij} is expected due to screening effects [72]. Inserting more small particles yields a shift of the function towards smaller lengths, i. e. they disturb the correlations of the big particles. A more detailed analysis of these data is not possible since the fluctuations are too big especially for large η_B . As function of

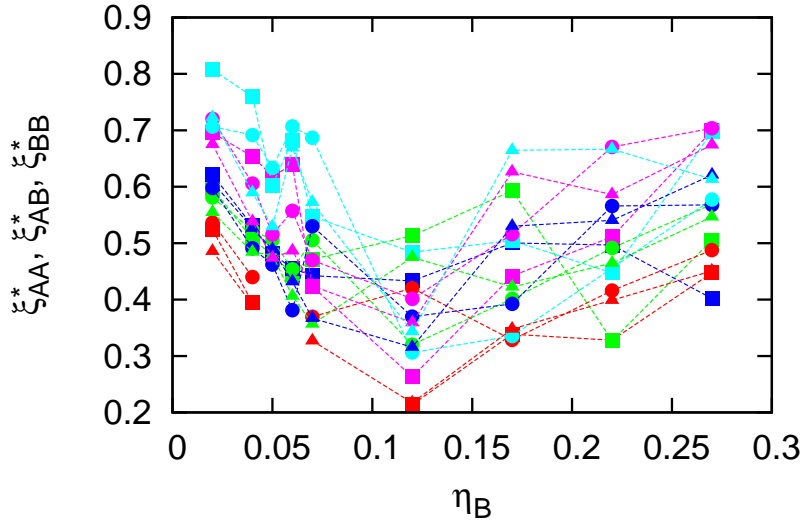


Figure 50: Reduced correlation lengths ξ_{AA}^* (squares), ξ_{AB}^* (circles), and ξ_{BB}^* (triangles) as function of η_B for different volume fractions of big particles $\eta_A = 0.05$ (red), $\eta_A = 0.1$ (green), $\eta_A = 0.15$ (blue), $\eta_A = 0.2$ (purple), and $\eta_A = 0.25$ (turquoise).

η_B the obtained values of ξ_{ij}^* plotted in fig. 50 exhibit a minimum about $\eta_B \approx 0.12$ which is located in the crossover region of fig. 47. A similar value of $\eta_B \approx 0.125$ at $\eta_A = 0.1$ was found for crossover in [48] using HS. There, these values were determined by integral equation methods. However, in [48] the crossover line depends on both η_A and η_B whereas in fig. 50 for screened charged particles the minimum of $\xi_{ij}^*(\eta_B)$ does not change with η_A . Keep in mind that, as for the monodisperse system discussed in chapter 5, the correlation lengths are strongly sensitive to the fitting eq. (145) of the MC data. However, figs. 49 and 50 provide an idea what is happening to the correlations in the bulk system. To clarify somewhat the data of fig. 50 the average of the three values ξ_{ij}^* is plotted in fig. 51 assuming ξ_{ij} to be equal (see sec. 3.9). The minimum in the correlation lengths as function of η_B might be explained as follows. In the crossover region found in fig. 47 the characteristic lengths change the behavior from a σ_A -dominated to a σ_B -dominated system. The occurring perturbations yield interferences as in fig. 45 and reduce the correlation lengths. In other words, at crossover there is less order in the system due to the perturbations.

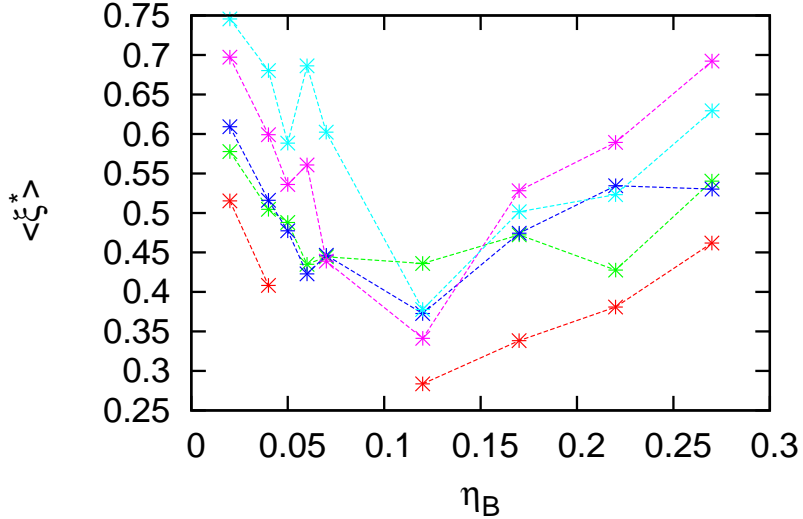


Figure 51: Average of the correlation lengths as function of η_B defined as $\langle \xi^* \rangle = (\xi_{AA}^* + \xi_{AB}^* + \xi_{BB}^*)/3$ for the same values of η_A as in fig. 50.

7.2 Impact of confinement on layering and composition of a binary mixture

In order to investigate the impact of confining walls on a binary mixture GCMC simulations are employed. It is reasonable to allow particle number fluctuations since the confining walls are expected to have an influence on the composition of the mixture. The mean pore composition is defined as

$$x_i = \frac{\bar{\rho}_i}{\bar{\rho}_A + \bar{\rho}_B} = \frac{\bar{\rho}_i}{\bar{\rho}} \quad (174)$$

with $\bar{\rho}_i = N_i/V$ and $\bar{\rho} = N/V$ being the mean pore particle densities and $i = A, B$. Depending on the wall separation one species might be squeezed out of the pore whereas the other one is pulled in. To this end several series of simulations have been done at small densities varying the wall separation L_z with the same choice of particles as in sec. 7.1 ($\sigma_A^* = 1.0$, $\sigma_B^* = 0.5$, $Z_A = 35$, $Z_B = 10$). Considering a system with $\eta_A = 0.01$ and $\eta_B = 0.001$ the normal pressure component P_{zz} in fig. 52 exhibits an oscillatory behavior as found for monodisperse suspensions (see sec. 5.1). These structural forces are induced by the layering of the particles. This layering, however, is for a mixture more complex than for a monodisperse system. Both species can behave in a different way which is shown in fig. 53a. On one hand the mean pore volume fraction of the big particles $\bar{\eta}_A$ decreases monotonically, i. e., there are less

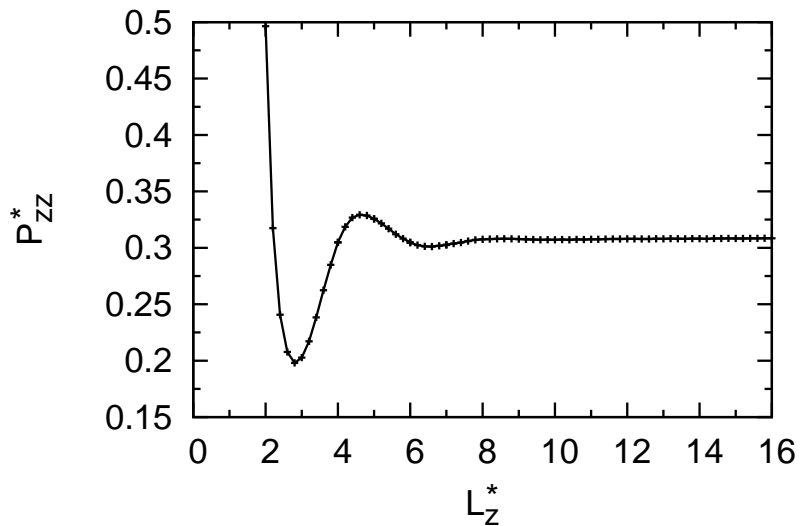


Figure 52: Solvation pressure P_{zz} as function of wall separation L_z for a binary mixture with $\sigma_A^* = 1.0$, $\sigma_B^* = 0.5$, $Z_A = 35$, and $Z_B = 10$ at $\eta_A = 0.01$ and $\eta_B = 0.001$.

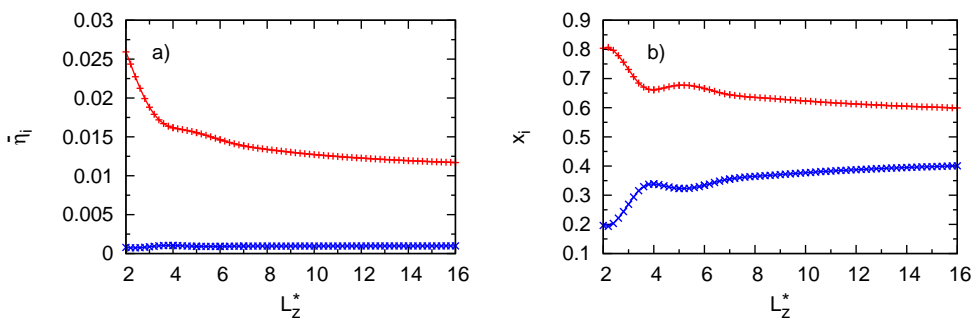


Figure 53: Same system as in fig. 52 showing the corresponding a) volume fractions $\bar{\eta}_i(L_z)$ and b) compositions $x_i(L_z)$ for particle species A (red plus symbols) and B (blue crosses).

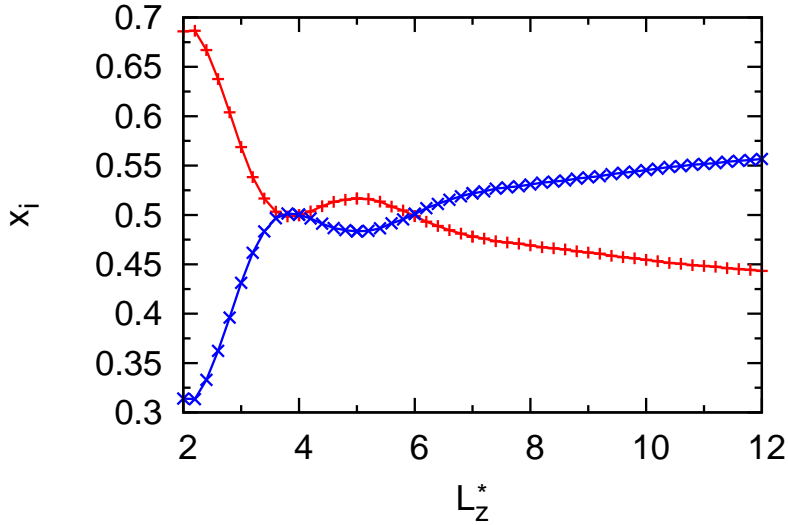


Figure 54: Compositions $x_i(L_z)$ for the binary mixture as in fig. 52 but at $\eta_B = 0.002$ for particle species A (red plus symbols) and B (blue crosses).

big particles per volume with increasing pore size. On the other hand, $\bar{\eta}_B$ increases monotonically with pore size. Both mean pore volume fractions tend towards their bulk values upon increasing L_z towards large values. We conclude that narrow pores adsorb big particles more efficiently than small ones. Furthermore, $\bar{\eta}_A$ slightly reflects the impact of the layering via an oscillatory change of the slope. A clearer view is shown by the composition of the mixture (see eq. (174)) in fig. 53b. The composition x_i is strongly affected by the layering where the oscillatory change of the slope seems to have the same period as the solvation pressure in fig. 52. A similar results of alternating compositions of the mixture as function of pore width was found in [6] investigating different mixtures in carbon nanotubes.

A different choice of the bulk value of $\eta_B = 0.002$ can have an interesting effect on the composition in the pore. There the number of small particles in the bulk is larger than of the big particles. As before decreasing the pore size yields a preferred adsorption of big particles and the composition changes, i. e., in the pore there are more big particles than small ones (see fig. 54).

To get a better idea of how the particles are adsorbed in the pore a closer look is taken on the structure perpendicular to the walls by computing local density profiles. To this end the mixture considered before at small bulk volume fractions $\eta_A = 0.01$ and $\eta_B = 0.002$ is simulated at different wall separations. The resulting profiles at $L_z = 4.0\sigma$ are plotted in fig. 55. Both

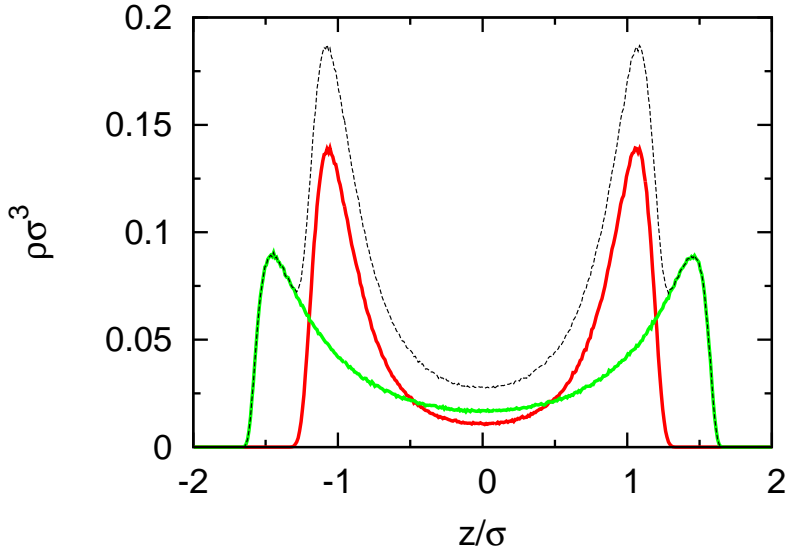


Figure 55: Local density profiles ρ_A (red solid line), ρ_B (green solid line), and $\rho_{tot} = \rho_A + \rho_B$ (black dashed line) in a pore of size $L_z = 4.0\sigma$ for a binary mixture with $\sigma_A^* = 1.0$, $\sigma_B^* = 0.5$, $Z_A = 35$, and $Z_B = 10$ at $\eta_A = 0.01$ and $\eta_B = 0.002$. Each species possesses two layers resulting four layers of the whole system.

species form two parallel particle layers where the big particle layers are more pronounced compared to these of the small particles. Furthermore, the small particles are located closer to the walls. Both effects might be explained as follows. On one hand the small particles can get closer to the walls due to their smaller excluded volume. On the other hand the slit pore is in terms of the length scale of the small particles larger than for the big ones, i. e., the effect of the confinement on species B which induces the layering is weaker. Another reason is the smaller bulk volume fraction η_B . In the end these effects yield effectively a four-layer system. The corresponding snapshot to fig. 55 is shown in fig. 56 in the side view. A similar behavior of the structure formation of the mixture under confinement was observed in [6] for mixtures in carbon nanotubes. There, depending on temperature and tube diameter the bigger OMCTS molecules with diameter 7.7\AA are located more closely to the center of the nanotube than the smaller cyclohexane molecules with 5.4\AA .

For a better understanding the structure formation of the mixture and how the mixture components influence each other, additional simulations for monodisperse systems at the same separation $L_z = 4.0\sigma$ are presented in

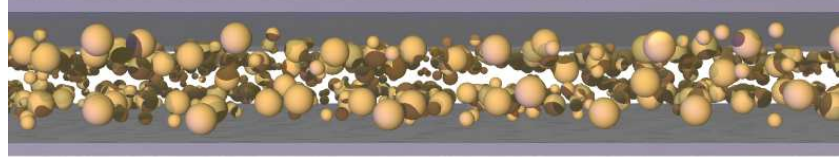


Figure 56: Snapshot of the slit pore containing the binary mixture of fig. 55 in the side view.

fig. 57. Neglecting the small particles but using the same volume fraction for the big ones as before ($\eta = 0.01$) the particle layers become softer, i. e., the density peaks are less pronounced and the minimum between the layers somewhat raises. The layer distance, however, does not change at least within numerical errors. Neglecting the big particles and keeping the density of the small particles at $\eta = 0.002$ as before a similar effect is observed. The layers become softer indicated by a significant raise of the density minimum between the layers. Furthermore, considering the maxima the layer distance seems to somewhat decrease. But this might be an effect of the softening itself. These observations for the two-layer system indicate that the inclusion of small particles to a confined big particle suspension enhance the layering. Including big particles to a small particle suspension the same effect is observed but it becomes more clear that the small particles are pressed out of the middle of the pore.

A further question which arises at this point is whether there is a difference in the formation of the layers for the species A and B . In a monodisperse system the layer formation proceeds with a certain periodicity upon increasing L_z which is reflected by the wavelength λ_f of the solvation forces. The solvation force for the binary system is shown in fig. 58 exhibiting an approximate wavelength $\lambda_f^* \approx 3.6$. This value was determined via the fit function $P_{zz}(L_z) - P_{bulk} \propto A_f \exp(-L_z/\xi_f) \cos(2\pi L_z/\lambda_f - \Theta_f)$ for $L_z \rightarrow \infty$ as predicted for monodisperse systems (see sec. 3.5). However, there are other effects arising from the mixture changing the asymptotic oscillatory behavior as derived from OZ theory. For large wall separations P_{zz} does not oscillate around P_{bulk} but it asymptotically approaches the bulk pressure. The quantity P_{zz} seems to be lowered. This has to be discussed in future work.

In order to extract the periodicity of the layering from local density profiles one can seek for values of L_z where new particle layers emerge. Beginning with species A two profiles are plotted in fig. 59 for $L_z = 2.6\sigma$ and 6.4σ . In the first case the one existing layer of A -particles begins to split up into two layers characterized by a minimum in ρ_A (fig. 59a). In the second case a third

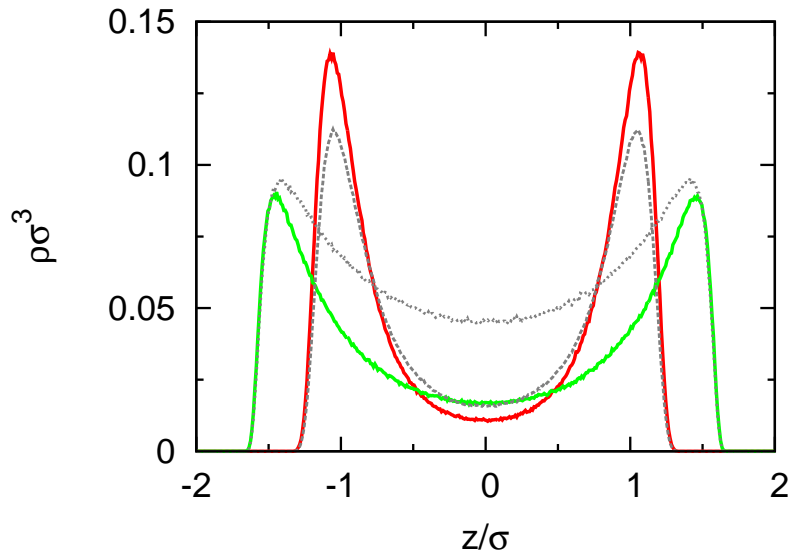


Figure 57: Comparison between mixture and monodisperse suspensions for the same system as in fig. 55. The mixture consists of big (red solid line, $\eta_A = 0.01$) and small particles (green solid line, $\eta_B = 0.002$). The gray dashed line includes only big particles at $\eta = 0.01$, whereas the gray dotted line only includes small particles at $\eta = 0.002$.

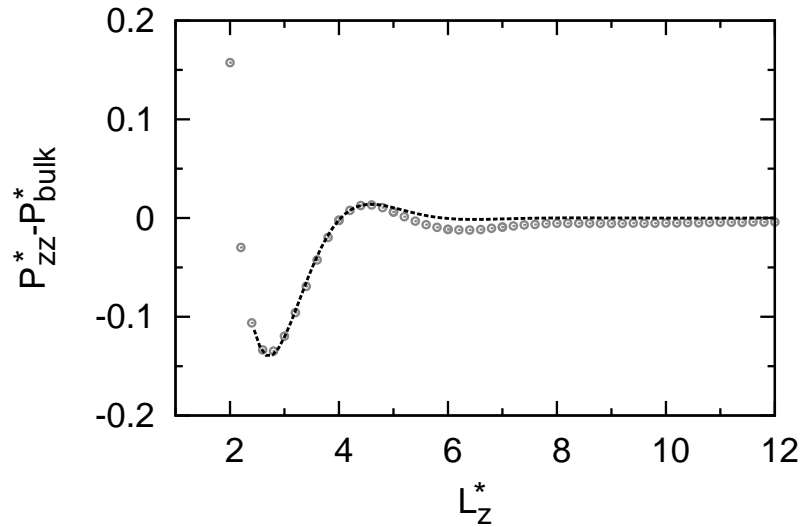


Figure 58: Solvation pressure P_{zz} as function of wall separation L_z for the system as in fig. 55. The dashed black line is the fit function (see text).

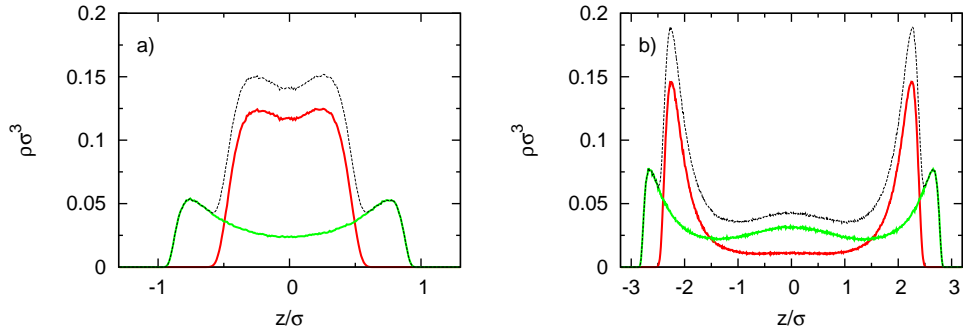


Figure 59: Local density profiles showing the emergence of a new layer of big particles for the system as in fig. 55 with a) $L_z = 2.6\sigma$ and b) $L_z = 6.4\sigma$.

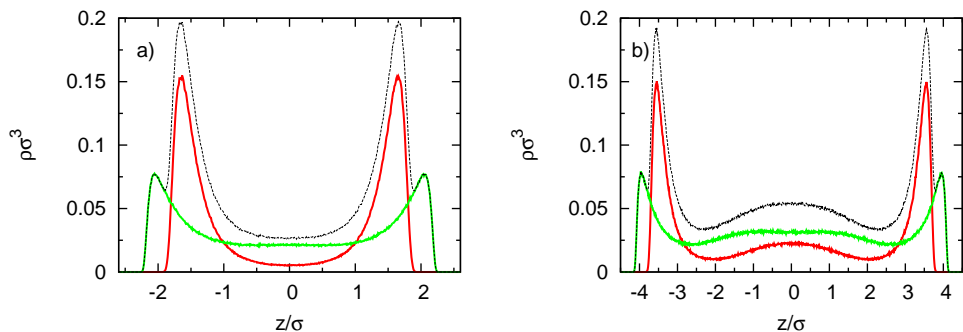


Figure 60: Local density profiles showing the emergence of a new layer of small particles for the system as in fig. 55 with a) $L_z = 5.2\sigma$ and b) $L_z = 9.0\sigma$.

layer begins to develop in the center of the pore characterized by an emerging bump (fig. 59b). The difference in the distance of these two wall separations is related to the periodic behavior of P_{zz} . The two separations mark the point of creating a new layer. Indeed, the difference is $\Delta L_z = 3.8\sigma$ which approximately equals the wavelength λ_f of the solvation pressure. Note, that due to statistical errors it is not possible to determine exactly the point where a new layer forms. For the B -particles a similar result is found plotted in fig. 60 for $L_z = 5.2\sigma$ and 9.0σ . In the smaller pore the small particles begin to form a third layer in the center whereas in the bigger pore a fourth layer emerges. Note, that in figs. 59 and 60 the (new) emerging layers are still very small. As for the big particles the difference between these two separation is also $\Delta L_z = 3.8\sigma$, i. e., the small particles form layers with the same periodicity as the big particles. This underlines the fact from ref. [74] that at small densities the layering is determined by the mean interparticle separation (i. e., the packing fraction) but not the particle size.

8 Conclusion and outlook

In this thesis we investigated the structure formation of charged, colloidal suspensions containing spherical particles in the bulk and the confinement. These suspensions are characterized by the particle size, surface charge, salt concentration, and, in case of binary mixtures, the composition. The impact of these parameters and the influence of confining plane-parallel surfaces (slab-geometry) on the structure formation was examined via Monte-Carlo simulations and compared with CP-AFM experiments. A main issue was the influence of surface charges of the confining walls on the particle-wall interaction and, thus, on the structure formation. Our findings for monodisperse systems are published in [72, 43, 45, 73, 44].

In chapter 5, monodisperse suspensions were investigated at low densities by computing solvation pressure curves for 26nm sized, charged particles. The results revealed that an increasing salt concentration I decreases the amplitude of the oscillating pressure [72] and changes the asymptotic decay length ξ_f . However, the asymptotic wavelength λ_f is unaffected. Whereas λ_f yields a power-law behavior as function of the bulk volume fraction ϕ [101, 74], the decay length exhibits a non-monotonic behavior for $I \lesssim 5 * 10^{-4} \text{ mol l}^{-1}$. This effect results from a competition between the increasing screening strength due to more counterions (recall, that their number increases with density) and the increasing packing of the macroions. Smaller particles of the sizes 16nm and 9nm , possessing smaller surface charges, are characterized by a decreased amplitude of the pressure as compared to the bigger ones [73, 130]. As function of bulk particle density, λ_f of each particle type falls on a master curve with power-law behavior. This was not found for ξ_f . In contrast to our results for ξ_f , CP-AFM predicts a master curve for the decay lengths as well, at least in the experimental parameter range [130]. Here, we note that the determination of ξ_f is difficult at small densities due to the fast decaying oscillations of the forces.

An important aim of the thesis is the investigation of surface charges of the confining walls and their impact on the structure formation [45]. To this end, screened, negatively charged silica and mica walls were modeled which contributed additional counterions to the suspension. This is motivated by CP-AFM experiments, which we published in [45], where an unexpected behavior of force enhancement by replacing charged silica walls by higher charged mica walls was found. According to former studies [26, 4], the additional wall counterions are located near the walls. Thus, we suggested that the impact on the screening of the particle-wall interaction is essential whereas the influence on the particle-particle interaction yields minor effects on the layering [26] and the in-plane correlation functions. We

modified the screening parameter of the particle-wall interaction such that it involves particle and wall counterions. The resulting potential is characterized by a non-monotonic behavior as function of the surface potential ψ_S . This emerges for varying $|\psi_S|$ from the competition between the wall repulsion and the screening. In more detail, increasing $|\psi_S|$, an effective narrowing of the slit pore is followed by an effective broadening above $|\psi_S| \approx 40mV$. To our knowledge, none of the previously suggested models for charged walls [15, 4, 52] shows a non-monotonic behavior in the parameter range considered. Employing GCMC simulations, the computed solvation pressure curves revealed the non-monotonicity. More precisely, between $|\psi_S| = 0$ and $40mV$ the amplitude of the pressure decreases while for $|\psi_S| \gtrsim 40mV$ an enhancement occurs. This finding is consistent with the experimental data for silica and mica walls which have surface potentials of $|\psi_S| = 80mV$ and $160mV$, respectively. The asymptotic wave- and decay lengths, however, are not affected by the surface charges which conforms with DFT predictions [34, 48]. Furthermore, local density profiles revealed that the layers are softened for increasing repulsion (replacing the mica by silica walls).

In chapter 6, the impact of the density, surface separation, and surface charge on translational order in the suspension is studied which we discussed in detail in [43, 44]. The DLVO potential alone does not induce freezing in the density range considered here [51]. However, we expect that SS with DLVO interaction exhibit a freezing transition at smaller densities as compared to SS alone. Our bulk simulations revealed a broadened metastable fluid-solid range as compared to SS [57]. In confinement, the capillary freezing known from HS [29] is shifted towards smaller densities as well. We found evidence for the density shift by employing GCMC simulations, where deviations in the structural forces from the exponential decay occurred. Computing in-plane bond angle order parameters revealed an alternation between (staggered) hexagonal and squared order for varying wall separations. This effect results from a competition between the arrangement of the particles in layers and the in-plane packing within the layer. As function of the bulk density, we found an onset of crystallization characterized by a significant increase of the bond order parameter. Computing the pressure and bond order susceptibilities, we found evidence that the increase might be related to a first-order phase transition. Confirmed via isobaric-isothermal MC simulations, first-order solid-solid transitions between hexagonal and squared structures were found. Increasing the parallel pressure, the mean pore density and the bond order parameters clearly exhibit a metastable range of both structures. A closer look on the squared structures at high densities shows that also domain-like structures can occur.

A focus in this thesis is again the impact of surface charges where we found

that charged walls can shift or totally change the onset of crystallization. Considering, e. g., $L_z = 2.4\sigma$, silica walls induced a hexagonal order whereas for mica walls a squared order was found. The latter occurred at even smaller chemical potentials. Corresponding bond order fluctuations gave evidence for first-order transitions. Using uncharged surfaces at the same wall separation suppresses a possible transition. The bond order parameters also showed that “large-scale” fluctuations occur near phase coexistence, i. e., the system “jumps” between two coexisting phases which is typical for first-order phase transitions. This yields a typical double-peak structure in the probability distribution of the order parameter. From a theoretical point of view, taking the surface potential of the confining walls as a continuous parameter yields a non-monotonic structuring due to the non-monotonicity of the wall potential. Bond order parameters together with bond order susceptibilities revealed that two “transitions” occur. On one hand, the number of layers changes non-monotonically for increasing $|\psi_S|$. On the other hand, wall-charge-induced phase transitions between fluid, squared, and hexagonal phases are found. The system is characterized by a reentrant freezing behavior.

Chapter 7 extends the considerations towards strongly asymmetric mixtures containing particles of different sizes and charges [73]. A main aspect is the effect of structural crossover in bulk systems in three or two dimensions known from simulations of HS mixtures [47, 48, 10, 61] and experiments [10]. To this end, we employed canonical MC simulations. Depending on the composition of the mixture, the asymptotic wavelength approximately equals the diameter of species A or B at intermediate total volume fractions. Between these regions, a smooth crossover between the wavelengths takes place. For small total volume fractions, the typical power-law behavior as in monodisperse systems occurs. Furthermore, we obtained that the correlation length decreases in the vicinity of the crossover. Within GCMC simulations, the impact of confinement was investigated on the composition and the layering of the suspension. As compared to the bulk, a strong confinement changed the composition significantly, i. e., more small particles are squeezed out than big particles. Also the layering exhibited a non-trivial behavior. In more detail, the small particles were pushed towards the walls for the parameters considered. Depending on the wall separation, even the number of layers was found to be different for each of the species.

Considering the results, presented in this thesis, new questions arise which are a basis for future work. Furthermore, it would be worthwhile to confirm the theoretical findings in experiments, especially the freezing phenomena in uncharged and charged confinement. Within this context, the unusual shape of the structural forces are of interest which might be related to the onset of crystallization. It is noteworthy that within the CP-AFM exper-

iment, deviations from the fluid-like behavior was found for (strongly confined) monolayers at intermediate densities where our simulations predicted fluid-like behavior. Whereas our theoretical approach was successful in predicting qualitative properties of the experiment for larger separations or small densities, it might be necessary to take further effects into account if different parameter ranges are considered. In this context, further fluid-wall interactions and microion distributions in confinement should be discussed. There, van-der-Waals interaction and image charges are of interest. The latter can be investigated via primitive model simulations [3].

Another effect concerning freezing in strong confinement is the existence of a hexatic phase [50]. Although we found evidence for first-order phase transitions in one- and two-layer systems, we cannot exclude the phenomenon of two-stage melting. One problem is that it is supposed to occur in a very narrow density range which requires more detailed examinations. Furthermore, it is known that the two stages of melting can occur simultaneously in the form of a conventional first-order transition [114].

Considering strongly asymmetric mixtures, we suppose that the effect of structural crossover, which we considered in homogeneous systems, will be affected by confining surfaces, especially the surface charge. Another issue is the in-plane ordering at large densities. The charged particles might freeze at different densities yielding a fluid-solid mixture. It would be desirable to investigate these aspects experimentally. In this context, different theoretical models of the interactions in the mixture could be discussed involving non-additivity [5]. Beyond the binary character of the mixtures considered, polydispersity is a further field receiving attention in research [126].

In real life, many complex types of confinement exist involving porous materials as, e. g., zeolites or MCM-41 [76]. Although modeled slit-pores yield good agreement with experiments within certain parameter ranges, it is reasonable to take more details about the geometry into account as, e. g., cylindrical pores and structured or deformable surfaces [49]. Thus, the question is how the precise geometry influences the structure formation of charged suspensions including the counterion distribution.

So far we considered equilibrium properties of charged colloids. An important field of research receiving great attention is rheology. Non-equilibrium systems induce a large variety of complex, dynamical behavior in colloidal suspensions [81]. For instance, lane formation in externally driven systems [127], accelerated motion of self-propelled particles in a shear flow [115], and motion of rod-like viruses in shear flows [77] are recent topics. Thus, we suppose that combining the models presented in this thesis with rheology will add interesting dynamical effects to the known phenomena and will have great impact on the structuring of the suspensions, especially between

charged surfaces. But also other external influences on confined, charged suspensions are of interest as, e. g., gravitation [82] and external electric or magnetic fields.

We think that the models and our findings are important for colloidal sciences in general, because they are transferable to different systems as well such as polyelectrolytes (involving (branched) chains and stars), elastic spheres, macromolecules, micelles, cells, liquid crystals, and dusty plasmas. Many of these systems can be found in real life in porous materials and other types of confinement. They are interesting for applications (e. g., drug targeting), membranes in biology or technology, and optical properties of materials (e. g., photonic crystals).

A Calculation of local bond angle order parameters

In this section we describe how the in-plane bond order parameters can be calculated efficiently for the use in computer programs. This parameter for an order n is given as an ensemble average of the quantity

$$\psi_{n,i}^0 = \left| \frac{1}{N_i^b} \sum_{j=1}^{N_i^b} \exp(in\Theta_j) \right| \quad (175)$$

for particle i with N_i^b neighbors. The particles are located on the x - y -plane. We need to take the absolute value of an imaginary function. Hence, the sum in eq. (175) can be re-expressed as

$$\begin{aligned} \sum_{j=1}^{N_i^b} \exp(in\Theta_j) &= \sum_{j=1}^{N_i^b} \cos(n\Theta_j) + i \sum_{j=1}^{N_i^b} \sin(n\Theta_j) \\ &\equiv Re_{n,i} + i Im_{n,i} \end{aligned} \quad (176)$$

with the real part $Re_{n,i}$ and the imaginary part $Im_{n,i}$. Thus, eq. (175) yields together with eq. (176)

$$\psi_{n,i}^0 = \frac{1}{N_i^b} \sqrt{Re_{n,i}^2 + Im_{n,i}^2}. \quad (177)$$

The angle Θ_j is enclosed by the particle bond vector and an arbitrary axis in the x - y -plane. The bond vector is the vector between particle i and the neighboring particle considered. Thus, the angles are determined via

$$\cos \Theta_j = \frac{\Delta x}{\sqrt{\Delta x^2 + \Delta y^2}} \quad \text{and} \quad (178)$$

$$\sin \Theta_j = \frac{\Delta y}{\sqrt{\Delta x^2 + \Delta y^2}}. \quad (179)$$

where a case-by-case analysis is necessary if the inverse functions are taken. Finally, using eqs. (178) and (179) and the addition theorems for trigonometric functions, the summands in $Re_{n,i}$ and $Im_{n,i}$ (see eq. (176)) read for

the orders $n = 2, 4, 6, 8$

$$\cos 2\Theta_j = \cos^2 \Theta_j - \sin^2 \Theta_j, \quad (180)$$

$$\sin 2\Theta_j = 2 \sin \Theta_j \cos \Theta_j, \quad (181)$$

$$\cos 4\Theta_j = \cos^2 2\Theta_j - \sin^2 2\Theta_j, \quad (182)$$

$$\sin 4\Theta_j = 2 \sin 2\Theta_j \cos 2\Theta_j, \quad (183)$$

$$\cos 6\Theta_j = \cos 2\Theta_j \cos 4\Theta_j - \sin 2\Theta_j \sin 4\Theta_j, \quad (184)$$

$$\sin 6\Theta_j = \sin 2\Theta_j \cos 4\Theta_j + \cos 2\Theta_j \sin 4\Theta_j, \quad (185)$$

$$\cos 8\Theta_j = \cos^2 4\Theta_j - \sin^2 4\Theta_j, \quad (186)$$

$$\sin 8\Theta_j = 2 \sin 4\Theta_j \cos 4\Theta_j. \quad (187)$$

The next neighbors of a particle can be determined via two different methods. The first defines the neighbors as all particles within a cut-off radius around the central particle. This radius is given as the first minimum in the in-plane correlation function $g_{||}(r)$. In other words, the first peak in $g_{||}$ are the next neighbors which form a shell around the central particle. Another method is the Delaunay triangulation which gives a more precise definition of the next neighbors [100]. We used both methods in our simulations, however, no qualitative difference was found in the results. To determine squared order via Delaunay triangulation it is necessary to compute ψ_8 instead of ψ_4 since for perfect squared structure, ψ_4 keeps smaller than 1 due to the triangulation.

B Fourier transforms of Coulomb and Yukawa potential

The Fourier transform of the Coulomb potential can be solved within spherical coordinates which is sketched briefly. Using the substitution $\mathbf{s} = \mathbf{r} - \mathbf{R}$, the Fourier transformation with respect to \mathbf{r} gets

$$\mathcal{F}\left[\frac{1}{|\mathbf{r} - \mathbf{R}|}\right](\mathbf{k}) = \exp(-i\mathbf{k} \cdot \mathbf{R}) \int_{\mathbb{R}} d^3s \exp(-i\mathbf{k} \cdot \mathbf{s}) \frac{1}{|\mathbf{s}|}. \quad (188)$$

Transforming eq. (188) into spherical coordinates and integrating over the angles yields

$$\mathcal{F}\left[\frac{1}{|\mathbf{r} - \mathbf{R}|}\right](\mathbf{k}) = \exp(-i\mathbf{k} \cdot \mathbf{R}) 2\pi \frac{i}{k} \int_0^\infty ds [\exp(-iks) - \exp(iks)]. \quad (189)$$

By multiplying the factor $\lim_{\gamma \rightarrow 0} e^{-\gamma s}$, which is 1, to the integrand of eq. (189), the integral converges. There, the limit can be written outside of the integral since it does not depend on s . Thus, the transform reads

$$\mathcal{F} \left[\frac{1}{|\mathbf{r} - \mathbf{R}|} \right] (\mathbf{k}) = \exp(-i\mathbf{k} \cdot \mathbf{R}) \lim_{\gamma \rightarrow 0} \frac{4\pi}{k^2 + \gamma^2} \quad (190)$$

$$= \exp(-i\mathbf{k} \cdot \mathbf{R}) \frac{4\pi}{k^2}. \quad (191)$$

The Fourier transformation of the Yukawa potential is derived in the same way as eq. (191). The convergence is guaranteed by the exponential term in the numerator and the limit is not needed. Thus, we get

$$\mathcal{F} \left[\frac{\exp(-m|\mathbf{r} - \mathbf{R}|)}{|\mathbf{r} - \mathbf{R}|} \right] (\mathbf{k}) = \exp(-i\mathbf{k} \cdot \mathbf{R}) \frac{4\pi}{k^2 + m^2}. \quad (192)$$

References

- [1] C. Alba-Simionescu, B. Coasne, G. Dosseh, G. Dudziak, K. E. Gubbins, R. Radhakrishnan, and M. Sliwinska-Bartkowiak. *J. Phys.: Condens. Matter*, 18:R15, 2006.
- [2] B. J. Alder and T. E. Wainwright. *J. Chem. Phys.*, 27:1208–1209, 1957.
- [3] E. Allahyarov, I. D’Amico, and H. Löwen. *Phys. Rev. Lett.*, 81:1334, 1998.
- [4] E. Allahyarov, I. D’Amico, and H. Löwen. *Phys. Rev. E*, 60:3199–3210, 1999.
- [5] E. Allahyarov and H. Löwen. *J. Phys.: Condens. Matter*, 21:424117, 2009.
- [6] K. G. Ayappa. *Langmuir*, 14:880, 1998.
- [7] K. G. Ayappa and C. Ghatak. *J. Chem. Phys.*, 117:5373, 2002.
- [8] V. Ballenegger and J.-P. Hansen. *J. Chem. Phys.*, 122:114711, 2005.
- [9] P. Bartlett and A. I. Campbell. *Phys. Rev. Lett.*, 95:128302, 2005.
- [10] J. Baumgartl, R. P. A. Dullens, M. Dijkstra, R. Roth, and C. Bechinger. *Phys. Rev. Lett.*, 98:198303, 2007.
- [11] C. Bechinger, D. Rudhardt, P. Leiderer, R. Roth, and S. Dietrich. *Phys. Rev. Lett.*, 83:3960–3963, 1999.
- [12] S. H. Behrens and D. G. Grier. *Phys. Rev. E*, 64:050401(R), 2001.
- [13] G. M. Bell, S. Levine, and L. N. McCartney. *J. Coll. Int. Sc.*, 33:335–359, 1970.
- [14] S. Bhattacharjee and M. Elimelech. *J. Coll. Int. Sc.*, 193:273–285, 1997.
- [15] S. Bhattacharjee, M. Elimelech, and M. Borkovec. *Croat. Chem. Acta*, 71:883, 1998.
- [16] K. Binder. *Rep. Prog. Phys.*, 50:783, 1987.
- [17] A. Blanco, E. Chomski, S. Grabtchak, M. Ibáñez, S. John, S. W. Leonard, C. Lopez, F. Meseguer, H. Miguez, J. P. Mondia, G. A. Ozin, O. Toader, and H. M. van Driel. *Nature*, 405:437–440, 2000.

- [18] I. N. Bronstein and K. A. Semendjajew. *Taschenbuch der Mathematik*. Teubner Verlagsgesellschaft, Leipzig, and Verlag Nauka, Moskau, 19 edition, 1979.
- [19] C. Brunet, J. G. Malherbe, and S. Amokrane. *J. Chem. Phys.*, 130:134908, 2009.
- [20] H.-J. Butt, K. Graf, and M. Kappl. *Physics and Chemistry of Interfaces*. Wiley-VCH, Weinheim, 2 edition, 2006.
- [21] M. K. Chalam, K. E. Gubbins, E. de Miguel, and L. F. Rull. *Mol. Sim.*, 7:357–385, 1991.
- [22] D. L. Chapman. *Phil. Mag.*, 25:475, 1913.
- [23] R. F. Cracknell, D. Nicholson, and N. Quirke. *Mol. Phys.*, 80:885, 1993.
- [24] P. Debye and E. Hückel. *Physikalische Zeitschrift*, 24:185, 1923.
- [25] A. Delville. *J. Phys. Chem. B*, 109:8164, 2005.
- [26] A. M. Denton and H. Löwen. *Thin Solid Films*, 330:7–13, 1998.
- [27] B. Derjaguin. *Kolloid-Z.*, 69:155–164, 1934.
- [28] B. Derjaguin. *Trans. Faraday Soc.*, 35:203–215, 1940.
- [29] M. Dijkstra. *Phys. Rev. Lett.*, 93:108303, 2004.
- [30] M. Dijkstra, R. van Roij, R. Roth, and A. Fortini. *Phys. Rev. E*, 73:041404, 2006.
- [31] H. Dominguez, M. P. Allen, and R. Evans. *Mol. Phys.*, 96:209–229, 1999.
- [32] W. A. Ducker, T. J. Senden, and R. M. Pashley. *Nature*, 353:239–241, 1991.
- [33] S. Engström and H. Wennerström. *J. Phys. Chem.*, 82:2711, 1978.
- [34] R. Evans, J. R. Henderson, D. C. Hoyle, A. O. Parry, and Z. A. Sabeur. *Mol. Phys.*, 80:755–775, 1993.
- [35] B. Fazelabdolabadi, J. Y. Walz, and P. R. Van Tassel. *J. Phys. Chem. B*, 113:13860–13865, 2009.
- [36] M. E. Fisher and B. Widom. *J. Chem. Phys.*, 50:3756–3772, 1969.

- [37] A. Fortini and M. Dijkstra. *J. Phys.: Condens. Matter*, 18:L371, 2006.
- [38] V. E. Fortov, A. V. Ivlev, S. A. Khrapak, A. G. Khrapak, and G. E. Morfill. *Phys. Rep.*, 421:1–103, 2005.
- [39] D. Frenkel and B. Smit. *Understanding Molecular Simulations*. Academic Press, San Diego, 2002.
- [40] P. Gallo, A. Attili, and M. Rovere. *Phys. Rev. E*, 80:061502, 2009.
- [41] B. Götzelmann, R. Evans, and S. Dietrich. *Phys. Rev. E*, 57:6785–6800, 1998.
- [42] G. Gouy. *Journ. de Phys.*, 9:457, 1910.
- [43] S. Grandner and S. H. L. Klapp. *J. Chem. Phys.*, 129:244703, 2008.
- [44] S. Grandner and S. H. L. Klapp. *Europhys. Lett.*, 90:68004, 2010.
- [45] S. Grandner, Y. Zeng, R. von Klitzing, and S. H. L. Klapp. *J. Chem. Phys.*, 131:154702, 2009.
- [46] J. Gregory. *J. Coll. Int. Sc.*, 51:44, 1975.
- [47] C. Grodon, M. Dijkstra, R. Evans, and R. Roth. *J. Chem. Phys.*, 121:7869, 2004.
- [48] C. Grodon, M. Dijkstra, R. Evans, and R. Roth. *Mol. Phys.*, 103:3009, 2005.
- [49] G. Günther, J. Prass, O. Paris, and M. Schoen. *Phys. Rev. Lett.*, 101:086104, 2008.
- [50] B. I. Halperin and D. R. Nelson. *Phys. Rev. Lett.*, 41:121–124, 1978.
- [51] S. Hamaguchi, R. T. Farouki, and D. H. E. Dubin. *Phys. Rev. E*, 56:4671, 1997.
- [52] J. P. Hansen and I. R. McDonald. *Theory of Simple Liquids*. Academic Press, Amsterdam, 3 edition, 2006.
- [53] S. Heidenreich, S. Hess, and S. H. L. Klapp. *Phys. Rev. Lett.*, 102:028301, 2009.
- [54] L. E. Helseth, H. Z. Wen, and T. M. Fischer. *J. Appl. Phys.*, 99:024909, 2006.

- [55] J. R. Henderson and Z. A. Sabeur. *J. Chem. Phys.*, 97:6750–6758, 1992.
- [56] W. G. Hoover and F. H. Ree. *J. Chem. Phys.*, 49:3609–3617, 1968.
- [57] W. G. Hoover, M. Ross, and K. W. Johnson. *J. Chem. Phys.*, 52:4931, 1970.
- [58] P. Hopkins, A. J. Archer, and R. Evans. *Phys. Rev. E*, 71:027401, 2005.
- [59] P. Hopkins, A. J. Archer, and R. Evans. *J. Chem. Phys.*, 124:054503, 2006.
- [60] P. Hopkins, A. J. Archer, and R. Evans. *J. Chem. Phys.*, 129:214709, 2008.
- [61] P. Hopkins and M. Schmidt. *J. Phys.: Condens. Matter*, 22:325108, 2010.
- [62] R. G. Horn, D. F. Evans, and B. W. Ninham. *J. Phys. Chem.*, 92:3531–3537, 1988.
- [63] R. G. Horn and J. N. Israelachvili. *J. Chem. Phys.*, 75:1400–1411, 1981.
- [64] P. Hu and C. Xiao. *Phys. Lett. A*, 353:422–426, 2006.
- [65] A.-P. Hyyninen and M. Dijkstra. *Phys. Rev. E*, 68:021407, 2003.
- [66] J. N. Israelachvili and R. M. Pashley. *Nature*, 306:249, 1983.
- [67] I. B. Ivanov and D. S. Dimitrov. *Thin Liquid Films*. New York: Dekker, 1988.
- [68] A. V. Ivlev, S. K. Zhdanov, H. M. Thomas, and G. E. Morfill. *Europhys. Lett.*, 85:45001, 2009.
- [69] B. Jönsson, A. Broukhno, J. Forsman, and T. Åkesson. *Langmuir*, 19:9914–9922, 2003.
- [70] J. Jordanovic and S. H. L. Klapp. *Phys. Rev. Lett.*, 101:038302, 2008.
- [71] R. Jurgons, C. Seliger, A. Hilpert, L. Trahms, S. Odenbach, and C. Alexiou. *J. Phys.: Condens. Matter*, 18:S2893–S2902, 2006.
- [72] S. H. L. Klapp, S. Grandner, Y. Zeng, and R. von Klitzing. *J. Phys.: Condens. Matter*, 20:494232, 2008.

- [73] S. H. L. Klapp, S. Grandner, Y. Zeng, and R. von Klitzing. *Soft Matter*, 6:2330, 2010.
- [74] S. H. L. Klapp, D. Qu, and R. von Klitzing. *J. Phys. Chem. B*, 111:1296, 2007.
- [75] S. H. L. Klapp, Y. Zeng, D. Qu, and R. von Klitzing. *Phys. Rev. Lett.*, 100:118303, 2008.
- [76] C. T. Kresge, M. E. Leonowicz, W. J. Roth, J. C. Vartuli, and J. S. Beck. *Nature*, 359:710–712, 1992.
- [77] M. P. Lettinga, Z. Dogic, H. Wang, and J. Vermant. *Langmuir*, 21:8048–8057, 2005.
- [78] S. Levine and A. Suddaby. *Proc. Phys. Soc. A*, 64:287–302, 1951.
- [79] H. Li-Xin, X. Chang-Ming, H. Ping, and G. Hai-Xia. *Chinese Physics B*, 18:1287–1293, 2009.
- [80] L. Liu and I. Nerensteins. *Coll. Surf. A*, 317:636, 2008.
- [81] H. Löwen. *J. Phys.: Condens. Matter*, 13:R415–R432, 2001.
- [82] H. Löwen and E. Allahyarov. *J. Chem. Phys.*, 135:134115, 2011.
- [83] H. Löwen, J. P. Hansen, and P. A. Madden. *J. Chem. Phys.*, 98:3275, 1993.
- [84] H. Löwen, A. Härtel, A. Barreira-Fontechá, H. J. Schöpe, E. Allahyarov, and T. Palberg. *J. Phys.: Condens. Matter*, 20:404221, 2008.
- [85] M. Mazars. *Mol. Phys.*, 105:1909–1925, 2007.
- [86] M. Mazars. *Europhys. Lett.*, 84:55002, 2008.
- [87] R. Messina and H. Löwen. *Phys. Rev. Lett.*, 91:146101, 2003.
- [88] N. Metropolis, A. W. Rosenbluth, M. N. Rosenbluth, A. H. Teller, and E. Teller. *J. Chem. Phys.*, 21:1087–1092, 1953.
- [89] D. J. Mitchell, B. W. Ninham, and B. A. Pailthorpe. *J. Chem. Soc., Faraday Trans. 2*, 74:1116–1125, 1978.
- [90] W. J. Moore. *Physical Chemistry*. Prentice-Hall, Englewood Cliffs, 4 edition, 1972.

- [91] I. Nezbeda and J. Kolafa. *Mol. Sim.*, 5:391–403, 1991.
- [92] A. D. Nikolov and D. T. Wasan. *Langmuir*, 8:2985–2994, 1992.
- [93] L. S. Ornstein and F. Zernike. *Proc. Acad. Sci.*, 17:793, 1914.
- [94] E. C. Oğuz, R. Messina, and H. Löwen. *Europhys. Lett.*, 86:28002, 2009.
- [95] E. C. Oğuz, R. Messina, and H. Löwen. *J. Phys.: Condens. Matter*, 21:424110, 2009.
- [96] R. Parthasarathy, P. A. Cripe, and J. T. Groves. *Phys. Rev. Lett.*, 95:048101, 2005.
- [97] M. Piech and J. Y. Walz. *J. Coll. Int. Sc.*, 253:117–129, 2002.
- [98] M. Piech and J. Y. Walz. *J. Phys. Chem. B*, 108:9177–9188, 2004.
- [99] B. Pouliquen, D. J. W. Aastuen, and N. A. Clark. *Phys. Rev. A*, 44:6616–6625, 1991.
- [100] W. H. Press, S. A. Teukolsky, W. T. Vetterling, and B. P. Flannery. *Numerical Recipes*. Cambridge University Press, New York, 3rd ed. edition, 2007.
- [101] C. V. Raman. *Philos. Mag.*, 47:671, 1924.
- [102] F. Ramiro-Manzano, F. Meseguer, E. Bonet, and I. Rodriguez. *Phys. Rev. Lett.*, 97:028304, 2006.
- [103] P. Richetti and P. Kékicheff. *Phys. Rev. Lett.*, 68:1951–1954, 1992.
- [104] Y. Rosenfeld. *J. Chem. Phys.*, 98:8126–8148, 1993.
- [105] R. Roth, R. Evans, and S. Dietrich. *Phys. Rev. E*, 62:5360–5377, 2000.
- [106] I. Rouzina and V. A. Bloomfield. *J. Phys. Chem.*, 100:9977–9989, 1996.
- [107] M. Schmidt and H. Löwen. *Phys. Rev. Lett.*, 76:4552–4555, 1996.
- [108] M. Schmidt and H. Löwen. *Phys. Rev. E*, 55:7228–7241, 1997.
- [109] M. Schmiedeberg and H. Stark. *Phys. Rev. Lett.*, 101:218302, 2008.
- [110] M. Schoen and S. H. L. Klapp. *Reviews in Computational Chemistry*, volume 24. Wiley, New Jersey, 2007.

- [111] B. I. Shklovskii. *Phys. Rev. E*, 60:5802–5811, 1999.
- [112] C. Stubenrauch and R. v. Klitzing. *J. Phys.: Condens. Matter*, 15:R1197–R1232, 2003.
- [113] J. Tallon. *Phys. Rev. Lett.*, 57:1328–1331, 1986.
- [114] J. L. Tallon. *Phys. Rev. B*, 22:453–455, 1980.
- [115] B. ten Hagen, R. Wittkowski, and H. Löwen. *Phys. Rev. E*, 84:031105, 2011.
- [116] A. Tulpár, P. R. Van Tassel, and J. Y. Walz. *Langmuir*, 22:2876–2883, 2006.
- [117] J. P. Valleau, R. Ivkov, and G. M. Torrie. *J. Chem. Phys.*, 95:520–532, 1991.
- [118] E. C. M. Vermolen, A. Kuijk, L. C. Filion, M. Hermes, J. H. J. Thijssen, M. Dijkstra, and A. van Blaaderen. *Proc. Natl. Acad. Sci.*, 106:16063–16067, 2009.
- [119] E. J. W. Verwey and J. T. G. Overbeek. *Theory of Stability of Lyophobic Colloids*. Elsevier, Amsterdam, 1948.
- [120] R. L. C. Vink and J. Horbach. *J. Chem. Phys.*, 121:3253–3258, 2004.
- [121] H. H. von Grünberg, L. Helden, P. Leiderer, and C. Bechinger. *J. Chem. Phys.*, 114:10094–10104, 2001.
- [122] A. Vorobiev, J. Major, H. Dosch, G. Gordeev, and D. Orlova. *Phys. Rev. Lett.*, 93:267203, 2004.
- [123] F. Wang and D. P. Landau. *Phys. Rev. Lett.*, 86:2050, 2001.
- [124] D. T. Wasan and A. D. Nikolov. *Nature*, 423:156, 2003.
- [125] B. Widom. *J. Chem. Phys.*, 39:2808–2812, 1963.
- [126] N. B. Wilding. *J. Chem. Phys.*, 130:104103, 2009.
- [127] A. Wysocki and H. Löwen. *J. Phys.: Condens. Matter*, 16:7209–7224, 2004.
- [128] F. Yan and W. A. Goedel. *Chem. Mater.*, 16:1622–1626, 2004.

- [129] M. Yi, H. Nymeyer, and H.-X. Zhou. *Phys. Rev. Lett.*, 101:038103, 2008.
- [130] Y. Zeng, S. Grandner, C. L. P. Oliveira, A. F. Thünemann, O. Paris, J. S. Pedersen, S. H. L. Klapp, and R. von Klitzing. *Soft Matter*, page DOI: 10.1039/C1SM05971H, 2011.

Danksagung

An dieser Stelle möchte ich die Gelegenheit nutzen allen Menschen zu danken, die mich während des Studiums und der Doktorarbeit begleitet haben, mich moralisch als auch fachlich unterstützt und letztlich die Doktorarbeit ermöglichten.

Besonderer Dank geht dabei an meine Betreuerin Prof. Sabine H. L. Klapp, welche durch ihre fachliche Unterstützung, konstruktive Kritik und nicht zuletzt durch ihre Geduld mich immer wieder motivieren konnte diese Arbeit zu Ende zu führen. Des Weiteren möchte ich mich bei Herrn Prof. Hartmut Löwen bedanken, dass er sich bereit erklärt hat Gutachter meiner Dissertation zu sein und bei Frau Prof. Birgit Kanngießer als Vorsitzende des Promotionsausschusses zu fungieren. Ein weiterer Dank geht dabei an meine Kollegen in unserer Arbeitsgruppe sowie an Prof. Martin Schoen und dessen Mitarbeiter. Bei Heiko Schmidle bedanke ich mich für das Korrekturlesen einiger Kapitel und fachliche Diskussionen. Bei Carlos Alvarez und Martial Mazars bedanke ich mich für interessante Diskussionen, die sehr hilfreich waren für meine Arbeit. Insbesondere möchte ich Helge Neitsch, Jelena Jordanovic und Dortje Schirok erwähnen, welche mir mit Rat und Tat zur Seite standen, wenn es mal schleppender lief, aber auch bei allen anderen Kollegen für die Unterstützung in den letzten Wochen.

Während der Zeit als wissenschaftlicher Mitarbeiter an der TU Berlin bzw. der FU Berlin gab es zudem einen Umbruch in meinem Leben, wodurch einerseits die Doktorarbeit zu einer größeren Herausforderung wurde. Andererseits ging ich mit einer neuen Motivation daraus hervor, welche die Arbeit letztlich positiv beeinflusste. In diesem Zusammenhang geht ein besonderer Dank an meine beste Freundin Katharina Schieritz sowie an Markus Radzsuweit und Jan Ranglack, welche mir während dieser Zeit sehr halfen, und an viele andere Freunde, die ich hier nicht alle aufzählen kann. Zu guter Letzt danke ich meinen Eltern, die meine Ziele immer unterstützten.